

The Spin Structure of the Proton From SLAC Experiment E155^{*}

P. M. McKee

Stanford Linear Accelerator Center
Stanford University
Stanford, CA 94309

SLAC-Report-622
August 2000

Prepared for the Department of Energy
under contract number DE-AC03-76SF00515

Printed in the United States of America. Available from the National Technical Information Service, U.S. Department of Commerce, 5285 Port Royal Road, Springfield, VA 22161.

^{*} Ph.D. thesis, University of Virginia, Charlottesville, VA 22901

Abstract

Experiment E155 at the Stanford Linear Accelerator Center (SLAC) measured the longitudinal and transverse deep inelastic structure functions of the proton and deuteron using a polarized, 48.3 GeV electron beam and solid polarized targets of ammonia ($^{15}\text{NH}_3$) for proton measurements and lithium deuteride ($^6\text{Li}^2\text{H}$) for deuteron measurements. Three electromagnetic spectrometers at angles of 2.75° , 5.5° , and 10.5° measured the scattered electrons. This work presents an analysis of the longitudinal structure function of the proton, $g_1^p(x, Q^2)$. Included is a re-analysis of the proton target polarization data that for the first time corrects a problem encountered which altered those measurements.

Acknowledgements

The task of enumerating all the sources of support that have permitted me to pursue this degree is easily as difficult as the pursuit of the degree itself. Below are some of the obvious factors that have most directly allowed me to achieve this goal.

I would first like to thank my advisor, Dr. Donal Day for guiding me through the completion of this work, and for many enjoyable conversations, both related to physics and not. Drs. Don Crabb and Oscar Rondon have also been instrumental in my development as a physicist, with all three of these individuals providing almost complete illumination of the stunning vastness that endows this field with such interest. I would also like to thank my former advisor, Dr. James McCarthy for introducing me to this field.

The number of graduate students working on E155 was half that of some of the recent experiments at SLAC. Luckily, my colleagues were more than up to the task. Special nods of appreciation go to the other stars of E155: Greg Mitchell, Terry Toole, Al Tobias, Paul King, and Frank Wesselmann.

Another graduate student, Chris Cothran, deserves special mention. Chris has always made the time to provide a concerned ear or a helpful explanation, whether the problem was with physics or not. In many ways, I feel as if we see the scientific world through the same eyes.

I doubt my path would have led so clearly to physics were it not for my father, Michael McKee. I have memories dating back to the age of three of him presenting to me a world full of physical mysteries whose depth is only surpassed by the enjoyment gained by solving them.

No amount of mystery would be worth pursuing without the deep sense of balance I've gained from my mother, Jeanne McKee. The faithfulness to one's feelings and convictions that she has imprinted on me has given me a sense of self I would not wish to live without.

Finally, I devote the rest of these comments to the person to whom I devote the rest of my life, my wife Dana Tornabene. The light shines brightly from you, darling. Its reflections make my whole world more beautiful.

Contents

1	Introduction	1
2	Theory	4
2.1	Deep Inelastic Scattering	4
2.2	Cross Sections and Structure Functions	6
2.3	Virtual Photon Asymmetries	10
2.4	Quark Parton Model	13
2.5	Sum Rules	17
3	Experimental Setup	20
3.1	Beam and Beamline Components	20
3.1.1	Source	20
3.1.2	Beamline	22
3.1.3	Beamline Components in End Station A	26
3.1.4	Dump	28
3.1.5	Møller Polarimeters	28
3.2	Spectrometers	34
3.2.1	Optics	34
3.2.2	Hodoscopes	38
3.2.3	Čerenkov Counters	38
3.2.4	Lead Glass Detector	39
3.2.5	Electronics	40
4	Polarized Target	42
4.1	Theory of Solid Polarized Targets	42
4.1.1	Dynamic Nuclear Polarization	45
4.1.2	Nuclear Magnetic Resonance	49
4.1.3	Q Meter Operation	50
4.2	Target Setup and Equipment	55
4.2.1	Proton Material	56
4.2.2	Deuteron Material	57
4.2.3	Cryostat, Refrigerator, and Magnet	59
4.2.4	Target Insert	62

4.2.5	NMR System	63
4.2.6	Temperature Measurement	66
4.2.7	Microwave System	69
4.3	Analysis of Target Data	70
4.3.1	NMR Signal Analysis	71
4.3.2	Thermal Equilibrium Calibration	72
4.3.3	Measurement of Other Spin Species	75
4.4	Correction of Proton NMR Signals	77
4.4.1	Attempts to Correct the NMR Data	80
4.4.2	Failure of the Constant Current Condition	83
4.4.3	Using Radiation Damage Curves as a Correction	86
5	Asymmetry Analysis	102
5.1	Raw Asymmetries	102
5.1.1	Data Reduction	102
5.1.2	Electron Definition	103
5.1.3	Run Selection	106
5.1.4	Experimental Asymmetry	107
5.2	Asymmetry Corrections	107
5.2.1	Pion Background Correction	107
5.2.2	Charge-Symmetric Processes	110
5.2.3	Electro-Weak Correction	112
5.2.4	Rate Dependence	113
5.3	Beam Quantities	114
5.3.1	Møller Polarimeter Measurements	114
5.3.2	Reporting of Beam Helicity	115
5.4	Dilution Factor	116
5.5	Nuclear Corrections	120
5.6	Radiative Corrections	122
5.7	Structure Functions and Integrals	125
5.7.1	Determining the Final Structure Functions	125
5.7.2	Evolution to a Common Q^2	127
5.7.3	Proton, Deuteron, and Neutron Functions for $0 \leq x \leq 1$	131
5.7.4	Sum Rules	137
6	Conclusions	140
A	NMR Correction Based on ^{15}N Polarization	143
B	NMR Correction Based on Lineshape Fitting	150

List of Figures

2.1	Feynman diagram of the fundamental deep inelastic scattering process.	5
2.2	Acceptance of the E155 spectrometers and kinematic cuts used. . . .	6
2.3	Current measurement of $F_2(x, Q^2)$	16
3.1	Facilities at SLAC	21
3.2	Components of the Injector and Polarized Source	22
3.3	Energy states in unstrained and strained GaAs	23
3.4	Results of Møller energy scan	26
3.5	Components of the Møller Detectors	33
3.6	Layout of Spectrometers in ESA.	35
3.7	Kinematic coverage of the E155 spectrometers	36
4.1	Level diagram for a nucleon-electron system in a magnetic field	46
4.2	Transitions involved in polarization enhancement	47
4.3	Block diagram of the main Q Meter circuit.	52
4.4	The E155 Polarized Target Cryostat and Refrigerator.	60
4.5	Layout of the target cavities in the E155 target insert.	63
4.6	Components of the E155 NMR System.	67
4.7	Steps of the E155 NMR signal analysis	73
4.8	NMR signal area as the target material comes to thermal equilibrium.	75
4.9	TE calibration constants from an E155 target insert.	76
4.10	^{15}N versus proton polarizations.	77
4.11	Comparison of NMR signals of $^{15}\text{NH}_3$ at 2.5 T and 5 T.	81
4.12	Fit of a modeled lineshape to a real proton NMR signal.	83
4.13	Resonant circuit with the addition of stray capacitance.	84
4.14	Impedance of a normal NMR coil as a function of frequency.	87
4.15	Possible impedance of an E155 NMR coil as a function of frequency. .	87
4.16	Typical decay of polarization with accumulated beam dose.	88
4.17	E155 positive polarization anneal cycles.	92
4.18	E155 negative polarization anneal cycles.	93
4.19	Correction for the positive polarization, copper NMR coil subset. . .	95
4.20	Correction for the negative polarization, copper NMR coil subset. . .	96
4.21	Correction for the positive polarization, aluminum NMR coil subset. .	97

4.22	Correction for the negative polarization, aluminum NMR coil subset.	98
4.23	Data and averaged curve for the E155x reference set.	99
4.24	Final curves used to correct the E155 proton polarization data.	100
4.25	Measured region integral of g_1^p for uncorrected and corrected data . . .	101
5.1	Hadron contamination vs. x	109
5.2	Hadron asymmetry vs. x	109
5.3	Positron contamination vs. x	111
5.4	Positron asymmetry vs. x	111
5.5	Beam Polarizations measured with the Single-Arm Møller	115
5.6	Dilution factor for the three E155 spectrometers.	119
5.7	Packing fraction as a function of x for an E155 target.	120
5.8	Examples of external processes that require radiative corrections. . .	125
5.9	Examples of internal processes that require radiative corrections. . . .	125
5.10	g_1^p/F_1^p plotted as a function of Q^2	132
5.11	g_1^p plotted as a function of Q^2	133
5.12	E155 g_1 for proton, deuteron, and neutron	135
5.13	E155 xg_1 for proton, deuteron, and neutron.	136
5.14	E155 integrals and sum rule predictions.	139
A.1	Comparison of NMR signals of $^{15}\text{NH}_3$ at 2.5 T and 5 T.	144
A.2	Polarization buildup measuring proton and ^{15}N polarization.	146
A.3	Correction from measured values and Equation 4.17.	148
A.4	NMR signal anomalies interfering with residual background fit	149
B.1	Ideal absorptive and dispersive NMR signals.	151
B.2	Sample E155 proton NMR signal.	151
B.3	Fit of Equation B.8 to a typical E155 NMR signal.	156
B.4	Correction curve generated by fitting NMR signals to Equation B.8. . .	157

List of Tables

2.1	Variables used in discussing Deep Inelastic Scattering.	5
4.1	Lengths of $\lambda/2$ cables	64
4.2	Performance of the four batches of material used in g_1^p running.	90
5.1	Cuts comprising the E155 Electron Definition.	105
5.2	Variables used in ^{15}N nuclear correction.	121
5.3	Parameters from fit to g_1/F_1	128
5.4	g_1^p/F_1^p and g_1^p at $Q^2 = 5 \text{ GeV}^2$ for the 2.75° spectrometer.	129
5.5	g_1^p/F_1^p and g_1^p at $Q^2 = 5 \text{ GeV}^2$ for the 5.5° & 10.5° spectrometers.	130
5.6	Definitions of world bins.	131

Chapter 1

Introduction

The ancient Greeks thought that matter consisted of Earth, Wind, Fire, and Water. Before that, the Chinese claimed it was Yin and Yang. Mankind seems to have an instinctual desire to discover the fundamental components of matter, a drive which still today fuels ambitious endeavors and heated debate.

The past 100 years have seen incredible advances in our understanding of the building blocks of matter. This started with the discovery of the atom, and continued with the understanding that it, in turn, is made of a dense positively charged nucleus surrounded by a negatively charged cloud of electrons, resulting in a neutral whole.

Further study revealed the nucleus to be made of positively charged protons and uncharged neutrons, with the number of protons and electrons equal in a neutral atom. In the 1960's it was discovered that protons and neutrons are themselves comprised of smaller components, called quarks, with one combination of three quarks comprising a proton and a different combination comprising a neutron.

Currently, a total of six types of quarks have been discovered, each with an antimatter counterpart. Similarly, it is now known that the electron is a member of a family of six leptons, each also having an antimatter sibling. The body of theory

that describes the interaction of these particles is universally referred to as the *Standard Model* - a very successful theory encompassing three of the four known forces of nature.

One of the properties of the particles described by the standard model is that of *intrinsic spin*. Spin is a term used to describe a fundamental attribute of a particle that gives rise to its magnetic dipole moment. All particles may be divided into two groups: *fermions* have an intrinsic spin of $\frac{n}{2}$, with n an odd integer, and *bosons* have integral spin. All of the quarks and leptons are fermions with a spin of $\frac{1}{2}$. The particles that transmit forces among the quarks and leptons are all bosons.

One of the best tools we have to investigate spin effects in nucleons is particle scattering: the likelihood that an electron of known spin will scatter off a nucleon will depend on the spin state of that nucleon. Measurement of the asymmetry in the scattering cross section can be connected to fundamental quantities relating to the nucleon. Combinations of these quantities, in turn, give an indication of the spin content of the type of nucleon studied.

There are three quantities that contribute to the total spin of the proton: the spin from the quarks, $\Delta\Sigma$, the spin from the gluons that bind the quarks together, ΔG , and the total angular momentum of the quarks and gluons, L . Early theories predicted that the proton spin was due entirely to the contribution from the quarks, $\Delta\Sigma$. In contrast, experiments have shown $\Delta\Sigma$ to be less than half of the predicted value. When this was first discovered [1], it was such a surprise and generated such interest that the discrepancy came to be termed, with a touch of hyperbole, the *spin crisis*, and resulted in hundreds of journal articles and several major experiments.

At present, many experiments have measured $\Delta\Sigma$, including EMC [1] and SMC [2, 3] at CERN, HERMES [4] at DESY, and E142 [5, 6], E143 [7–9], E154 [10, 11], and E155 [12–14] at SLAC. Two of these experiments, SMC and E155 have performed

initial measurements of ΔG , with upcoming experiments to provide significant improvement in measurement precision. Measurement of L is not accessible to current experimental techniques, but may be deduced once accurate measurements of $\Delta\Sigma$ and ΔG are made.

The subject of this dissertation is experiment E155, conducted at the Stanford Linear Accelerator Center (SLAC) in Palo Alto, California. The fourth in a series of four spin experiments at SLAC, it ran in March and April of 1997 with a 48.3 GeV polarized electron beam produced by the SLAC linac, incident on a solid polarized target of ammonia ($^{15}\text{NH}_3$) or lithium deuteride (^6LiD), thus facilitating measurements on polarized protons or deuterons, respectively. Three fixed-angle, electromagnetic spectrometers were used to measure the energy and momentum of electrons scattered from the target. The polarizations of the target and beam were also measured. Approximately 2.5 terabytes (2500 MB) of data were written to tape, the analysis of which yielded data on approximately 200 million scattered electrons.

Chapter 2 discusses the theory of Deep Inelastic Scattering used in the conduction and analysis of this experiment. Chapter 3 describes the equipment used to produce and deliver the beam to the target and the spectrometers used to measure the electrons scattered from the target. Chapter 4 discusses the theory of polarized targets, describes the setup of the target equipment, and presents a new, complete re-analysis of the polarized proton measurements, with particular attention paid to the correction of a problem encountered in those measurements. Chapter 5 shows the asymmetry analysis resulting from the new polarization data. Finally, Chapter 6 contains conclusions from this analysis and discusses future work in the field.

Chapter 2

Theory

2.1 Deep Inelastic Scattering

The fundamental process studied in E155 is the exchange of a virtual photon between an electron in the beam and a quark in a polarized target nucleon. This can be seen as the elastic scattering of the quark from the virtual photon. Before discussion can proceed on the theory of such scattering, this section will define the variables that will be used throughout this work. Sections 2.2 and 2.3 will then present the equations used to express the cross section of the scattering process involved. Section 2.4 presents an interpretation of the scattering processes according to the parton model, and finally Section 2.5 discusses relations involving integrals of the nucleon structure functions.

Figure 2.1 shows the Feynman diagram of the fundamental scattering process. Table 2.1 lists the variables that will be used. For variables that represent combinations of other fundamental quantities, expressions are given in Lorentz-invariant form as well as in the Lab reference frame whenever possible.

The Deep Inelastic regime is defined as scattering with a Q^2 greater than 1 GeV^2 ,

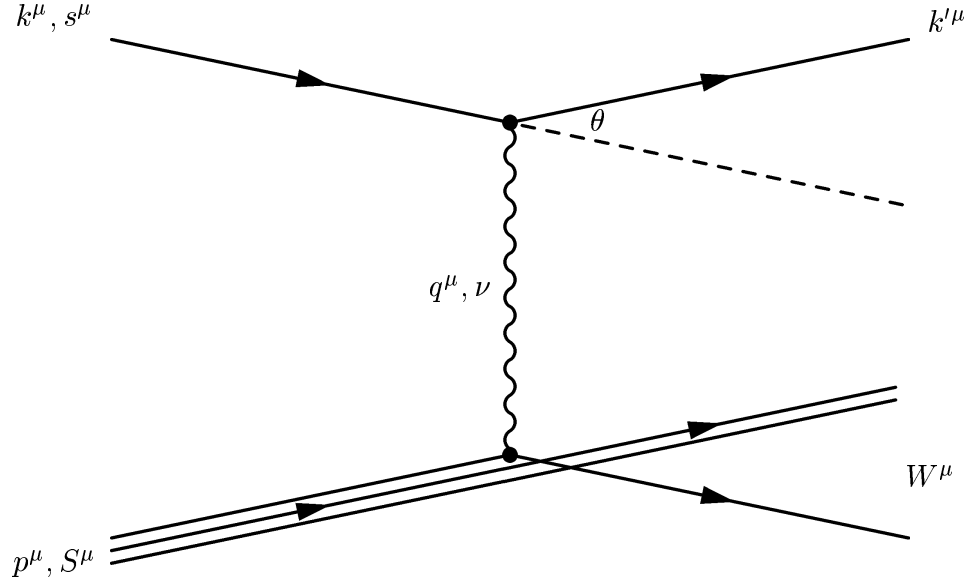


Figure 2.1: Feynman diagram of the fundamental deep inelastic scattering process.

Variable Name	Invariant Form	Lab Frame	Meaning (in Lab Frame)
E		E	Lab frame initial electron energy
M		M	Rest mass of target nucleon
k^μ		$(E, 0, 0, \vec{k})$	Initial 4-momentum of electron
s^μ		$1/m(\vec{k}, 0, 0, E)$	Initial spin vector of electron
E'		E'	Lab frame final electron energy
k'^μ		(E', \vec{k}')	Final 4-momentum of electron
θ		θ	Lab frame electron scattering angle
p^μ		$(M, 0, 0, 0)$	Initial 4-momentum of nucleon
S^μ			Initial spin vector of nucleon
q^μ		$k - k'$	4-momentum of the virtual photon
ν	$p \cdot q / M$	$E - E'$	Lab frame energy of virtual photon
Q^2	$(k - k')^2$	$4EE' \sin^2(\theta/2)$	Virtual photon 4-momentum squared
x	$Q^2 / 2p \cdot q$	$Q^2 / 2M\nu$ or $2EMxy$	Fraction of nucleon momentum carried by the struck quark
y	$(p \cdot q) / (p \cdot k)$	ν / E	Fraction of energy lost by electron
W^2	$(p + q)^2$	$M^2 + Q^2 \frac{(1-x)}{x}$	Invariant mass squared of hadronic final state

Table 2.1: Variables used in discussing Deep Inelastic Scattering.

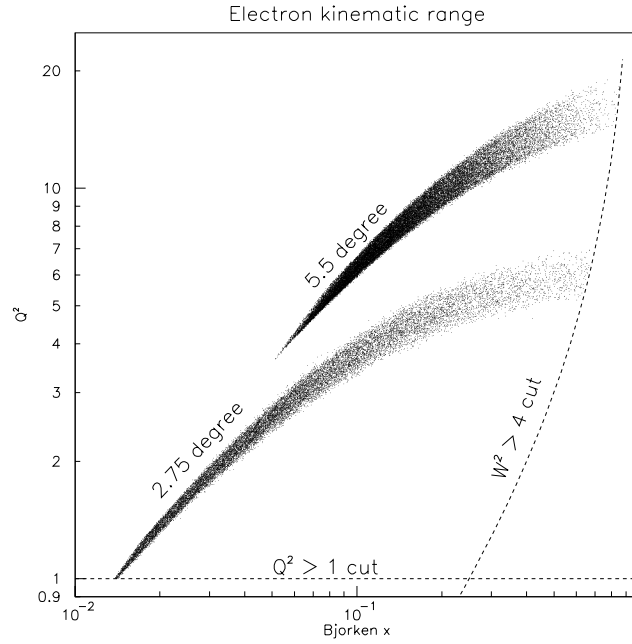


Figure 2.2: Acceptance of the E155 spectrometers and kinematic cuts used.

and with W^2 , the mass squared of the final state of the nucleon, greater than 4 GeV^2 . These restrictions result in a slight loss of events in the spectrometers used in E155. As can be seen in Figure 2.2, some events in the 2.75° spectrometer are eliminated by the Q^2 cut, while the W^2 removes events from all the spectrometers. The spectrometers, described in Section 3.2, were designed so that the vast majority of the electrons detected were from deep inelastic scattering.

2.2 Cross Sections and Structure Functions

The cross section for the interaction depicted in Figure 2.1 can be written [15] in the form

$$\frac{d^2\sigma}{d\Omega dE'} = \frac{\alpha^2}{2MQ^4} L_{\mu\nu} W^{\mu\nu}. \quad (2.1)$$

The $L_{\mu\nu}$ tensor describes the electron-photon vertex. Since the electron is a funda-

mental Dirac particle, $L_{\mu\nu}$ may be written (summing over final electron polarization states) as

$$L_{\mu\nu} = 2(k'_\mu k'_\nu + k'_\nu k'_\mu - g_{\mu\nu}(k \cdot k' - m^2) - im\epsilon_{\mu\nu\rho\sigma} s^\sigma q^\rho) \quad (2.2)$$

The $W^{\mu\nu}$ term in Equation 2.1 represents the virtual photon-nucleon interaction. Since the nucleon is not a fundamental particle, an expression for this tensor cannot be directly written. However, the general form of $W^{\mu\nu}$ can be constrained by using several properties that it must possess. It must be a Lorentz invariant transforming as a rank 2 tensor, it must be invariant under time reversal and parity, and it must conserve the hadronic electromagnetic current. If we sum over all possible final hadronic states and final hadronic spins, $W^{\mu\nu}$ can be written as

$$\begin{aligned} W^{\mu\nu} = & F_1(x, Q^2)(-g^{\mu\nu} + \frac{q^\mu q^\nu}{q^2}) \\ & + \frac{F_2(x, Q^2)}{p \cdot q}(p^\mu - \frac{p \cdot q}{q^2}q^\mu)(p^\nu - \frac{p \cdot q}{q^2}q^\nu) \\ & + i \frac{g_1(x, Q^2)}{p \cdot q} \epsilon^{\mu\nu\sigma\rho} S_\sigma q_\rho \\ & + i \frac{g_2(x, Q^2)}{(p \cdot q)^2} \epsilon^{\mu\nu\sigma\rho} [(p \cdot q)S_\sigma - (S \cdot q)p_\sigma]q_\rho \end{aligned} \quad (2.3)$$

There are four functions of x and Q^2 in this expression – F_1 , F_2 , g_1 , and g_2 – that are known as *structure functions* of the nucleon involved. F_1 and F_2 are the unpolarized structure functions and contribute to the cross section in all scattering events. g_1 and g_2 , the polarized structure functions or spin structure functions, contribute to the cross section only in those cases in which both the incident electron and the struck nucleon are polarized.

Experimentally, measuring absolute cross sections directly is more difficult than measuring differences in cross sections. With the ability to change the beam helicity

on a pulse-by-pulse basis at SLAC, two target/beam helicity combinations can be measured simultaneously. This has the distinct advantage that slowly varying factors, such as beam quality, spectrometer acceptance, target polarization, etc, do not distort the measurement, since both cross sections are impacted equally, and thus their difference is unaffected.

For the case of longitudinally polarized beam and longitudinally polarized target, we may write the cross section difference in the lab frame as

$$\frac{d^2\sigma^{\downarrow\uparrow}}{d\Omega dE'} - \frac{d^2\sigma^{\uparrow\uparrow}}{d\Omega dE'} = \frac{4\alpha^2 E'}{Q^2 M E \nu} [(E + E' \cos \theta)g_1(x, Q^2) - 2xMg_2(x, Q^2)] \quad (2.4)$$

where the single arrow depicts the polarization of the beam and the double arrow depicts the polarization of the target.

When expressing the difference of two small cross sections, as in Equation 2.4, the relative errors can be quite large. Instead, the *asymmetry* of the cross section is often discussed, defined as the difference of the cross sections divided by their sum. For a longitudinally polarized beam and target, the parallel asymmetry is

$$A_{\parallel}(x, Q^2) = \frac{\frac{d^2\sigma^{\downarrow\uparrow}}{d\Omega dE'} - \frac{d^2\sigma^{\uparrow\uparrow}}{d\Omega dE'}}{\frac{d^2\sigma^{\downarrow\uparrow}}{d\Omega dE'} + \frac{d^2\sigma^{\uparrow\uparrow}}{d\Omega dE'}}. \quad (2.5)$$

Similarly, a transverse asymmetry, A_{\perp} can be defined for scattering of a longitudinally polarized beam from a transversely polarized target

$$A_{\perp}(x, Q^2) = \frac{\frac{d^2\sigma^{\downarrow\Rightarrow}}{d\Omega dE'} - \frac{d^2\sigma^{\uparrow\Rightarrow}}{d\Omega dE'}}{\frac{d^2\sigma^{\downarrow\Rightarrow}}{d\Omega dE'} + \frac{d^2\sigma^{\uparrow\Rightarrow}}{d\Omega dE'}}. \quad (2.6)$$

The advantage of dealing with asymmetries over cross section differences is that common factors cancel, along with their associated uncertainties.

We may write g_1 and g_2 in terms of these asymmetries as

$$g_1(x, Q^2) = \frac{F_1(x, Q^2)}{D'} \left(A_{\parallel}(x, Q^2) + \tan \frac{\theta}{2} A_{\perp}(x, Q^2) \right) \quad (2.7)$$

and

$$g_2(x, Q^2) = \frac{yF_1(x, Q^2)}{2D'} \left(\frac{E + E' \cos \theta}{E' \sin \theta} A_{\perp}(x, Q^2) - A_{\parallel}(x, Q^2) \right). \quad (2.8)$$

Note that in order to determine the value of g_1 both A_{\parallel} and A_{\perp} must be measured. However, the contribution to g_1 from A_{\perp} is suppressed by a factor $\tan \frac{\theta}{2}$ relative to A_{\parallel} . D' is defined as

$$D' = \frac{(1 - \epsilon)(2 - y)}{y[1 - \epsilon R(x, Q^2)]} \quad (2.9)$$

where

$$\epsilon = \frac{1}{1 + 2(1 + \frac{\nu}{Q^2}) \tan^2 \theta / 2}, \quad (2.10)$$

and $R(x, Q^2)$ is defined below.

Since we are only discussing cross section differences, and the helicity of the incident electrons is reversed several tens of times a second, we can make the further simplification of replacing the cross sections with the spectrometer counting rates per incident charge. In order to do this, we must also make an appropriate correction for the fact that neither the beam nor the target is perfectly polarized, and that the target does not consist of only polarized nucleons, but has other materials (polarized and unpolarized) in it. We can then write the asymmetry as

$$A_{\parallel}(x, Q^2) = \frac{1}{fP_b P_t C_1} \frac{(N/Q)^{\downarrow\uparrow} - (N/Q)^{\uparrow\uparrow}}{(N/Q)^{\downarrow\uparrow} + (N/Q)^{\uparrow\uparrow}}, \quad (2.11)$$

where N is the number of counts and Q the total incident charge for a given beam-nucleon helicity combination, f is the *dilution factor* which is the ratio of polarizable

nucleons to total nucleons, P_b and P_t are the beam and target polarizations, respectively, and C_1 is a correction factor for nuclear effects in the target material, discussed in Section 5.5.

2.3 Virtual Photon Asymmetries

Up to now we have discussed the scattering asymmetry in terms of the incoming electron. This is logical because it is the electron beam that produces the virtual photons that couple to the nucleon. We may also choose to discuss the virtual photon-nucleon scattering asymmetries, known as $A_1(x, Q^2)$ and $A_2(x, Q^2)$. The Optical Theorem may be used to tie the deep inelastic scattering cross sections to the imaginary component of the forward virtual-photon Compton scattering amplitudes.

For a spin- $\frac{1}{2}$ target there are four independent amplitudes,

$$\text{Im}(\mathcal{M}_{+1, -\frac{1}{2}, +1, -\frac{1}{2}}) \equiv \sigma_{1/2}^T = \frac{1}{M} (F_1 + g_1 - \gamma^2 g_2) \quad (2.12)$$

$$\text{Im}(\mathcal{M}_{+1, +\frac{1}{2}, +1, +\frac{1}{2}}) \equiv \sigma_{3/2}^T = \frac{1}{M} (F_1 - g_1 + \gamma^2 g_2) \quad (2.13)$$

$$\text{Im}(\mathcal{M}_{+0, +\frac{1}{2}, +0, +\frac{1}{2}}) \equiv \sigma_{1/2}^L = \frac{1}{M} \left(-F_1 + \frac{1 + \gamma^2}{2x} F_2 \right) \quad (2.14)$$

$$\text{Im}(\mathcal{M}_{+1, -\frac{1}{2}, +0, +\frac{1}{2}}) \equiv \sigma_{1/2}^{TL} = \frac{\gamma\sqrt{2}}{M} (g_1 + g_2), \quad (2.15)$$

where the subscripts of \mathcal{M} denote the initial photon, initial nucleon, final photon, and final nucleon helicities, respectively. The superscripts of σ indicate the transverse (T) or longitudinal (L) polarization of the photon, or the interference between the two (TL); the subscripts of σ indicate the total spin of the virtual photon-nucleon system quantized in the direction of the electron's initial momentum. The kinematic factor $\gamma^2 = Q^2/\nu^2 = 4M^2 x^2/Q^2$ has also been introduced.

The virtual photon-nucleon asymmetries may now be expressed as

$$A_1(x, Q^2) \equiv \frac{\sigma_{\frac{1}{2}}^T - \sigma_{\frac{3}{2}}^T}{\sigma_{\frac{1}{2}}^T + \sigma_{\frac{3}{2}}^T} = \frac{g_1(x, Q^2) - \gamma^2 g_2(x, Q^2)}{F_1(x, Q^2)} \quad (2.16)$$

$$A_2(x, Q^2) \equiv \frac{\sigma_{\frac{1}{2}}^{TL}}{\sigma_{\frac{1}{2}}^T + \sigma_{\frac{3}{2}}^T} = \frac{\gamma [g_1(x, Q^2) + g_2(x, Q^2)]}{F_1(x, Q^2)}. \quad (2.17)$$

It should be noted that γ is small and can be neglected only at very high energies, leading to the approximation $A_1 \approx g_1/F_1$ used by experiments at CERN, as can be seen from Equation 2.16.

The electron-nucleon asymmetries and the polarized nucleon structure functions may be written in terms of A_1 and A_2 as

$$A_{\parallel}(x, Q^2) = D(x, Q^2) [A_1(x, Q^2) + \eta A_2(x, Q^2)] \quad (2.18)$$

$$A_{\perp}(x, Q^2) = d(x, Q^2) [A_2(x, Q^2) - \zeta A_1(x, Q^2)] \quad (2.19)$$

$$g_1(x, Q^2) = \frac{F_1}{1 + \gamma^2} [A_1(x, Q^2) + \gamma A_2(x, Q^2)] \quad (2.20)$$

$$g_2(x, Q^2) = \frac{F_1}{1 + \gamma^2} \left[\frac{1}{\gamma} A_2(x, Q^2) - A_1(x, Q^2) \right], \quad (2.21)$$

where

$$D(x, Q^2) = \frac{1 - \epsilon E'/E}{1 + \epsilon R(x, Q^2)} \quad (2.22)$$

$$\eta = \epsilon \frac{\sqrt{Q^2}}{E - \epsilon E'} \quad (2.23)$$

$$d(x, Q^2) = D(x, Q^2) \sqrt{\frac{2\epsilon}{1 + \epsilon}} \quad (2.24)$$

$$\zeta = \eta \frac{1 + \epsilon}{2\epsilon} \quad (2.25)$$

$$\epsilon = \frac{1}{1 + 2(1 + \nu^2/Q^2) \tan^2(\theta/2)}. \quad (2.26)$$

The function $R(x, Q^2)$ is defined in terms of the virtual photon cross sections as

$$R(x, Q^2) = \frac{\sigma^L}{\sigma^T}, \quad (2.27)$$

where $\sigma^L \equiv \sigma_{1/2}^L$ and $\sigma^T \equiv \sigma_{1/2}^T + \sigma_{3/2}^T$ for a spin- $\frac{1}{2}$ target.

At E155 kinematics, $R(x, Q^2)$ is found to be small [16] - around 0.25 at low x and decreasing with increasing x . This may be interpreted as the result of the spin- $\frac{1}{2}$ nature of the quarks, since a spin- $\frac{1}{2}$ quark can only absorb a transverse photon (helicity = ± 1) and not a longitudinal one (helicity = 0).

The unpolarized structure functions are also related to $R(x, Q^2)$ through

$$F_1(x, Q^2) = F_2(x, Q^2) \frac{1 + \gamma^2}{2x[1 + R(x, Q^2)]}, \quad (2.28)$$

which can be obtained from Equations 2.12 through 2.14.

Since the σ are all positive quantities, a bound may be put on A_1 , known as the *positivity limit*

$$|A_1(x, Q^2)| \leq 1. \quad (2.29)$$

The interference term $\sigma_{1/2}^{TL}$ can be positive or negative, leaving the sign of $A_2(x, Q^2)$ undetermined. However, applying the Schwartz inequalities, one can show that

$$|\sigma_{1/2}^{TL}| < \sqrt{\sigma^T \sigma^L}. \quad (2.30)$$

Dividing Equation 2.30 by σ^T yields

$$\left| \frac{\sigma_{1/2}^{TL}}{\sigma^T} \right| < \frac{\sqrt{\sigma^T \sigma^L}}{\sigma^T} = \sqrt{\frac{\sigma^L}{\sigma^T}}, \quad (2.31)$$

$$|A_2(x, Q^2)| < \sqrt{R(x, Q^2)}. \quad (2.32)$$

2.4 Quark Parton Model

DIS Experiments at SLAC in the late 1960's measured nucleon cross sections that did not decrease with increasing Q^2 as expected, but rather seemed to depend only on x , a property known as *x-scaling*. This Q^2 independence suggested that the scattering took place off very small, possibly point-like objects in the nucleon. Feynman explained these phenomena in the Quark Parton Model (QPM) [17], which postulates that the virtual photon scatters off these point-like objects, which he termed *partons*. Later, partons were identified with the *quarks* postulated in Gell-Mann and Zweig's theory of hadrons. In this model, the DIS cross section of the nucleon as a whole is explained as an incoherent sum of the cross sections for elastic scattering of the virtual photon off each of the types of quarks in the nucleon.

The *parton distribution functions*, $q_i(x, Q^2)$, give the probability to find in the proton a quark of flavor i with momentum between a factor of x and $x + dx$ times that of the parent nucleon. They are important in this context because they can be related to the nucleon structure functions, as will be discussed below. They can be expressed as a sum of helicity states for a single quark flavor,

$$q_i(x) = [q_i^\uparrow(x) + q_i^\downarrow(x)] + [\bar{q}_i^\uparrow(x) + \bar{q}_i^\downarrow(x)], \quad (2.33)$$

where the arrow indicates quarks with spin that is aligned (\uparrow) or anti-aligned (\downarrow) with the nucleon spin, and \bar{q}_i is the distribution function for the antiquark of flavor i .

Experimentally, six flavors of quarks have been observed*. The contribution of each flavor to the total momentum of the nucleon is just the integral of x times the parton distribution for that flavor over the range $0 \leq x \leq 1$. The sum of the

*In the kinematic region of E155, with $\langle Q^2 \rangle$ on the order of 5 GeV², only the three light quarks – u , d , and s – and their antiquarks need be considered.

contributions from all flavors should be bounded by unity

$$\sum_i^{N_f} \int_0^1 x q_i(x) dx \leq 1, \quad (2.34)$$

where N_f represents the total number of quark flavors. Equation 2.34 is known as the *momentum sum rule*, as the left hand side of the equation represents the total nucleon momentum contributed by quarks.

QCD sets an asymptotic limit on this sum of $1/(1 + \frac{16}{3N_f})$. Using the current count of six quark flavors, this limit is close to $\frac{1}{2}$, in agreement with experiment, and suggesting that perhaps all quark flavors have been identified [18, 19].

The Detailed Quark Parton Model considers the nucleon in the infinite momentum frame, in which the parton mass and any parton momentum transverse to that of the nucleon may be ignored. This model results in expressions for $F_1(x)$ and $F_2(x)$ that are independent of Q^2

$$F_1(x) = \frac{1}{2} \sum_i e_i^2 q_i(x), \text{ and} \quad (2.35)$$

$$F_2(x) = \sum_i e_i^2 x q_i(x), \quad (2.36)$$

where e_i is the charge of quarks of flavor i . The connection between the structure functions $F_2(x, Q^2) = 2xF_1(x, Q^2)$ is known as the Callan-Gross relation [20].

Parallel to Equation 2.33, polarized parton distribution functions may also be defined, representing the difference between helicity states of a single quark flavor

$$\delta q_i(x) = [q_i^\uparrow(x) - q_i^\downarrow(x)] + [\bar{q}_i^\uparrow(x) - \bar{q}_i^\downarrow(x)]. \quad (2.37)$$

The integral of the polarized distribution functions will be written as

$$\Delta q_i \equiv \int_0^1 \delta q_i(x) dx. \quad (2.38)$$

Similar to Equation 2.35, $g_1(x)$ may be expressed as

$$g_1(x) = \frac{1}{2} \sum e_i^2 \delta q_i(x). \quad (2.39)$$

The QCD-Improved Quark Parton Model accounts for gluons in the nucleon, in addition to quarks and antiquarks, resulting in a Q^2 dependence of the structure functions and parton distributions [21]. This dependence goes as $\ln Q^2$ and can be explained in terms of the quark's increasing likelihood to radiate gluons as Q^2 increases.

Figure 2.3 shows current measurements of F_2 over a large Q^2 range. The Q^2 dependence of the data can be readily seen. The decrease with Q^2 in the high x bands can be interpreted as the struck quark being increasingly likely to radiate gluons, reducing that quark's contribution to the nucleon momentum. At low x , the number of sea quarks produced increases with the number of gluons present. As Q^2 increases, the likelihood of the quark radiating gluons also increases, resulting in a rising contribution to the nucleon momentum.

Combinations of the polarized parton distribution functions, Δq_i , may be related to matrix elements of the proton axial current, a_i , defined by

$$2MS_\mu a_i = \langle p, S | \bar{q} \gamma_\mu \gamma_5 \frac{\lambda^i}{2} q | p, S \rangle, \quad (2.40)$$

for $i = 0$ to 8.

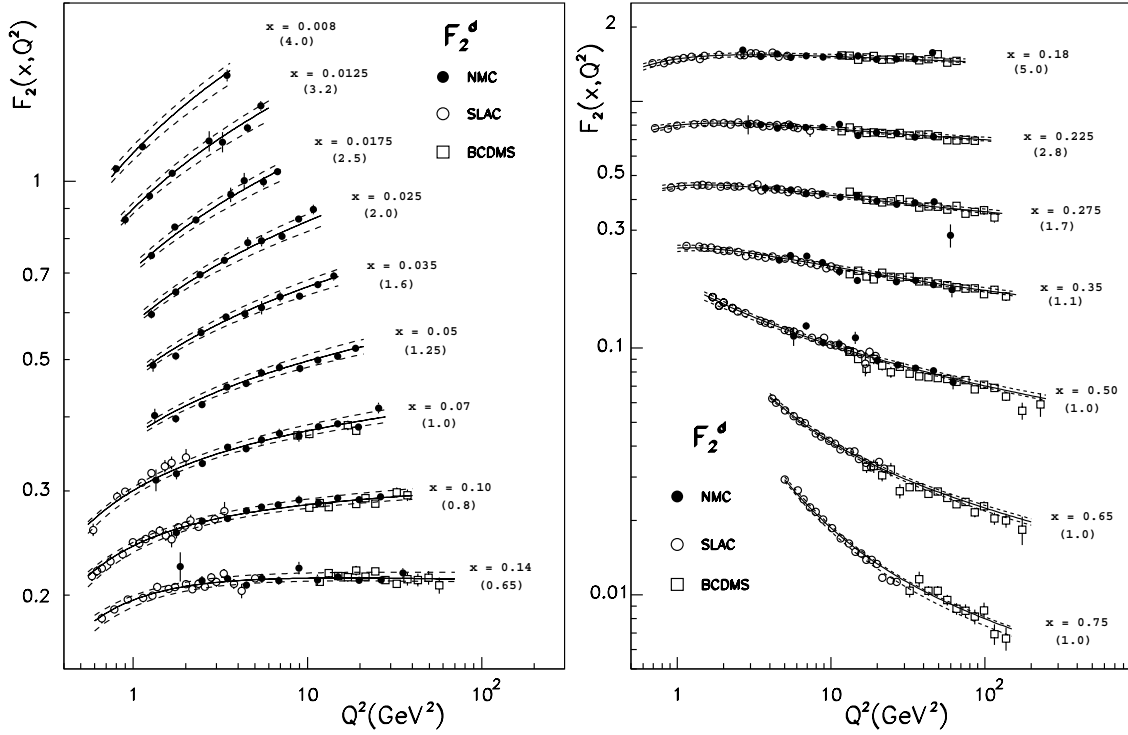


Figure 2.3: Current measurement of $F_2(x, Q^2)$. Data for each x bin have been multiplied by the values shown in parentheses.

The matrix elements that may be related to the parton distribution functions are

$$\text{Singlet : } a_0 = \Delta q_u + \Delta q_d + \Delta q_s \quad (2.41)$$

$$\text{Triplet : } a_3 = \Delta q_u - \Delta q_d \quad (2.42)$$

$$\text{Octet : } a_8 = \Delta q_u + \Delta q_d - 2\Delta q_s. \quad (2.43)$$

Assuming exact SU(3) flavor symmetry, the non-singlet matrix elements, a_3 and a_8 , may be expressed in terms of two coupling constants, F and D , as

$$a_3 = F + D \quad (2.44)$$

$$a_8 = 3F - D \quad (2.45)$$

which are used to describe the weak decays of the light-quark baryon octet, a group which includes the proton and neutron [15]. The values of F and D are measured in hyperon β decay.

Assuming isospin symmetry, the combination $F + D$ is equated to the axial/axial-vector coupling constant ratio g_A/g_V , which can be determined by measurement of β -decay of the neutron

$$a_3 = (F + D) = \left. \frac{g_A}{g_V} \right|_{np}. \quad (2.46)$$

Current experimental results for this quantity are [22]

$$\left. \frac{g_A}{g_V} \right|_{np} = 1.2670 \pm 0.0035, \quad (2.47)$$

while results for the combination $3F - D$ are [23]

$$3F - D = 0.584 \pm 0.032. \quad (2.48)$$

2.5 Sum Rules

A number of integrals may be formed from combinations of the structure functions. Such integrals, taken over a range $[0, 1]$ in x , are known as moments. The n th moment of an arbitrary structure function $f(x)$ is

$$\Gamma_n \equiv \int_0^1 x^{n-1} f(x) dx. \quad (2.49)$$

A theoretical prediction of the value of a moment is known as a *sum rule*.

For E155 the unpolarized structure functions, $F_1(x, Q^2)$ and $F_2(x, Q^2)$, are considered known quantities, measured in past experiments. For this reason the sum

rules of the unpolarized structure functions that may be tested in an electron beam experiment – the momentum sum rule (Equation 2.34) and the Gottfried sum rule [24] – will not be discussed. However, there are sum rules involving the polarized structure functions that may be examined by E155.

The most famous and most experimentally tested prediction is certainly the Bjorken Sum Rule [25]. Developed before the Quark Parton Model, it uses axial currents in the baryon sector and isospin symmetry to predict the integral of the difference of the first moments of the proton and neutron

$$\Gamma_1^p - \Gamma_1^n = \int_0^1 g_1^p(x) - g_1^n(x) dx = \frac{1}{6} \left| \frac{g_A}{g_V} \right|_{np} \quad (2.50)$$

From Equation 2.46, this sum can be connected to $(F + D)$.

Equation 2.50 is valid in the infinite Q^2 limit, also known as the *scaling limit*. At the finite Q^2 of a real experiment, the prediction gains a non-singlet QCD radiative correction. For three active quark flavors, the multiplicative correction has been calculated to be [26]

$$C_{NS} = 1 - \left(\frac{\alpha_s(Q^2)}{\pi} \right) - 3.5833 \left(\frac{\alpha_s(Q^2)}{\pi} \right)^2 - 20.2153 \left(\frac{\alpha_s(Q^2)}{\pi} \right)^3 + \mathcal{O}(\alpha_s^4). \quad (2.51)$$

Although Bjorken described his sum rule as a “useless equation” when he derived it because polarized deep inelastic scattering experiments were not within the technology of the time, it has since been said that if the Bjorken Sum Rule is wrong, then all of QCD is wrong. It is thus viewed as a very fundamental test, and has not been shown to be violated by any experiment to date.

Another set of sum rules is from Ellis and Jaffe [27, 28]. They predict values for the first moments of g_1^p and g_1^n separately. The Ellis-Jaffe predictions use the

Operator Product Expansion (OPE) [29], a technique designed to separate the virtual photon cross sections into two parts: one which may be treated with perturbative QCD (pQCD) and another involving long-range processes unsuitable for treatment by pQCD and for which matrix elements are sought.

In the quark parton model, the integral of $g_1^p(x)$ is given by Equation 2.39

$$\int_0^1 g_1^p(x) dx = \frac{1}{2} \sum e_i^2 \Delta q_i \quad (2.52)$$

$$= \frac{1}{2} \left(\frac{4}{9} \Delta q_u + \frac{1}{9} \Delta q_d + \frac{1}{9} \Delta q_s \right). \quad (2.53)$$

Using Equations 2.41 through 2.45, this may be expressed as

$$\int_0^1 g_1^p(x) dx = a_3 + a_8 + a_0 \quad (2.54)$$

$$= \frac{1}{12}(F + D) + \frac{5}{36}(3F - D), \quad (2.55)$$

where the assumption made by Ellis and Jaffe is that $\Delta q_s = 0$, that is, the strange sea quarks present in the proton do not contribute to the proton spin.

Again, the above expression is valid only in the scaling limit. A singlet and a non-singlet QCD radiative correction modifies the prediction of the Ellis-Jaffe sum rule. The non-singlet correction is given in Equation 2.51, above. The singlet correction has been calculated to be [30]

$$C_S = 1 - 0.3333 \left(\frac{\alpha_s(Q^2)}{\pi} \right) - 0.5495 \left(\frac{\alpha_s(Q^2)}{\pi} \right)^2 + \mathcal{O}(\alpha_s^3). \quad (2.56)$$

The radiatively corrected Ellis-Jaffe sum rule is then

$$\Gamma_1^p = C_{NS} \left[\frac{1}{12} (F + D) + \frac{1}{36} (3F - D) \right] + C_S \frac{1}{9} (3F - D). \quad (2.57)$$

Chapter 3

Experimental Setup

3.1 Beam and Beamline Components

The polarized beam at SLAC begins with a polarized source, then accelerated eastward for approximately 3 km, bent through a 24.5 degree angle, delivered to the physics target in End Station A, and finally absorbed in Beam Dump East. A schematic of the beamline and experimental regions available at SLAC is presented in Figure 3.1. The following sections detail the equipment involved in each stage of this process.

3.1.1 Source

The source used in E155 was based on a strained GaAs crystal illuminated by circularly polarized laser light produced by a flashlamp-pumped Ti:sapphire laser [31]. Bulk GaAs is an efficient photo-emitter in the infrared range. This is possible due to a transition from a $P_{3/2}$ valence band state to a $S_{1/2}$ conduction band state. With the proper laser frequency, two transitions can occur: one from a $(j = \frac{3}{2}, m_j = \pm\frac{1}{2})$ state to a $(j = \frac{1}{2}, m_j = \mp\frac{1}{2})$ state, and another from $(\frac{3}{2}, \pm\frac{3}{2})$ to $(\frac{1}{2}, \pm\frac{1}{2})$, where the upper

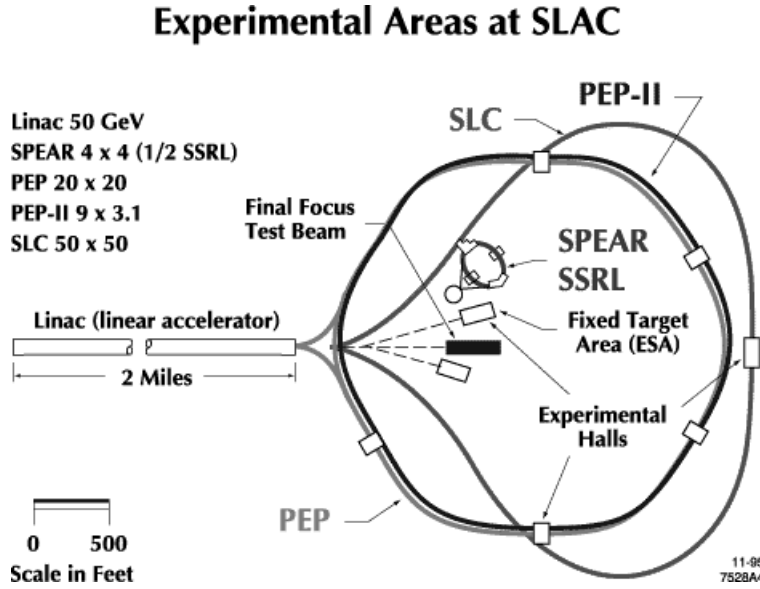


Figure 3.1: Facilities at SLAC.

signs represent transitions possible with left circularly polarized light, and the lower signs those with right circularly polarized light. Other transitions are suppressed due to the $\Delta m_j = \pm 1$ selection rule. This results in a maximum theoretical polarization of 50%, due to the fact that the $(\frac{3}{2}, \pm\frac{3}{2}) \rightarrow (\frac{1}{2}, \pm\frac{1}{2})$ transition occurs three times as often as the $(\frac{3}{2}, \pm\frac{1}{2}) \rightarrow (\frac{1}{2}, \mp\frac{1}{2})$ one.

If the GaAs is grown as a thin film on a GaAsP substrate, a tensile strain is created that causes the degeneracy of the $m_j = +\frac{1}{2}$ and $m_j = \frac{3}{2}$ states to be broken. It is then possible to tune the laser frequency to select only one of the two transitions, and, by using 100% circularly polarized light, a maximum polarization of 100% is theoretically possible. During production running of E155 the polarization measured in the End Station was typically in the 80% range.

By switching the direction of the circular polarizer of the laser light, the helicity of the electrons emitted from the crystal may be controlled. This was done on a pulse-by-pulse basis under control of a pseudo-random bit generator. The algorithm

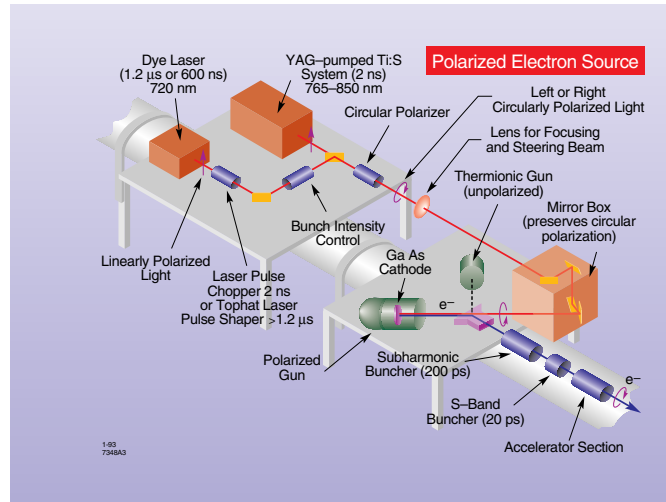


Figure 3.2: Components of the Injector and Polarized Source.

used was deterministic, such that if the values of 33 consecutive bits were known, the values of all successive bits could be predicted.

The laser light was applied for a duration of 200-400 ns, a value required for use in the linac when in “SLED” mode, described below. The power of the laser was moderated in such a way that, after beam loading in the linac took place, each beam spill had an even charge distribution when entering the End Station.

3.1.2 Beamline

Linac

The acceleration of the electrons to their delivered energy of 48.35 GeV was the responsibility of the linear accelerator, or linac. This is a pulsed machine approximately 3 km in length, consisting of 30 sectors, with each fed by eight 2.856 GHz klystron tubes. The microwave energy produced by the klystron was delivered to a disk-loaded copper accelerating cavity, through which the beam passed.

For beam energies above the original design limit of 30 GeV, a technique known

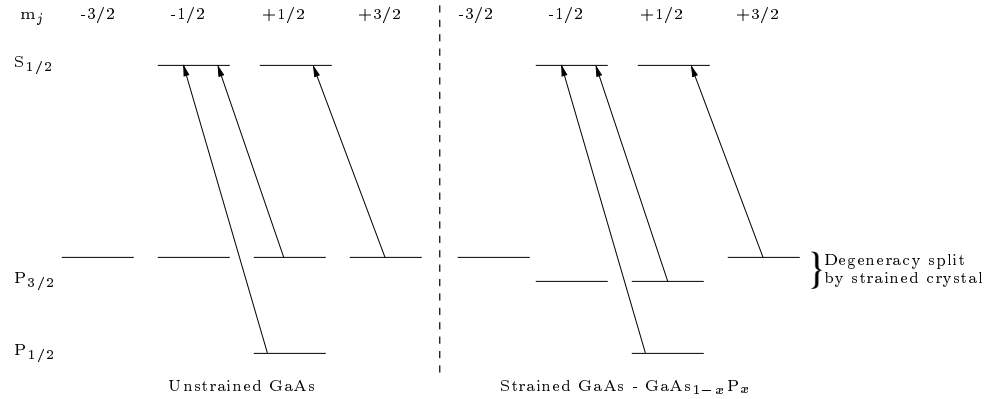


Figure 3.3: Energy states in unstrained and strained GaAs. Taken after [31].

as the SLAC Energy Doubler [32], or SLED, is used. The SLED method uses a pair of resonant cavities to store microwave energy, and a sudden reversal of the phase of the klystron output to cause the microwave power delivered to the accelerating cavity to be approximately twice the original value. One consequence of using this technique is that the length of a beam spill is reduced from 2 to 3 μs to 200 to 430 ns.

A-line

The last section through which the electrons pass before delivery to End Station A is known as the A-line. This part of the beamline is responsible for bending the beam 24.5 degrees to the north of its eastwardly trajectory along the linac. The first half-degree of bend is provided by pulsed dipole magnets, while the remaining 24 degrees by a set of 6 pairs of dipoles.

The A-line contains two massive, water-cooled collimators; one immediately downstream of the pulsed magnets (known as D-10) and another after the first 3 pairs of bending dipoles (known as SL-10). The jaws of these collimators are adjustable, allowing the energy variation of the electrons permitted through them to be set. In E155, SL-10 was set to allow a 1% $\Delta E/E$ energy spread.

Just upstream of the SL-10 collimator, in the middle of the 5th bend magnet, a video camera allows monitoring of the synchrotron light emitted as the beam is bent by the magnet. The angle at which this light is emitted varies with the amount of bend that the electrons undergo in the dipole, which is a function of their energy. The camera can be gated to take a snapshot of this light at any time during the spill. By varying the timing of this gate and observing the variation in position of the light hitting the camera, a profile may be made showing the energy of the electrons vs. their place within the spill. In addition to being a very helpful tool for the operators in tuning the linac, this monitor also gives an indication of the total energy spread of the spill. The measured value for this energy spread was typically around 0.5%, or half the spread that would be allowed by the setting of the SL-10 collimator. This is consistent with observations that very little energy was deposited in the collimator.

The absolute beam energy delivered to the End Station is determined by the field strength in the 12 A-line dipoles. There is a 13th dipole, with properties very close to the average of the other 12, installed out of the beamline in a control building, but connected in series with the the 12 magnets in the A-line. A flip coil installed in its bore allows accurate measurement of its field, and therefore the field of each of the A-line magnets.

As the beam makes its bend through the 24.5 degrees, it loses a small amount of energy due to synchrotron radiation, around 1% for a 50 GeV beam. As a result, the beam passing through the upstream magnets was more rigid and required a greater integrated field to produce the necessary deflection. The strengths of the magnets were adjusted in pairs with individual trim coils mounted in each dipole magnet.

At the exit of the linac the electrons are longitudinally polarized. As they undergo the 24.5 degree bend in the A-line, their spins precess by an amount dependent on the bend angle and the beam energy:

$$\theta_{\text{prec}} = \gamma \left(\frac{g-2}{2} \right) \theta_{\text{bend}} \quad (3.1)$$

where γ is $(1 - v^2/c^2)^{-\frac{1}{2}}$, and g is the gyromagnetic ratio of the electron, $(g-2)/2 = 1.159 \times 10^{-3}$ [22]. Since the experiment is designed to have longitudinally polarized beam at the target (after all bending in the A-line is complete), the total precession must be an integral multiple of π . This condition limits the energy deliverable at the target to fixed values, determined by the precession equation. A target energy of 48.3 GeV was the largest of these *magic energies* that the upgraded accelerator could produce. This corresponded to a total precession of 15π , and an accelerator energy of 48.7 GeV [33].

A cross-check of the energy measurement using the flip coil discussed above utilized the spin precession in the A-line. At the beginning of the experiment, a series of Møller polarimeter runs were made in which the beam energy was changed in small steps in a region about the nominal value (see Section 3.1.5 for a discussion of the Møller polarimeter). For each step, the beam polarization in the End Station was measured by the polarimeter. The energy setting that gives the maximum longitudinal polarization is the desired value for use in the experiment. The value measured by this technique (Figure 3.4) was in excellent agreement with the value obtained by the flip-coil measurement, differing by only 40 MeV, or 0.08%, and validated some corrections made to the flip coil to account for an unsampled stray field region and for a difference in support structures that slightly alters the field strength.

One final function is also performed by the A-line. Since most of the beam steering instrumentation of the linac, as well as the control electronics to read it out, is set up to monitor the very short, intense bursts (2 ns, $6 \times 10^{10} e^-/\text{spill}$) of beam used in the SLAC Linear Collider, its performance with the long-pulse, low current (200-

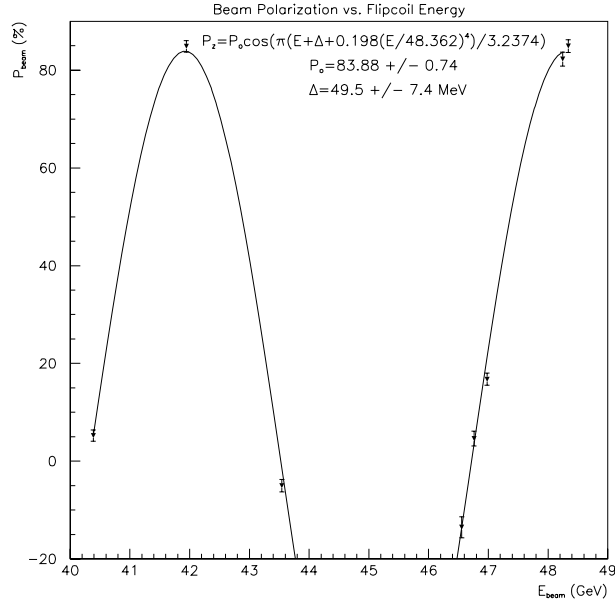


Figure 3.4: Results of Møller energy scan.

400 ns, $2 - 4 \times 10^9 e^-$ /spill) beam used for solid target experiments is very poor. To remedy this, once a *witness pulse* of 2 to 5 ns and $5 \times 10^9 e^-$, created by the illumination of the cathode with a separate laser, was sent through the linac. This pulse had sufficient charge density that the beam position monitors could sense it, but because of the high charge density it was unsuitable for use in the End Station. The pulsed magnets, mentioned above, were then employed to steer this witness pulse to the dump D-10, at the beginning of the A-line, while the remaining 119 pulses per second were allowed to pass through to the End Station.

3.1.3 Beamline Components in End Station A

In addition to standard beam monitoring devices located elsewhere in the beamline, the End Station had several other devices with which to monitor the beam.

Two zinc-oxide coated screens, positioned upstream of the target, allow visual monitoring of the beam. Each screen can be moved into the beamline and the position of the beam spot observed through a video camera. This allows a determination not only of beam position, but also of spot size and shape, and was useful as a test for the beam scraping the beam pipe at any upstream position.

Two scintillator paddles positioned immediately downstream of the target, known as the goodspill and badspill monitors, can also be used for beam diagnostics, as well as during normal running. One is located at a small forward angle to the target (goodspill) and the other at a large scattering angle (badspill), allowing target luminosity to be monitored. If the beam is properly steered, scattering occurs only from the polarized target. This produces a great amount of forward scattering and thus a large signal in the goodspill paddle, and a small amount of large-angle scattering, and thus very little signal in the badspill paddle. Missteering of the beam results in scattering from the beam pipe upstream of the target, which produces large signals in both paddles. Data from these monitors was used to determine beam quality, and cuts on the values read were part of the standard electron definition.

Downstream of the spill monitors, a foil array measures the exact position of the beam in both the x and y directions. The spacing of the individual foils is small enough to allow a quantitative determination of spot size, as well as spot position. This data was also used in the beam cuts of the electron definition.

Beam current was measured by two toroid coils, each mounted upstream of the target. The ADCs that read the coils were calibrated by a loop of wire passing through the coils. Several times a day a known current of approximately 40 nA was passed through this wire and the ADC values read.

In addition to these beam monitoring devices, a Møller Polarimeter, consisting of a target, a magnet, and a set of detectors, was also located in the End Station.

Details of the arrangement of this equipment are given in Section 3.1.5.

3.1.4 Dump

After passing through the End Station, the beam is absorbed into Beam Dump East, a high-power, water-cooled device located in a tunnel in the side of a hill.

3.1.5 Møller Polarimeters

The accuracy with which the beam polarization is known factors directly into the error on the asymmetry measurements, so a great deal of effort was spent to perform the best beam polarization measurement possible. E155 performed this measurement with both a single arm and a double arm Møller polarimeter. The theory of Møller polarimetry will be presented first, followed by a description of the equipment used to conduct the measurement.

In spin-correlated elastic electron-electron scattering (Møller scattering), a cross-section asymmetry exists between cases when the two electron spins are in the same direction and when they are pointing opposite each other. By measuring this asymmetry, and knowing the beam energy and polarization of the electrons in the Møller target, the beam polarization can be accurately determined.

From QED calculations, and using high-energy ($1/\gamma \ll 1$) approximations, the lowest order expression for the unpolarized electron-electron cross section in the lab frame is [34]

$$\frac{d\sigma_0}{d\Omega} = \left[\frac{\alpha(1 + \cos \theta_{cm})(4 - \sin^2 \theta_{cm})}{2m \sin^2 \theta_{cm}} \right]^2. \quad (3.2)$$

The cross section for polarized scattering can be expressed in terms of the unpo-

larized cross section and nine asymmetry terms

$$\frac{d\sigma}{d\Omega} = \frac{d\sigma_0}{d\Omega} \left(1 + \sum_{i,j} P_B^i A_{ij} P_T^j \right) \quad (3.3)$$

$$A_{xy} = A_{yx} = A_{yz} = A_{zy} = 0 \quad (3.4)$$

$$A_{xz} = A_{zx} = -\frac{2 \sin^3 \theta_{cm} \cos \theta_{cm}}{\gamma(4 - \sin^2 \theta_{cm})} \quad (3.5)$$

$$A_{xx} = -A_{yy} = -\frac{\sin^4 \theta_{cm}}{(4 - \sin^2 \theta_{cm})} \quad (3.6)$$

$$A_{zz} = -\frac{\sin^2 \theta_{cm} (8 - \sin^2 \theta_{cm})}{(4 - \sin^2 \theta_{cm})}. \quad (3.7)$$

Measurement of this scattering asymmetry can be done by observation of both incident and struck electrons in coincidence (double-arm Møller), or by observation of only one of the scattered electrons (single-arm Møller). Double-arm measurements have the advantage of being largely insensitive to background from Mott scattering, which can have a cross section more than ten times larger than the Møller cross section [35]. The disadvantage of double-arm measurements, especially for experiments like E155 that feature low duty-factor beams, is the demands placed on the electronics to handle high instantaneous rates. Detector segmentation and adequate shielding are ways to reduce these rates.

In single-arm measurements, it is necessary to make an adequate determination of the background so that it may be subtracted to get the true scattering asymmetry. Determination of this background presents an additional source of error.

At a center-of-mass scattering angle of 90° , the $A_{xz} = A_{zx}$ terms vanish, while the remaining terms reach maxima: $A_{xx} = -A_{yy} = -1/9$, and $A_{zz} = -7/9$. Most double-arm detectors are designed so that 90° center-of-mass scattering is in the middle of their acceptance. For single-arm devices, detectors are usually positioned

so that their acceptance is either entirely above or entirely below the 90° point. This is so that only one of the Møller electrons is seen. If the detector spanned the 90° center-of-mass scattering angle, both incident and struck electrons would fall within the acceptance and double counting would occur.

Most Møller detectors use a magnetized iron-alloy foil as the source for the target electrons. The direction of magnetization can be in the plane of the foil, in which case a field of a few mT is adequate, or it may be perpendicular to the foil, requiring a field of at least 2.2 T to cause saturation of the spins. The overall electron polarization is typically in the range of 7 to 9%.

With in-plane magnetization, the foil plane must be inclined relative to the beam axis by some angle, resulting in a $\cos^2 \theta$ decrease in the measured asymmetry. With out-of-plane magnetization, superconducting magnets are generally required, adding to the cost and complexity of the polarimeter. The E155 Møller used in-plane magnetization.

One important aspect of the analysis of the scattering data is consideration of the initial atomic motion in the struck electron. The effects of this initial momentum, known as the *Levchuk Effect* [36], were ignored in Møller analysis until 1992, but can result in corrections as high as 20% to the final asymmetry [37].

Stated briefly, the effect arises from a variation in the distribution of the scattering angle with the initial shell state of the target electron. The inner-shell electrons are on average unpolarized (they are paired), and have a relatively large transverse momentum and thus a relatively broad distribution of scattering angles. The unpaired electrons, which give rise to the observed asymmetry, populate outer shells, have relatively low transverse initial momentum, and thus scatter to a more narrow range of angles. The analysis of both Møller detectors in E155 included Levchuk corrections.

Single Arm Polarimeter

The single arm polarimeter [38, 39] used for Møller measurements was an evolved form of the systems used in the past three spin physics experiments in End Station A. It consisted of a target, collimators, a bending magnet, and a detector hut.

The Møller target was made from a foil of Permendur – a polarizable metal consisting of 49% Iron, 49% Cobalt, and 2% Vanadium. Thickness varied among the six targets used, ranging from 20 μm to 154 μm . The atomic electrons were then polarized using Helmholtz coils placed around the target, producing a magnetic field at the target center of 0.01 T, which magnetized the foil almost to saturation. These foils were mounted in a movable ladder, which itself was mounted so that the plane of the foil made a 20.7° angle with respect to the path of the incoming beam. It is desirable that this angle be kept as small as possible because the atomic electrons in the foil polarize in a direction pointing along the foil plane, whereas the beam electrons are polarized along the beam axis.

The acceptance of the Møller detector was defined by a tungsten collimator placed approximately 10 m downstream of the foil target. Holes for scattered electrons were placed above and below the hole for the beam, each covering a vertical angle (θ) from 3.59 mrad to 8.96 mrad and a width (ϕ) of 0.20 rad for scatters above the beam and 0.22 rad below the beam. Since these angles are so small, a dipole magnet containing a centrally mounted shielded septum was used to bend the scattered electrons to a detector hut 28.9 m from the target, while allowing the unscattered beam to pass through a region of very small field.

The detector package for the single arm polarimeter consisted of five silicon strip detectors, each measuring 4 by 6 cm (x by y) by 300 μm thick. The Top Detector, consisting of a single pad segmented into 48 channels of 2.18 mm each, registered

electrons scattered above the beam. It was mounted behind a lead shield 19.1 mm thick, and inclined by an angle of -12.5° as seen by the beam in order to align the detector segments with the Møller stripe of scattered electrons. This detector was mounted on a remotely-controlled xy mover so that the portion of the Møller stripe that it saw could be adjusted. The Bottom Detector consisted of the remaining four pads, each segmented into 12 channels 8.69 mm tall. It was mounted behind a lead shield 12.7 mm thick and inclined by an angle of $+10.2^\circ$ so as to be aligned with the stripe of Møller electrons scattered below the beam. Typically the top detector saw scatters at 94° in the center-of-mass frame, while the bottom detector saw a range from 93 to 104° .

The outputs of the silicon detectors were sent to preamplifiers, which integrated the charge seen over the entire beam spill (220 to 420 ns). These signals were then read by highly linear ADC's at the end of each spill and, along with pertinent beam information, sent to tape.

Double Arm Polarimeter

The double arm polarimeter operated with the same target, collimation, and bending magnet as the single arm, but with a detector package of lead glass, mounted immediately behind the silicon pads used for the single arm.

The degree of segmentation of the detector is a direct requirement of the need to keep the singles rates in each element down to a reasonable level. This problem was exacerbated by the fact that the use of the SLED technique shortened the spill length by almost an order of magnitude compared to the spill length obtained when lower energy beams, not utilizing the SLED technique, are produced.

The double arm polarimeter provided an excellent cross-check on the measurement of the beam polarization.

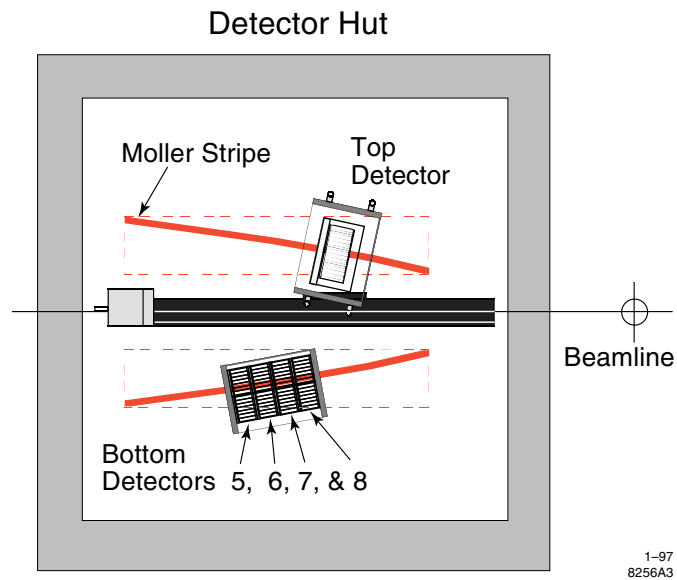
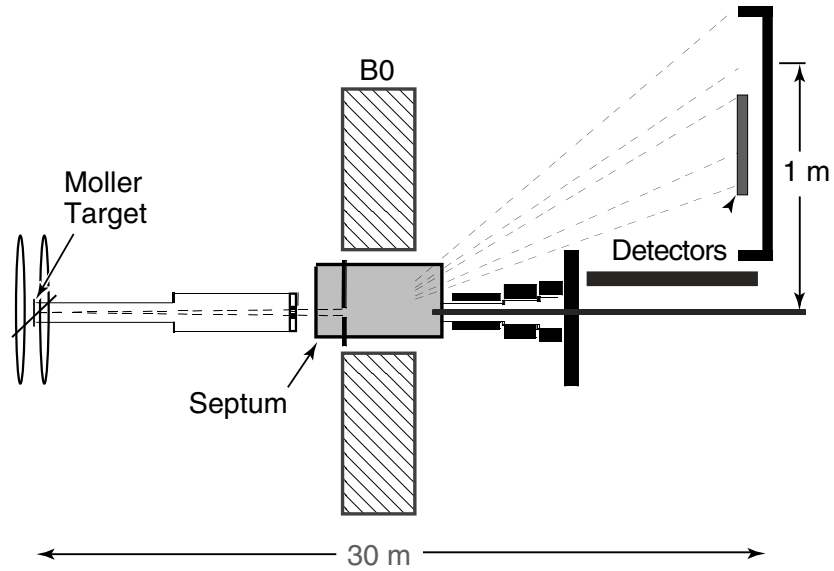


Figure 3.5: Components of the Møller Detectors. Taken from [39].

3.2 Spectrometers

For detection of the scattered beam electrons, three spectrometers were used for particle identification and momentum measurement. Each consisted of several planes of hodoscopes, at least one Čerenkov tank, and a lead glass shower calorimeter. Figure 3.6 shows the layout of the spectrometers on the floor of End Station A. Figure 3.7 shows the kinematic coverage of the spectrometers in x and Q^2 . Each spectrometer element is discussed separately below.

3.2.1 Optics

Several considerations went into determining the best optics design for the spectrometers. To gain access to data in the low- x region and to maximize the count rate, the highest deliverable beam energy was used and the smallest practical scattering angle. To keep statistical errors low, a large acceptance is desirable. At odds with these requirements, overall rates in the detector need to be kept to a level which the electronics could handle, with the majority of the particle tracks coming from π^- electro-produced in the target.

Each of the above needs were met nicely by an “S-bend” optics configuration, which was used for the 2.75° and the 5.5° spectrometers. This approach uses two magnetic dipoles, both bending in the vertical (non-scatter) plane but in opposite directions. In a more traditional design, both dipoles bend in the same direction. There are two advantages to the S-bend geometry. First, since the magnets bend in opposite directions, the detector elements can be placed on the floor of the End Station, instead of requiring the construction of a large detector hut. Second, a “two-bounce” geometry can be created in which a neutral particle has to scatter off the sides of the magnets or collimators twice before being able to strike the detector plane;

E155 Spectrometers

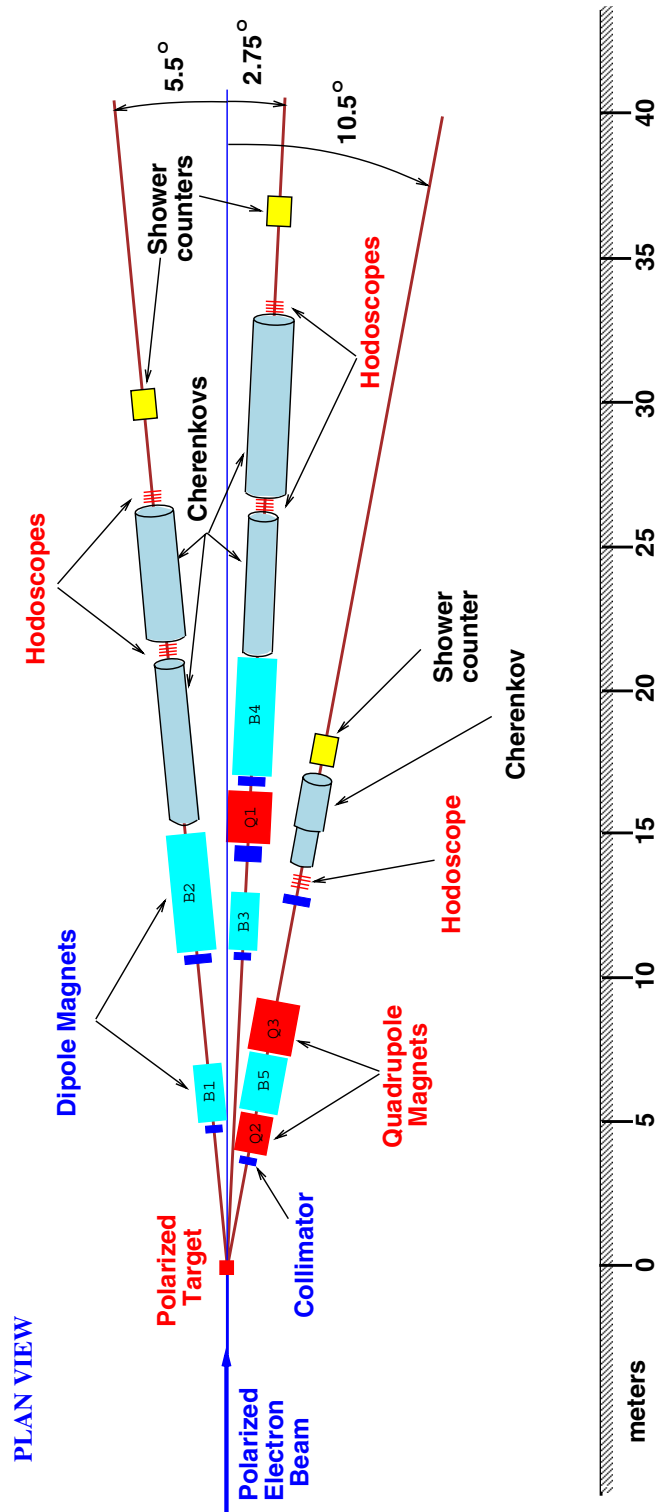


Figure 3.6: Layout of Spectrometers in ESA.

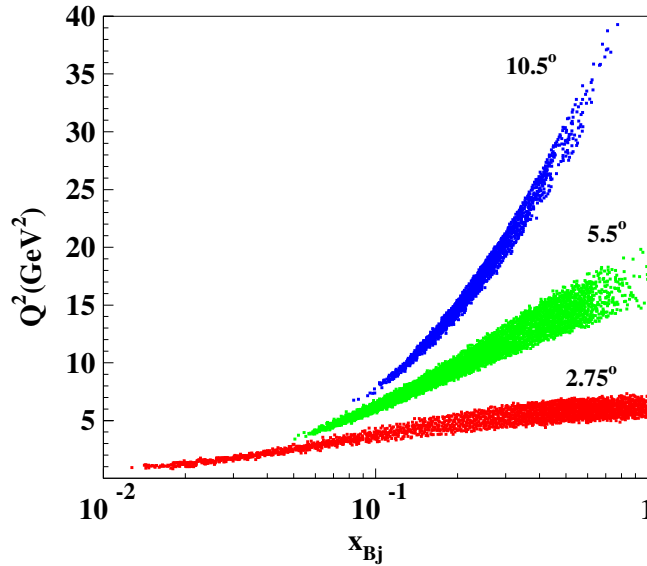


Figure 3.7: Kinematic coverage of the E155 spectrometers at 48.3 GeV.

. In addition, such an arrangement helps provide a larger acceptance over the full range of momenta.

The 2.75° spectrometer [40], which sat on the south side of the beamline, features an 18D72 magnet as its first dipole, B3, and the B82 magnet from the SLAC 8 GeV spectrometer, named B4 for this experiment, as the second dipole. Due to the high rates that this spectrometer would be subject to, a quadrupole, Q1, was installed between the two dipoles to provide defocusing in the horizontal (non-bend) plane. This helped to spread particles across the entire width of the detectors, while the bend-plane focusing distributed low-momentum particles over most of the height of the spectrometer.

Due to the small central angle of this spectrometer, it was necessary to position its steering magnets approximately 10 m away from the target. The other two spectrometers, being at larger angle, had their magnets positioned closer to the target. The result of this situation is that scattered electrons destined for the 2.75° spectrom-

eter's acceptance were vulnerable to the effects of fringe fields from the other two spectrometers' magnets. To avoid mis-steering these particles, a large, iron shielding pipe was installed, extending from near the target exit window downstream to the entrance of the B3 dipole.

The 5.5° spectrometer [41] also used an 18D72 as its first dipole, B1, and the B81 magnet from the SLAC 8 GeV spectrometer was renamed B2 and used as the second dipole. Since this spectrometer sat at a relatively larger angle, rates in its detectors were not as high as in the 2.75° spectrometer, so a quadrupole was not needed between the dipoles. This spectrometer sat to the north of the beamline.

The 10.5° spectrometer was a new addition for E155[42]. It was added to provide additional data to measure the Q^2 evolution of the polarized quark and gluon distribution functions. The physical space in which the spectrometer could be placed was limited to the area between the target and the beginning of the shielding hut for the 2.75° spectrometer. As such, some compromises were necessary in the optics and detector package in order to keep the overall length of the spectrometer within these constraints.

The magnetic elements of the 10.5° spectrometer [43] consisted of two quadrupoles and a dipole. Q2, the Q81 magnet from the SLAC 8 GeV spectrometer, provided defocusing in the vertical plane. Following that B5, an 18D72, bent particles downward, after which Q3, the Q82 magnet from the SLAC 8 GeV spectrometer, focused in the bend plane.

The result was a spectrometer that has an acceptance ranging from approximately 9° to 12° , covering a Bjorken x range of $0.09 < x < 0.94$, and a Q^2 range of $7 < Q^2 < 47$ (GeV/c)².

3.2.2 Hodoscopes

Hodoscopes were used to provide tracking information in each of the spectrometers. In the 2.75° and 5.5° spectrometers, two sets of hodoscope planes were used, the first between the two Čerenkov detectors and the second between the second Čerenkov detector and the shower counter. Each set of planes contained fingers oriented in the \hat{x} and \hat{y} directions, as well as planes whose fingers were oriented in two directions tilted relative to those axes (known as \hat{u} and \hat{v}). Further, the 2.75° spectrometer had a set of four planes upstream of the first Čerenkov detector.

All fingers of all hodoscope packages were equipped with a photomultiplier tube on one end, which was connected to a discriminator and then a multihit time-to-digital converter.

3.2.3 Čerenkov Counters

To separate electrons from the background of pions and other particles, Čerenkov detectors were used in each of the spectrometers. The 2.75° and 5.5° spectrometers each had two detectors, whereas the 10.5° spectrometer, due to space limitations, had only one.

In previous experiments, the same four tanks used in the 2.75° and 5.5° spectrometers were run with pure nitrogen gas, N_2 . Nitrogen scintillates, leading to scintillation light hitting the photomultipliers and being mistaken for Čerenkov light. To help avoid this problem, studies were made [44] before the running of E155 to find a gas that could be added to the nitrogen that would quench some of this scintillation light, while being transparent to the Čerenkov light. The result of this effort was the decision to use a mixture of 90% N_2 and 10% CH_4 in all tanks. Studies after the experiment on production data [45] show that there was indeed no noticeable reduc-

tion in the amount of Čerenkov light hitting the PMT, and that there was a 46% reduction in the scintillation light.

The pressure in the tanks was chosen [46] based on the measured temperature and the desired momentum at which the π^- detection efficiency turns on [47]. This value was typically set just below the central momentum setting for the spectrometer.

3.2.4 Lead Glass Detector

The final component of each spectrometer was a shower calorimeter made of $6.2 \times 6.2 \times 75$ cm blocks of F2 lead glass, arranged in a grid of 10 blocks horizontally by 20 blocks vertically. Each block was arranged with its long axis in the direction of flight of electrons, and was fitted with a 2 inch phototube on its downstream face.

The phototube signal was split and sent to an ADC and to at least one Discriminator/TDC pair. The ADC was gated to measure the integral of the PMT signal over the entire beam spill, thus allowing a measurement of the total energy deposited in each block during the spill.

The discriminator/TDC arrangement in turn allowed determination of how many hits the block received. The time (in ns relative to the beginning of the spill) at which the phototube signal rose above a set discriminator threshold was recorded, as was the time the signal dropped back below that threshold. If this happened several times during a spill, the times of each threshold traversal were recorded. Blocks that, due to the optics of the spectrometer, were expected to receive higher rates were equipped with two or three of these discriminator/TDC pairs – each pair with a higher discriminator threshold than the previous – so as to avoid loss of data due to discriminator saturation. By profiling the heights of the phototube signal vs. time in this way, it is possible to characterize the types of particle that caused the signal.

3.2.5 Electronics

Due to the relatively short duration of the beam spill at SLAC (typically 400 ns or less), the 120 Hz repetition rate, the number of detector elements needing to be read, and the average number of hits occurring in those elements, the readout system for E155 had to be capable of both high instantaneous data rates and relatively high sustained transfer rates [48].

To accomplish the first requirement, the system was designed to be triggerless. At the start of the beam spill, a gate opened enabling all of the modules to take data. At the end of the spill, the gate closed and the modules were read out.

Each of the hodoscope fingers was equipped with one photomultiplier tube which fed into a channel on a TDC (time to digital converter) module.

Each Čerenkov tank had a single photomultiplier tube to collect the Čerenkov light. The signal from this tube was digitized with a resolution of 1 ns by a Flash ADC module. In addition, the signal was fed into a TDC.

Almost all of the modules used were conformant to the CAMAC interface standard, with the exception of the Flash ADC modules used with the Čerenkov tanks, which were VME modules. After the end of each spill, all modules were read into VME memory modules, one for the modules used in the 2.75° spectrometer and one for those used in both the 5.5° and 10.5° spectrometers. The memory modules implemented a reflective memory scheme, meaning that they copy their contents to companion modules to which they are connected with a network cable. In the case of E155 this network cable ran up to the counting house, where a companion memory module was located. In this way, the data from all three spectrometers was copied automatically to a device outside the radiation area.

A dedicated computer running a real time operating system read the memory

module in the counting house and distributed the data to various other machines for monitoring of the experiment and storage of the data to tape.

Chapter 4

Polarized Target

The polarized target used in E155 will be discussed in detail in this chapter. An introduction to the theory of polarized targets begins the chapter, including discussion of dynamic nuclear polarization (DNP) and the operation of the NMR system used to measure the target polarization. Section 4.2 then provides a description of the experimental setup of the equipment used in the target, and of target operations. Finally, Section 4.3 presents the analysis procedure used to turn the data acquired from the target into polarization measurements, concluding with a detailed description of a problem encountered with the NMR system and its resolution.

4.1 Theory of Solid Polarized Targets

For the past 40 years, nuclear physics experiments have had access to solid polarized targets of some form. Early materials were typically frozen alcohols, while current materials are often inorganic crystalline solids. Progress in the field of polarized targets has been on two fronts: much higher polarizations are now attainable – over 90% in proton materials and over 40% deuteron materials – and resistance to radi-

ation damage from ionizing beams is now greater. The techniques used to produce polarization have also evolved, but the fundamental theory remains the same.

Unpaired nuclear spins in a solid placed in an external magnetic field will tend to align themselves with the direction of this magnetic field. The degree of this alignment depends on the strength of the magnetic field, B , the temperature of the material, T , and the spin of the particles in question, J . The simplest measure of this alignment is known as the *vector polarization*, P , of the material, and is defined as

$$P = \frac{\sum j_i N_i}{J \sum N_i}, \quad (4.1)$$

where the sum is over the $(2J + 1)$ orientations of the spin along the axis of the magnetic field (taken here as the z -axis), J_z is the projection of \vec{J} onto the z -axis, and N_i is the total number of nuclei in this state.

The cause of this alignment of the spins is the interaction of the magnetic moments of the nuclei with the magnet field. The energy of this interaction is $\vec{\mu} \cdot \vec{B}$, where $\vec{\mu}$ is the magnetic moment of the nucleus. Following a general technique of Statistical Mechanics, the *partition function* of such a nucleus can be expressed as

$$Z = \sum_{J_z=-J}^J e^{\mu B_z J_z / kT} \quad (4.2)$$

where k is Boltzmann's Constant and T is the temperature, to be discussed more fully below.

The polarization of a system of these nuclei is then

$$P = \frac{\partial Z}{\partial(\mu B / kT)} \quad (4.3)$$

which can be expressed, after some simplification, as

$$P = \frac{2J+1}{2J} \coth\left(\frac{2J+1}{2J} \frac{\mu B}{kT}\right) - \frac{1}{2J} \coth\left(\frac{1}{2J} \frac{\mu B}{kT}\right) \quad (4.4)$$

where the right hand side of Equation 4.4 is known as the *Brillouin Function*.

For the specific cases of spin- $\frac{1}{2}$, spin-1, and spin- $\frac{3}{2}$ systems, the polarization is therefore

$$P_{1/2} = \tanh \frac{\mu B}{kT}, \quad (4.5)$$

$$P_1 = \frac{4 \tanh \frac{\mu B}{2kT}}{3 + \tanh^2 \frac{\mu B}{2kT}}, \quad (4.6)$$

$$P_{3/2} = \frac{5 \tanh \frac{\mu B}{3kT} + \tanh^3 \frac{\mu B}{3kT}}{3(1 + \tanh^2 \frac{\mu B}{3kT})}. \quad (4.7)$$

An important point to note is the meaning of the temperature, T . This quantity is actually the *spin temperature* of the collection of nucleons in question, not to be confused with the lattice temperature of the material as a whole. The spin temperature is a rigorously defined quantity, and may have a positive or negative value*.

Over time, in a fixed magnetic field and at a fixed lattice temperature, the spins in the material will align themselves such that the spin temperature will be equal to the lattice temperature. This is the *Thermal Equilibrium* (TE) state. When a material has come to thermal equilibrium, the difficult task of measuring the spin temperature can be replaced by the easy task of measuring the lattice temperature. This value can then be used in one of Equation 4.5, 4.6, or 4.7, above. The utility of this will be

*This is a direct result of the total energy of the system having both an upper and lower bound. For a complete discussion of spin temperature, see [49].

recalled in the section on calibration of the NMR system, below.

The conditions typically attainable in the lab are magnetic field strengths on the order of several Tesla and temperatures of 1 K or below. For the example of target material at 5 T and 1 K, the proton polarization would be 0.5%, while that of the electrons in the material would be 99%. This method of polarizing, known as brute force or natural polarization, is itself inadequate for the majority of current target materials.

4.1.1 Dynamic Nuclear Polarization

One highly successful method used to enhance the polarization above that attainable with the brute force technique is known as Dynamic Nuclear Polarization, or DNP [50]. DNP requires that the material be doped with paramagnetic defects, which are usually introduced either chemically or through irradiation. The material used as a proton target in E155, $^{15}\text{NH}_3$, belongs in the latter category. One advantage of many materials that are doped through irradiation is that their polarization degrades less quickly in an ionizing particle beam than that of chemically doped materials. In the case of $^{15}\text{NH}_3$, the result of the irradiation is the production of low concentrations of NH_2 radicals and interstitial electrons in the material.

After the material is doped, the Hamiltonian for a system of one electron and one nucleon in the target material has three terms – a Zeeman term arising from the electron’s magnetic moment, a second Zeeman term from the nucleon’s magnetic moment, and a term representing spin-spin interaction between them:

$$H = \vec{\mu}_e \cdot \vec{B} + \vec{\mu}_n \cdot \vec{B} + H_{ss} \quad (4.8)$$

Ignoring the interaction term H_{ss} for the time being, and taking the exam-

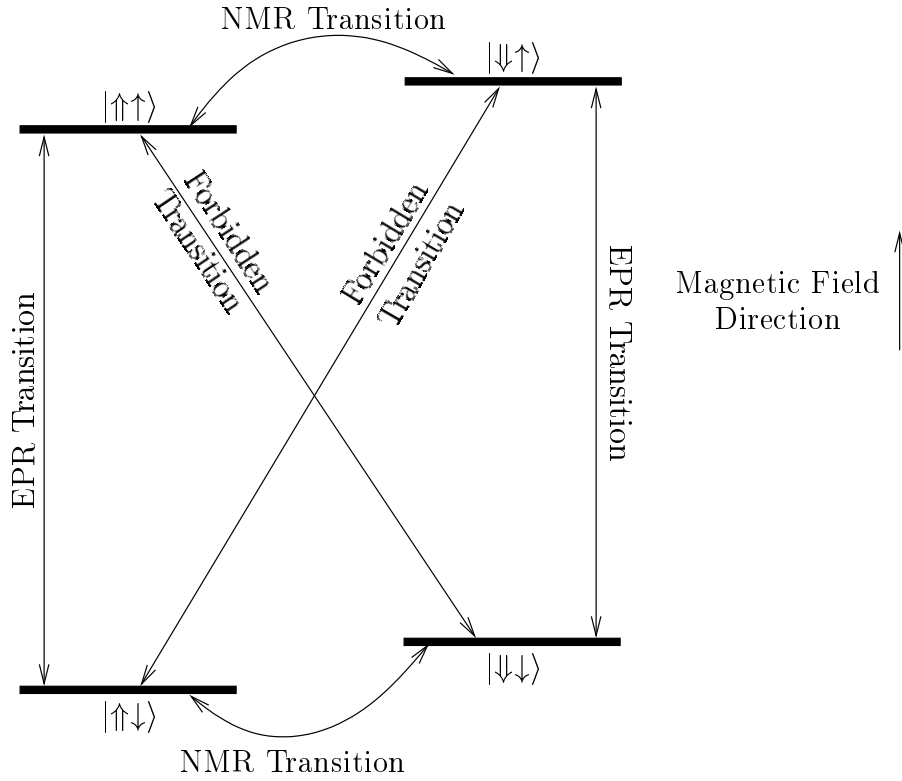


Figure 4.1: Level diagram of a system of one nucleon and one electron in an external magnetic field. Transitions between states are shown, along with their common names. The direction of the nucleon spin is denoted with \uparrow ; electron spin with \uparrow .

ple of a system of a spin- $\frac{1}{2}$ nucleon ($\mu > 0$) and an electron ($\mu < 0$), there are then four pure states: $|\uparrow\downarrow\rangle$, $|\downarrow\downarrow\rangle$, $|\uparrow\uparrow\rangle$, and $|\downarrow\uparrow\rangle$, listed in order of increasing energy, where the double arrow represents the nucleon spin, the single arrow the electron spin, and $|\mu_n| < |\mu_e|$. Figure 4.1 is a diagram of this level structure. There are four allowed transitions, two involving nucleon spin flip (“NMR transitions”) – $|\uparrow\downarrow\rangle \longleftrightarrow |\downarrow\downarrow\rangle$ and $|\uparrow\uparrow\rangle \longleftrightarrow |\downarrow\uparrow\rangle$ – and two involving electron spin flip (“EPR transitions”) – $|\uparrow\downarrow\rangle \longleftrightarrow |\uparrow\uparrow\rangle$ and $|\downarrow\downarrow\rangle \longleftrightarrow |\downarrow\uparrow\rangle$. The remaining two transitions, $|\uparrow\downarrow\rangle \longleftrightarrow |\downarrow\uparrow\rangle$ and $|\downarrow\downarrow\rangle \longleftrightarrow |\uparrow\uparrow\rangle$, are forbidden by dipole selection rules because they represent simultaneous flipping of both nucleon and electron spins, and thus violate $\Delta m_j = \pm 1$.

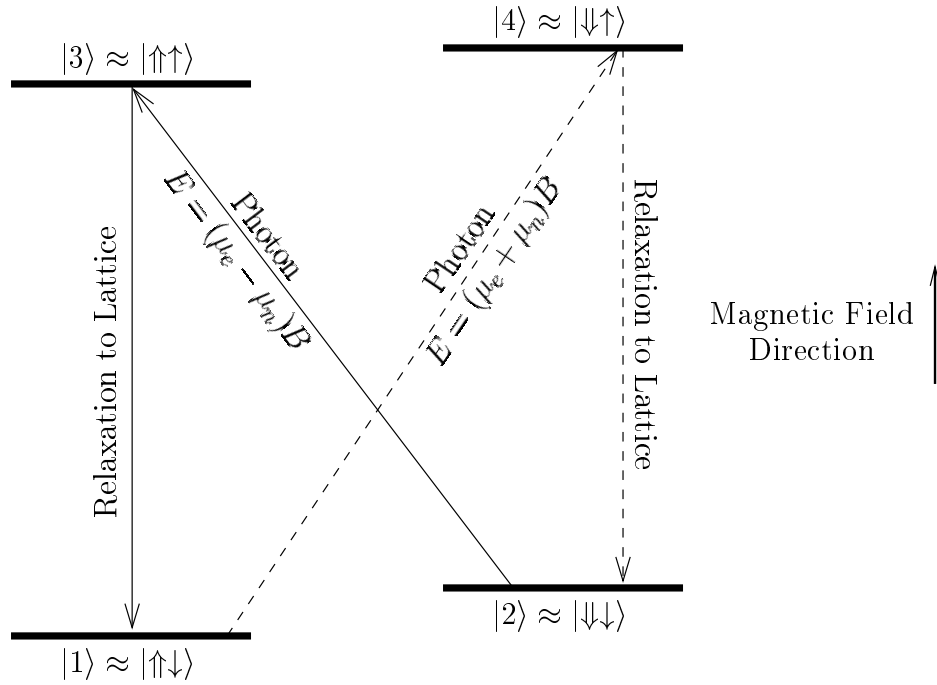


Figure 4.2: Transitions involved in polarization enhancement through Dynamic Nuclear Polarization (DNP).

Because the interaction term H_{ss} does exist, mixing occurs among the pure states as follows:

$$|\uparrow\downarrow\rangle \longrightarrow |1\rangle = c_1 |\uparrow\downarrow\rangle + c_2 |\downarrow\downarrow\rangle \quad (4.9)$$

$$|\downarrow\downarrow\rangle \longrightarrow |2\rangle = c_1 |\downarrow\downarrow\rangle + c_2^* |\uparrow\downarrow\rangle \quad (4.10)$$

$$|\uparrow\uparrow\rangle \longrightarrow |3\rangle = c_1 |\uparrow\uparrow\rangle + c_2 |\downarrow\uparrow\rangle \quad (4.11)$$

$$|\downarrow\uparrow\rangle \longrightarrow |4\rangle = c_1 |\downarrow\uparrow\rangle + c_2^* |\uparrow\uparrow\rangle \quad (4.12)$$

where $c_1 \approx 1$ and $c_2 \ll 1$. It is this mixing that allows the previously-forbidden transitions between the lowest and the highest energy states, and between the two middle energy states. The rates of these two transitions are several orders of magnitude lower than the rates of the EPR and NMR transitions, above.

Consider now that properly prepared material (irradiation doped or chemically doped) is placed into a strong magnetic field and cooled to low temperature. Once the material comes to equilibrium, the brute force or natural polarization is given by one of Equations 4.5 to 4.7. More of the population will be in state $|1\rangle$ than any other state.

If we then bombard the material with photons of frequency $\nu = (\mu_e - \mu_n)B/h$ (typically in the microwave spectrum for many targets), transitions from $|2\rangle$ to $|3\rangle$ will occur. Because the relaxation rate of the electron is typically a few ms, while that of the nucleon is typically tens to hundreds of minutes, almost all the $|3\rangle$ states will then decay quickly to $|1\rangle$ states. In this way, we convert states with anti-aligned nucleons into states with aligned nucleons, using the electron's spin as a vehicle to do so. The result is that the net nuclear polarization of the material increases. This is the principle behind DNP, and is depicted in Figure 4.2.

The same technique produces negative polarization (anti-aligned nucleons) with the use of microwaves of frequency $\nu = (\mu_e + \mu_n)B/h$, which drives the $|1\rangle \rightarrow |4\rangle$ transition, which then decays mostly to $|2\rangle$ states.

The DNP process described above explains how the polarization of an electron is transferred to a nucleon. The range of this electron-nucleon coupling is on the order of several angstroms [51]. An additional mechanism exists whereby the dipole-dipole interaction between two nuclei allows the spin of one nucleon to be transferred to a neighboring nucleon. This process, known as *spin diffusion*, transfers the nuclear alignment to parts of the material that are not near interstitial electrons, and thus allows the material to become polarized even in regions that cannot be polarized directly by the DNP process.

4.1.2 Nuclear Magnetic Resonance

Measuring the polarization of the target material directly is equivalent to measuring the net nuclear magnetization of the substance. Most target systems use continuous wave Nuclear Magnetic Resonance (NMR) techniques to do this.

When placed in a time-varying magnetic field perpendicular to the static external field created by the target magnet, the magnetic susceptibility of the target material is a function of the frequency of the varying field, and can be written as

$$\chi(\omega) = \chi'(\omega) + i\chi''(\omega), \quad (4.13)$$

where χ' is the dispersive and χ'' the absorptive component. It has been shown [52] that the integral over all frequencies of the absorptive component is directly proportional to the polarization of the material[†]. For a given spin species, the absorptive component is generally non-zero only in a small frequency range centered on the Larmor frequency of that species in the static field. To measure the polarization of a given spin species, the integral may then be replaced by an integral over a small region spanning the Larmor frequency of that species.

The most common method of measuring this absorption signal is to place an inductor, known as the NMR coil, in or around the target material. The coil is situated such that it creates a field with a component perpendicular to the static magnetic field. When an alternating current is passed through the coil, the interaction

[†]The exact equation is

$$P = \frac{2}{\mu_0 \pi \hbar \gamma^2 N I} \int_0^\infty \chi''(\omega) d\omega,$$

where γ is the nuclear gyromagnetic ratio, I is the spin of the species being measured, and N is the spin density of the material

of the target material with this field causes the inductance to become

$$L(\omega) = L_0[1 + 4\pi\eta\chi(\omega)] \quad (4.14)$$

where L_0 is the inductance of the coil with the material completely unpolarized and η , known as the filling factor, describes the coupling of the coil's field to the material (based on the geometry of the coil and its proximity to the material), and ranges from 0 to 1. A typical value of η is 0.3 [53]. The impedance of the coil can then be expressed as

$$\begin{aligned} Z_{coil} &= R_{coil} + i\omega L(\omega) \\ &= R_{coil} + i\omega L_0[1 + 4\pi\eta\chi'(\omega) + i4\pi\eta\chi''(\omega)] \\ &= \underbrace{[R_{coil} - 4\pi\omega L_0\eta\chi''(\omega)]}_{Re(Z)} + i \underbrace{[\omega L_0(1 + 4\pi\eta\chi'(\omega))]}_{Im(Z)}, \end{aligned} \quad (4.15)$$

where R_{coil} is the RF resistance of the coil.

Measuring Z_{coil} allows access to χ'' , and thus the polarization. The next section will discuss the operation of the circuit used to perform this crucial step.

4.1.3 Q Meter Operation

The most common method of determining the NMR coil impedance, and the one used in the NMR system of E155, is to place this inductor in series with a capacitor and resistor to form a series-resonant circuit, with the value of the capacitor chosen such that the resonant frequency of the circuit is exactly the Larmor frequency of the spin species to be measured. Part of the circuit used to accomplish this is a module developed at the University of Liverpool, England, known as a Q Meter [54].

As previously mentioned, the fundamental component of the NMR system is a

series RCL circuit. A functional diagram of the Q Meter and some other components is presented in Figure 4.3. A description of the principles of operation of the circuit follow.

The circuit begins at the RF generator, the output of which is immediately directed through a $50\ \Omega$ load, providing proper impedance matching to the output of the generator. Due to the large magnetic moment of the proton and the relatively high magnetic fields attainable with modern superconducting magnets, the Q Meter operates at a frequency of hundreds of MHz; in the case of E155 with a 5 T magnetic field, the operating frequency was 213 MHz.

Parallel to the $50\ \Omega$ load resistor is a second path to ground through R_{cc} . The value of this current-limiting resistor is typically on the order of $1\ \text{k}\Omega$. This keeps the total resistance of the circuit close to $50\ \Omega$ so that the generator's output impedance remains well matched over the entire frequency range of the NMR sweep. The parallel path through R_{cc} itself splits into two paths. One is through the RCL chain which contains the NMR coil; the other is through an output amplifier of known input impedance, R_A .

Since the current in the coil is what gives rise to the polarization signal in the circuit, it is essential for the amount of this current to be frequency independent, in order to avoid the need to make frequency-related corrections before signal integration. This is the *constant current condition*. To meet this condition, the impedance of the RCL branch should be much less than the impedance R_A of the output amplifier.

One way to ensure this is to use a high input impedance amplifier. Practical issues involving signal-to-noise performance of amplifiers on the market, and availability of parts led the designers to choose amplifiers with a $50\ \Omega$ input impedance. Thus the resonant impedance of the RCL chain needs to be much less than $50\ \Omega$. This is easily achieved for most combinations of target material and magnetic field. Typical values

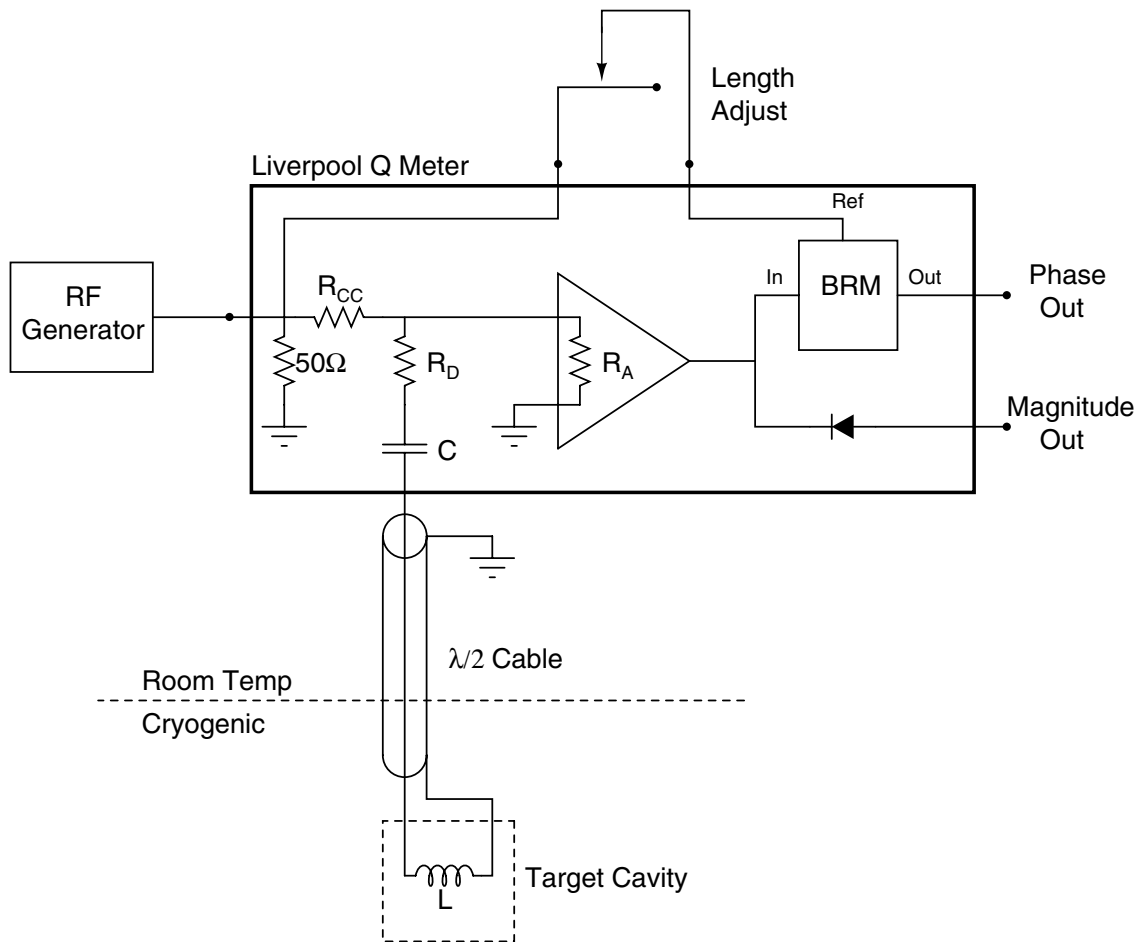


Figure 4.3: Block diagram of the main Q Meter circuit.

of the components in the RCL chain for a proton measurement in a 5 T field are on the order of 10 pF for the tuning capacitor C , 10 Ω for the damping resistor R_D , and under 30 nH for the NMR coil, L_0 . Typically, the overall impedance is around 10 Ω , which is sufficiently smaller than R_A .

One of the driving considerations behind the layout of the NMR system is that the target material exists in a cryogenic and high-radiation environment that is hostile to most electronic components. As a result, only the inductor (the NMR coil) is located within the target, as it must be in order to measure the susceptibility of the material. The connection between this inductor and the rest of the circuit is by means of a semi-rigid coaxial transmission cable. Reflections from the ends of this cable would interfere with the measurement, and would vary with the frequency of the signal passed through the cable. If instead a standing wave is established in the cable, the voltage delivered to the coil has no frequency dependence, and thus ensures the constant current condition is met.

The condition for the creation of a standing wave is the requirement that the length of the cable be an integral number of half-wavelengths of the resonant frequency to be measured. These cables are usually referred to as “lambda-by-two” ($\lambda/2$) cables for this reason. It should be noted that this length condition can only be met for one frequency, whereas the system is made to sweep across a small range of frequencies. This imparts a small asymmetric distortion of the signal which varies with the number of half-wavelengths of cable length, as well as with several other circuit parameters, such as the propagation delay and phase constant of the $\lambda/2$ cable and the inductance of the NMR coil when filled with target material. In addition the low input impedance R_A of the amplifier causes a broadening of the signal. The $\lambda/2$ cable also adds resistance and capacitance to the RCL chain in proportion to its length. In order to keep the total impedance of the chain below 50 Ω , the number of half-wavelengths of

the cable must therefore be kept to a minimum.

The output of the amplifier is split and sent into two devices. The first is a full-wave diode detector, which produces an output, the magnitude of which is useful in finding the proper setting of the tuning capacitor C . The second device to which the amplifier output is sent is a phase-sensitive detector (PSD) known as a Balanced-Ring Modulator (BRM).

The BRM is a device that takes two inputs, a reference and the signal input, and generates an output which is proportional to the magnitude of the input signal multiplied by the phase of the input relative to the reference signal. The input signal used is the suitably conditioned output of the amplifier R_A . The reference signal is a copy of the RF generator's output sent through a short coaxial cable. The length of this cable is adjusted so that there is zero phase difference between the reference signal and the amplifier output at the resonant frequency of the species to be measured. In this way, only the real part of the input signal is output by the BRM, and thus only the absorptive component of the susceptibility is measured. Unlike the magnitude signal from the diode detector, the real-part output from the BRM is largely independent of the signal modulation M [54], since the BRM's output is linear for a wide range of input signal voltages, even those close to zero.

The output of the BRM is close to being a direct representation of the desired quantity, $\chi''(\omega)$. A few processing steps, described in Section 4.3.1, produce a signal which may be directly integrated. This method allows determination of the integral of $\chi''(\omega)$ up to a multiplicative constant. In practice, some of the quantities contained in the exact equation for the polarization are very difficult to measure. The filling factor, η , determining the coupling of the target material to the field created by the NMR coil is one of these quantities. Rather than attempt to measure these quantities and suffer the error inherent in doing so, the overall constant of proportionality is determined

by making a calibration measurement when the material is at a known polarization. The most reliable method is to make this calibration when the spins are in thermal equilibrium with the temperature of the lattice. In this state, the polarization is given by the lattice temperature and the external magnetic field, as in Equation 4.5 to Equation 4.7. With the area of the thermal equilibrium signal measured and the NMR system thus calibrated, the enhanced polarization may then be measured. The larger area of the enhanced signal, combined with the calculated polarization at thermal equilibrium can then be used to calculate the enhanced polarization with

$$\frac{P_{\text{Enh}}}{P_{\text{TE}}} = \frac{A_{\text{Enh}}}{A_{\text{TE}}} \frac{G_{\text{TE}}}{G_{\text{Enh}}} \quad (4.16)$$

where P is the polarization, A the area measured under the signal, and G the amplifier gain used to obtain the signal.

In E155, thermal equilibrium calibrations were often performed at 5 T and 1.6 K. From Equation 4.5, the proton polarization at these conditions is about 0.3%. Typical enhanced proton polarizations may be 95% or more. Thus it should be noted that Equation 4.16 can only be used because the electronics in the Q Meter are capable of linear operation across a dynamic range of over 300:1.

4.2 Target Setup and Equipment

A solid, polarized target was used for E155 as the source of polarized protons and deuterons. The target material was cooled to 1 K, surrounded by a magnetic field of 5 T, and irradiated with about 1 W of 140 GHz microwaves. The following sections detail the equipment required to attain these conditions, the equipment used to measure the resultant target polarization, and the equipment used to monitor other

important quantities pertaining to the target.

4.2.1 Proton Material

For proton use, ammonia – $^{15}\text{NH}_3$ – was the optimum choice. It has been proven as a reliable, radiation-resistant source of highly polarized protons [55], and has been used for years in this capacity. For a 1 K, 5 T system, ammonia has been shown to reach polarizations greater than 90% routinely [56], and to maintain its polarization under beam conditions for an acceptable length of time. In the case of E155, this was typically 10 to 14 hours of production running, which corresponds to a total dose of up to $20 \times 10^{15} e^-$. One effect of the electron beam is to cause radiation damage in the material, which reduces the maximum achievable polarization by an amount roughly proportional to the total beam dose. After this damage has reduced the polarization to an unacceptable value, the material can largely be restored by putting it through an *anneal cycle*. This procedure involves warming the material to a temperature of about 80 K for a period of about 20 minutes.

When using ammonia as a target material, it is not possible to polarize the 3 hydrogens without also polarizing the nitrogen atom. This is an unwanted polarized contamination in the target material, and the asymmetry being measured needs to be corrected for any asymmetry due to scattering off this polarized nitrogen. It is therefore essential to know what the nitrogen polarization is. Normal ammonia is made of ^{14}N , a spin-1 nucleus. The result is both an unpaired proton and neutron that act as a polarized contaminant in the material. Also, due to the electric field gradient within the molecules in the lattice, the ^{14}N signal is split into two NMR peaks, spanning a rather wide energy range (approximately 2 MHz at 5 T). Because of the width of this signal, it is difficult to measure accurately the ^{14}N polarization.

The physics asymmetries measured from a $^{14}\text{NH}_3$ target also require correction due to the polarized proton and neutron polarizations in the ^{14}N .

By using ammonia containing ^{15}N instead of ^{14}N , some of these difficulties are eliminated. There is no polarized neutron in ^{15}N , eliminating the need to correct for this polarized contamination, leaving only a correction for the polarized proton. Further, ^{15}N is a spin- $\frac{1}{2}$ nucleus, and has a single, narrow NMR peak. This makes measuring the ^{15}N polarization much easier than measuring the ^{14}N polarization.

The ammonia chips were prepared by freezing purified gaseous $^{15}\text{NH}_3$ in bulk with liquid nitrogen. The solid block of frozen ammonia was then crushed into small pieces and mechanically sorted with a wire mesh into chips of 1 to 3 mm size. This procedure, the storage of the material, and the process of loading of the material into the target was done in or near the surface of a bath of liquid nitrogen, in order to keep the material below its freezing point and to avoid contact with water vapor, which would cause a layer of ice to form around the granules.

4.2.2 Deuteron Material

In the past, experiments of this type have used deuterated ammonia or deuterated butanol as a polarized deuteron source. For E155, deuterated lithium six hydride ($^6\text{Li}^2\text{H}$), more usually referred to as lithium six deuteride (^6LiD) was used. There were several reasons for choosing lithium deuteride over deuterated ammonia. A brief discussion of each follows.

First, ^6LiD provides an improvement over $^{15}\text{ND}_3$ in the figure of merit of the target. The figure of merit is proportional to the square of the dilution factor times the square of the polarization times the material density. To good approximation [57], ^6Li consists of an alpha particle plus a deuteron. This deuteron, in combination

with the free external deuteron in the ${}^6\text{LiD}$ molecule, makes a polarized nucleon to total nucleon ratio close to $4:8 = 50\%$, as compared with the ratio of deuterated ammonia – $6:21 = 28.6\%$. ${}^{15}\text{ND}_3$ can be polarized up to around 40% [56, 58, 59], while ${}^6\text{LiD}$ reaches typically 25% [60] at the same temperature and magnetic field. The somewhat higher polarization of ${}^{15}\text{ND}_3$ does not make up for its much lower dilution factor: the overall figure of merit for ${}^6\text{LiD}$ is about a factor of two greater than that of ${}^{15}\text{ND}_3$.

A second advantage of using ${}^6\text{LiD}$ is that the measurement of the deuteron polarization is easier than in ${}^{15}\text{ND}_3$. In ${}^{15}\text{ND}_3$ the NMR signal of the deuteron is split into two peaks because of interaction between the deuteron quadrupole moment and the electric field that exists within the ${}^{15}\text{ND}_3$ molecule. In ${}^6\text{LiD}$, this electric field is absent and therefore the splitting does not occur. The result is a single NMR peak that is much higher and more narrow, which causes a better signal-to-noise ratio in the measurement.

A third advantage ${}^6\text{LiD}$ has over ${}^{15}\text{ND}_3$ is in its radiation resistance. ${}^{15}\text{ND}_3$ required frequent annealing, about every 12 hours, to repair radiation damage. Along with this was the need to recalibrate the NMR system with thermal equilibrium measurements, which imposed additional down time, due to the need to verify that target settling had not occurred. ${}^6\text{LiD}$ exhibits much better radiation resistance, typically taking about 5 times the beam dose, before its polarization drops unacceptably low. As a result, a target sample can be loaded and used for many days without interruption. A disadvantage to ${}^6\text{LiD}$ is that once the material becomes substantially damaged, annealing did not seem to recover the polarization performance to that of new material, despite one successful anneal.

In addition to the three main benefits already discussed, ${}^6\text{LiD}$ was also much easier to handle. It is a rock-like solid, similar in composition to sandstone, light enough

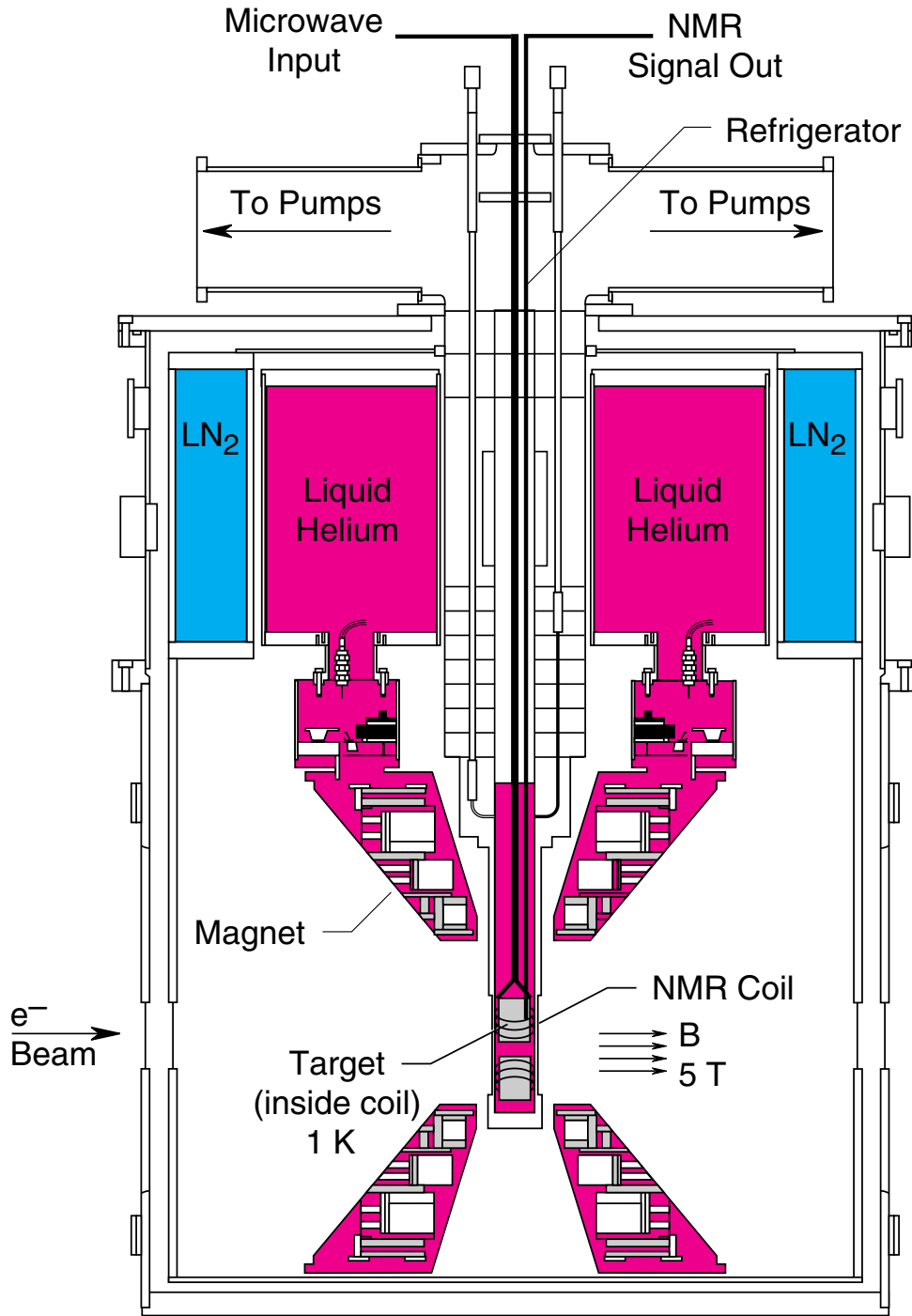
that small chips of it float in liquid nitrogen. This made working with the material and loading it into the target much easier. This robustness also accounted for the fact that no physical destruction of the chips was observed after use in-beam. Ammonia chips have been observed to break down into smaller pieces, and sometimes into a powder-like substance under similar beam and annealing conditions. The resulting settling of the material changes the coupling of the material to the NMR coil, which then requires a new calibration of the NMR by thermal equilibrium measurement.

The ${}^6\text{LiD}$ was acquired as a cylindrical chunk of sintered material from Lawrence Livermore National Labs. It was placed in a dry nitrogen atmosphere in a glove box or bag and smashed with a hammer, and then sorted with a wire mesh into chips of approximately 1 to 3 mm size. It was then irradiated at the SunSHINE facility at Stanford University, a 30 MeV linear electron accelerator. Typical conditions of this pre-irradiation were a temperature of 180 K and a total dose of $3.0 \times 10^{12} e^-/\text{cm}^2$. To maintain the proper temperature in the ${}^6\text{LiD}$, a controlled stream of chilled helium gas was passed through the material during the irradiation. A full discussion of the preparation and performance of ${}^6\text{LiD}$ in E155 can be found in [60].

4.2.3 Cryostat, Refrigerator, and Magnet

The magnetic and cryogenic requirements of the target are met by an insulated cryostat containing a ${}^4\text{He}$ evaporation refrigerator and a split Helmholtz-pair superconducting magnet. Figure 4.4 shows a schematic of the cryostat used.

The refrigerator sits in the innermost layer of the system, drawing liquid helium from the 85 l reservoir above the magnet coils. Outside this reservoir is a 57 l liquid nitrogen reservoir that acts as a heat shield, absorbing the 300 K blackbody radiation from the room-temperature outer walls of the cryostat. The volume surrounding the



4-94

7656A1

Figure 4.4: The E155 Polarized Target Cryostat and Refrigerator.

cryogen reservoirs is maintained at a high vacuum of a few 10^{-7} torr when cold, to eliminate convective heating of the cryogen reservoirs.

To maintain proper liquid levels, the magnet reservoir was automatically filled from a 500 l liquid helium dewar, which in turn was automatically filled from a 2000 l dewar. Approximately every 2 weeks the 2000 l dewar would be craned out of the End Station for refilling. In a similar way, the liquid nitrogen level was maintained automatically by a 2000 l dewar mounted on a cart. Approximately every 2 weeks this dewar would need refilling.

The magnet was built by Oxford Instruments and consisted of two sets of coils, approximately 50 cm in outer diameter and approximately 8 cm apart at the core, forming a Helmholtz pair. The thickness of the coils and the location of the supporting structures between them were such that beam could pass through in two directions: along the shared axis of the coils (parallel to the magnetic field) or between the coils (perpendicular to the magnetic field). For A_{\parallel} or A_{\perp} measurements, the entire cryostat was rotated such that the magnetic field was along the beam direction or perpendicular to it, respectively. The shape of the coils, and of all downstream beam windows and flanges, was such that no part of the magnet entered the acceptance of the spectrometers[‡]

A 10 V, 120 A power supply was used to drive the magnet, with a current of about 77.8 A producing the 5 T field at which the experiment was conducted. The magnet was also equipped with two trim coils, and with them also energized a 28 mm spherical region was created in which the field was uniform to 1.1×10^{-4} . This uniform field region could be maintained indefinitely by putting the magnet into *persistent mode*. This involved the closing of a superconducting switch in the magnet, allowing the

[‡]A small portion of the acceptance of the 10.5° spectrometer actually did include a thicker part of an outer beam window of the target can. This small part of the total acceptance was at the large angle side of the spectrometer and received very few counts.

power supply to be ramped down to zero current, while the magnet remained at full field. A field stability of better than 1×10^{-6} per hour was possible in this mode.

4.2.4 Target Insert

The target material was held in place in the cryostat by an apparatus known as the target insert. This device combined the target cavities, NMR coils, microwave distribution system, and temperature sensors into a 2 m long by 5 cm wide cylindrical package that could be easily removed and replaced to facilitate changes of target material or replacement of broken sensors.

The bottom of the insert contained the target cavities, arranged in a vertical stack, as depicted in Figure 4.5. The insert was mounted in the cryostat by means of a mechanical piston, which allowed the entire insert to be moved vertically so as to place any of the targets into the beam path. There were two 2.5 cm diameter cavities designed to hold polarizable material. This allowed greater periods of data taking before radiation damage in the material necessitated target annealing. It also afforded flexibility in run planning since both deuteron and proton material could be placed in the same insert, and the targets alternated to suit the needs of the experiment. These two target positions were referred to simply as the **upper** and **lower** targets.

Between the two polarized target cavities were two smaller target positions. One contained a small (1.2 cm diameter) unpolarized target of either carbon or beryllium, known as the **disk** target. At the other position, the insert had a 0.8 cm hole. This position allowed the scattering contribution from windows in the cryostat to be measured.

Below the **lower** target was another cavity, identical to the ones designed to contain the polarized material. This cavity was loaded with a disk of unpolarizable

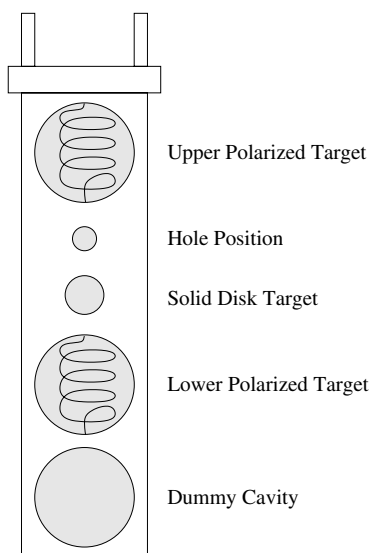


Figure 4.5: Layout of the target cavities in the E155 target insert.

material designed to match the radiation length of the polarized material. Pyrolytic carbon was used as the match for $^{15}\text{NH}_3$, and pure beryllium as the match for ^6LiD [61]. This target, known as the dummy target, was useful in determining the target packing fraction (see Section 5.4) and in monitoring for acceptance changes over the course of the experiment.

4.2.5 NMR System

Polarization measurements of the target material were made by a continuous NMR system. The system utilized the Liverpool Q Meter [54], an RF device that measures the absorptive portion of the magnetic susceptibility of the target material by examining the phase error between an applied RF signal and the response to that signal of an inductive coil embedded in the target material. A full description of the operation of the Q Meter was given in Section 4.1.3.

The RF input came from a Rohde & Schwarz SMT02 generator, being frequency

Species	Larmor Frequency (MHz)	$n\lambda/2$	Total length (cm)
^1H	213.05	7	365.78
^2H (D)	32.70	1	339.16
^6Li	31.36	1	354.45
^7Li	82.81	3	405.22
^{15}N	21.60	1	523.03

Table 4.1: Lengths of $\lambda/2$ cable used in the NMR system. All frequencies are for a magnetic field of 5.004 T.

modulated at 1 kHz by an external triangle wave. This signal was sent to the Q Meter, which then sent it through a transmission line with a length equal to an integral number of half-wavelengths of the RF. This is the $\lambda/2$ cable discussed in Section 4.1.3. Table 4.1 lists the length of cable used for each of the polarization measurements made. Each $\lambda/2$ cable consisted of two sections: a room temperature part and a cryogenic part. The cable used in the cryogenic environment was 152.4 cm in length, extended from the NMR coil to the top plate of the target insert, and had a solid dielectric made of teflon. The room temperature cable connected to a vacuum feedthrough on the top plate of the insert and terminated at the input to the Q Meter. This part of the $\lambda/2$ cable contained a teflon dielectric that is closer in consistency to a foam than a solid plastic. This different dielectric is necessary because the dielectric constant of the solid teflon material used in the cryogenic region undergoes a transition in the 18 to 20 C range, making it unsuitable for use in changing room temperature environments. Such a transition causes significant deviations in the tune of the Q Meter, and thus affects the accuracy of the polarization measurement.

Since the frequencies needed to measure all spin species in the target varied across a large range, two NMR coils of different length were used – one for the lower frequencies used to measure ^{15}N , ^6Li and ^2H consisted of 4 turns, approximately 24 cm

in length; the other for the higher frequencies used to measure ${}^7\text{Li}$ and ${}^1\text{H}$ consisted of a single turn, approximately 7.5 cm in length.

In addition to the two shapes of NMR coil, two alternatives for coil material existed. One consisted of 70% copper, 30% nickel tubing with an outer diameter of 0.5 mm and a wall thickness of 0.178 mm. The other consisted of solid aluminum wire with an outer diameter of 0.5 mm, plated with a trace amount of nickel, and then a 5 μm layer of copper. The nickel was necessary for the copper plating to adhere to the aluminum, and the copper plating was necessary to facilitate soldering the wire into the target insert.

One end of each coil was soldered to the end of the $\lambda/2$ cable, the other soldered directly to the wall of the target cavity, a 2.5 cm diameter by 3 cm cylinder made of aluminum and copper plated in the manner described above.

The Q Meter measured the polarization by detecting changes in phase of the signal in the NMR coil, as discussed in Section 4.1.3. The signal usually consisted of a DC component of several volts plus a frequency-dependent 5 mV to 1 V component due to the susceptibility. This signal was first sent through an offset card capable of subtracting off up to 3 V of DC. The output of the offset subtraction then went through two stages of differential amplification, and finally into a unit called a STAC [62] – a set of two CAMAC modules, one containing an embedded 68000 microprocessor, the other a 4-channel multiplexer, a sample-and-hold circuit, and a 16-bit ADC.

The STAC controlled the entire sequence of the NMR sweeping in a multi-step, double-sweep process. First it generated a DC value to be used as the FM input to the frequency generator. Then it paused for a programmable length of time to let the generator and other electronics stabilize. Next it sampled the amplified Q Meter signal with a 16-bit ADC. The ADC value was then stored in a memory location corresponding to the frequency. These four steps were then repeated for the next fre-

quency step. After all 400 frequency steps, from lowest to highest, had been sampled, the STAC would repeat the process on all 400 steps, this time going from highest to lowest frequency. In usual running the STAC would perform 200 double-sweeps, keeping a running total of all ADC values for each of the 400 frequency steps. During thermal equilibrium measurements, 1000 to 5000 double-sweeps were acquired for each measurement, due to the much smaller signal size, and therefore worse signal-to-noise ratio.

When the STAC finished performing the prescribed number of double-sweeps, it returned the 400-point waveform to the NMR data acquisition computer. This computer then performed the necessary signal processing to go from the waveform to a polarization value.

4.2.6 Temperature Measurement

Accurate knowledge of the temperature of the target material was essential for proper calibration of the NMR during thermal equilibrium measurements. During enhanced polarization running, target temperature was helpful in understanding small fluctuations in the polarization, among other things. During annealing of the target material, accurate measure of the target temperature was again necessary to control the length of time the material was at the anneal temperature, and to help guarantee that the paramagnetic centers in the material would not be destroyed by inadvertent overheating. For all of these reasons, several methods were used to monitor the target temperature, each having greatest utility in a specific temperature regime.

The primary device used to measure temperatures in the 1 K to 5 K range was a ^3He manometer. This consisted of a long closed tube containing a small amount of ^3He , with one end placed in the vicinity of the target material, extending through

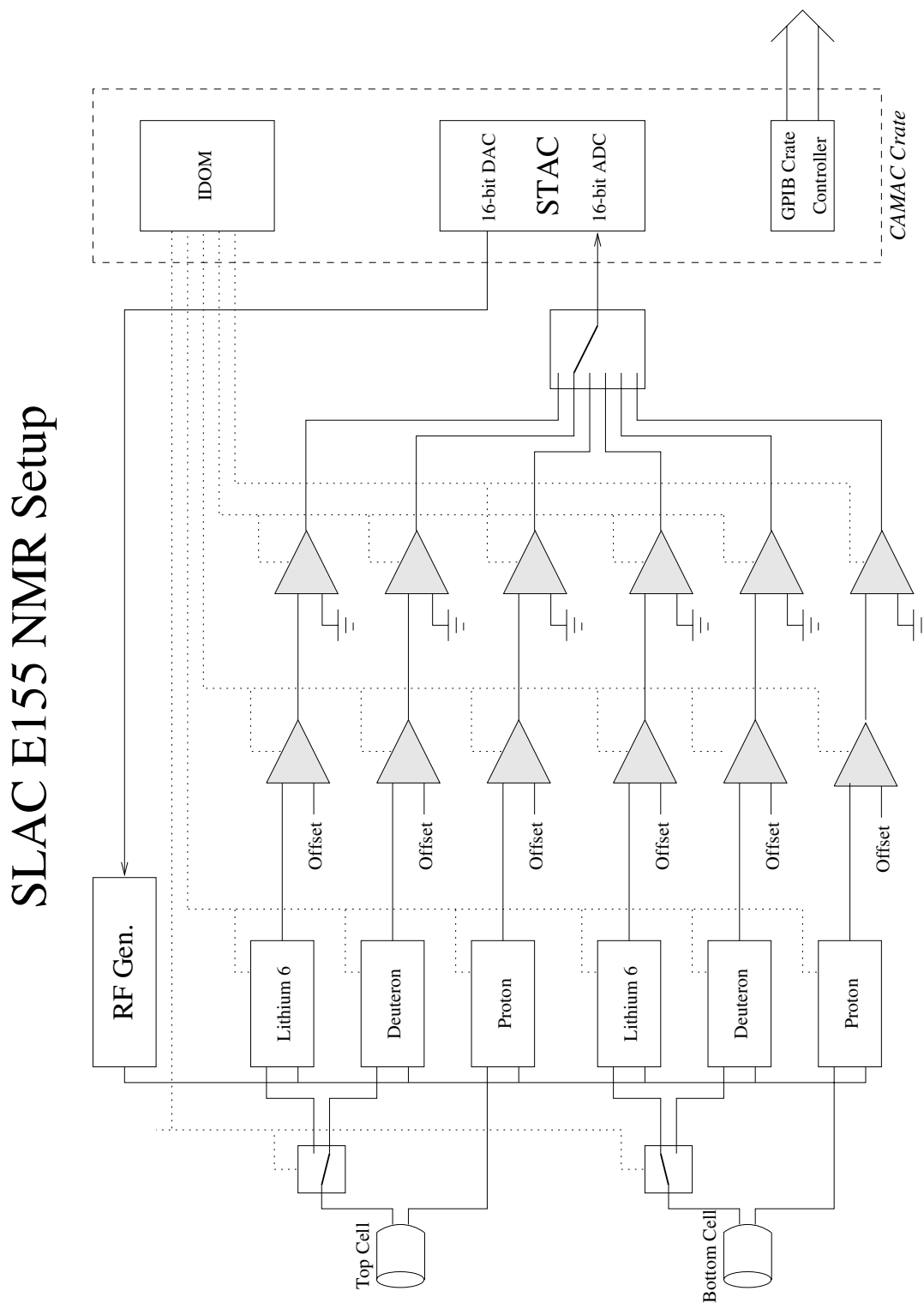


Figure 4.6: Components of the E155 NMR System.

a penetration in the system up to room-temperature, terminating in a sensing head. The readout unit of this device returned to the data acquisition computer a value representing the pressure, in torr, inside the tube. This was then converted to temperature using the ITC-90 [63] temperature standard for ^3He .

As a backup to the ^3He manometer, a ^4He manometer was also used. It consisted of an open tube placed in the vicinity of the target, but with the end high enough so that it was not immersed in liquid helium during normal operation. This tube then also extended up through a penetration in the system to room temperature, at which point it fed into a measuring head. Again, the readout unit reported the pressure in torr, and again the ITC-90 temperature standard was used to determine absolute temperature.

After the end of E155 production running, a comparison test was made between the two manometers, and they were found to be in excellent agreement up to 1.65 K. It is believed that the discrepancy between the two above 1.65 K was due to a small contamination of ^4He present in the sealed ^3He tube, such that above the boiling point of ^4He , the vapor pressure of the ^4He began to dominate over that of the ^3He . Due to this discrepancy, the manometers were not used for measurements above 1.65 K. Another possibility is that the pressure sensing head on the manometer was malfunctioning.

For monitoring temperatures during a target anneal, two 100 Ω platinum resistors were used, one in each of the polarized target cavities. These were monitored by an Oxford Instruments ITC-4 temperature controller, which also controlled the current delivered to a 40 or 60 Ω heater wire wrapped around the target insert. In addition to the platinum resistors, each target cavity had a 1 k Ω RuO₂ chip resistor, which was monitored by balanced resistance bridge. Some setups of the target also included a gold/iron-chromel thermocouple, which was monitored on a high-precision voltmeter.

Additional temperature measurement devices were located on the target insert to aid for monitoring and diagnostic purposes. These devices included 100 Ω and 270 Ω Allen-Bradley resistors, carbon-glass RTDs, and RuO₂ resistors.

4.2.7 Microwave System

Microwaves for enhancing the polarization of the target material were generated by an Extended Interaction Oscillator (EIO) tube manufactured by Varian, Canada. The tube used produced up to 20 W of microwave power at a frequency of around 140.1 GHz. Once exiting the tube, the microwaves were carried by air-filled waveguide to the entrance to the target, and by helium-filled waveguide once inside the target cryostat.

Immediately downstream of the tube, a coupler split off a small portion of the microwaves, which were sent to an EIP Frequency Counter, and a power measuring device. The rest of the microwaves were then brought through a switch, capable of routing them to the top target cavity, the bottom target cavity, or a dump. If the microwaves were directed to either of the two target cavities, they then passed through a number of waveguide transitions, and then entered the target insert through oversized, circular waveguide for better power transmission. Since this circular waveguide was located inside the ⁴He refrigerator, while the rest of the waveguide pieces and other components were outside the cryostat and at room temperature, an isolating window made of FEP (a Teflon film) was placed between the circular waveguide and the transition pieces immediately upstream of it.

The end of this circular waveguide connected to a specially made horn, which broadcasted the incident power evenly over the volume of the target cavity. The target cavities were made of conducting material – aluminum plated with copper –

in order to help contain the microwaves to the cavity alone, thus making the best use of the available power. This had unexpected consequences, however. See Section 4.4 for a complete discussion.

From the change in the boiloff rate of liquid helium when the microwaves were turned on, it is estimated that approximately 1 W of power actually made it into the target cavity.

It has long been known, though generally forgotten, that if the frequency of the microwaves is modulated slightly, an increase in polarization is possible. This effect was recently rediscovered [64]. To produce this frequency modulation, a function generator was used to make a 1 kHz triangle wave with an amplitude of approximately 2 V peak-to-peak. This signal was then applied to a special input on the microwave power supply, which then amplified it and used it as a bias on the cathode voltage applied to the tube. As a result a frequency deviation on the order of 10^{-4} was realized. The exact value was adjusted by the target operator to obtain the most favorable polarization performance.

4.3 Analysis of Target Data

Post-experimental analysis of the target data entails three main processes, to be discussed in the following sections. Section 4.3.1 discusses conversion of an acquired NMR signal into an area proportional to the target polarization. Section 4.3.2 describes how the NMR system is calibrated by measuring the area of the NMR signal when the target is at a known polarization at thermal equilibrium. Finally, Section 4.3.3 presents the method used to calculate the polarization of the other spin species present in the target material.

4.3.1 NMR Signal Analysis

Of the three quarters of a gigabyte of target data taken during the beam time of E155 and during the target technical run that followed beam shutoff, the vast majority represents the 225,000 NMR waveforms captured by the STAC, as described in Section 4.2.5. The remainder of the data comprised associated measurements such as temperatures, magnetic fields, gain settings, and frequencies.

The mechanics of turning an NMR measurement into a raw polarization measurement are relatively simple, and are detailed below. Figure 4.7 gives a pictorial representation of the steps. The signal used in Figure 4.7 is from a poorly tuned Q Meter in order to more clearly depict the effects of the procedure – normally there would be much less slope in the raw signal.

Step 1: Before a series of polarization measurements are to be made, a *baseline measurement* is taken. This baseline is an NMR waveform taken with the magnetic field of the target shifted so that the Larmor frequency of the target material is outside the sweep width of the NMR. In other words, there is no “bump” in the waveform due to the presence of polarized target material. When baseline measurements are complete, the magnetic field is restored to the value that centers the Larmor frequency of the material in the NMR sweep.

Step 2: Each NMR signal that represents a polarization measurement has the baseline signal subtracted from it. Ideally this should remove all of the parabola-like shape that is characteristic of a signal generated by the Q Meters. The result is called the Subtracted Signal.

In reality, temperature drifts in the Q Meters and $\lambda/2$ cable cause slight drifts in component values, which change the shape of the Q Curve slightly. The result is that there is some residual structure remaining after the subtraction. Step 3 is then to fit

the “wings” of the signal – the regions to either side of the peak due to the target polarization – to a polynomial. This polynomial is then subtracted from the entire signal, resulting in what is known as the Polysubtracted Signal.

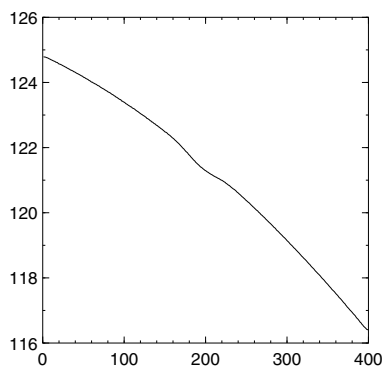
At this stage, all features of the signal due to the electronics of the NMR system should be removed, in principle yielding a waveform due only to the interaction of the NMR field with the polarized material. Step 4 is to calculate the area under this waveform. A numerical integration is performed from a starting point on the low frequency side of the signal to an ending point on the high side.

The regions of the polynomial fit in step three and of the integration area in step four are symmetric about the center of the waveform and are chosen to avoid the first and last several points in the waveform because they typically show much more noise than the rest of the signal. The percentage of the total waveform eliminated for this reason is less than 8%.

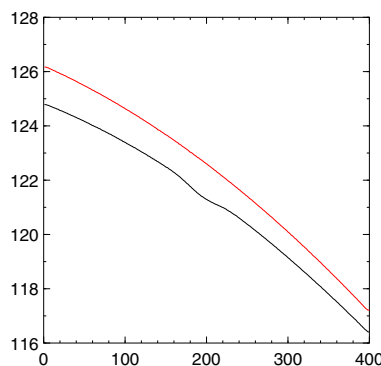
In E155, several tests were done on each NMR waveform before the above steps were performed to obtain a polarization measurement. These included tests on the frequency and sweep parameters, the target position and magnetic field value, the presence of the specified baseline, proper convergence of the polynomial fit, and a check for signal clipping that can result when large amplifier gains produce ADC saturation. Clipping was found in less than 2 percent of the total data set, a number which attests to the attentiveness of the target operators.

4.3.2 Thermal Equilibrium Calibration

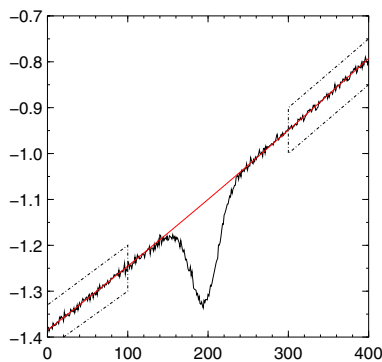
The procedure outlined in Section 4.3.1 above results in a determination of the area of the acquired NMR signal. As discussed in Section 4.1.2, this area is directly proportional to the polarization of the target. Thermal Equilibrium Calibrations –



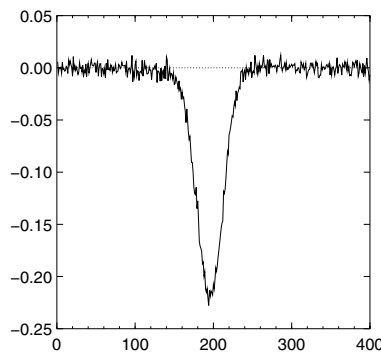
Signal is acquired by the NMR DAQ system



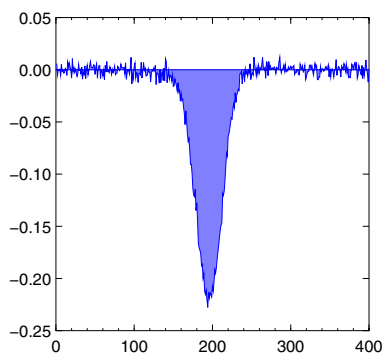
Baseline is subtracted from the signal



Polynomial is fit to wings of the signal



Polynomial is subtracted from the signal



Signal is integrated, giving area

$$\text{Area} \times \text{CC} = \text{Polarization}$$

Calibrating the NMR system gives polarization

Figure 4.7: Steps of the E155 NMR signal analysis.

TE measurements – allow determination of the constant of proportionality.

In order for a proper measurement of a TE to be made, several things must be done. First, the NMR must be tuned so that its resonant peak is at the Larmor frequency of the species to be measured. This minimizes non-linear effects from amplifiers in the Q Meters and from the $\lambda/2$ cables. After the TE measurement is made, any further major tuning of the system alters the calibration constant, necessitating a new TE calibration or a new baseline measurement. Second, the cryogenic levels in the target must be brought to steady states so that the temperature can remain constant for several hours. This involves trimming the position of some of the needle valves that control liquid helium delivery to and gaseous helium removal from the target cryostat. Finally, the measured area of the NMR signals must be examined to determine when the material's spin-temperature comes to equilibrium with its lattice temperature. This is the condition that must be met in order for the TE measurement to be used as a calibration between signal area and polarization.

Typically, the target operator monitors the area of the NMR signals as they are returned from the STAC, plotting them on an area vs. time graph. These points trace out a typical exponential shape as the material thermalizes. The rule of thumb is that the operator should wait at least three time constants of this exponential before considering if the material is thermalized. Figure 4.8 depicts one such thermalization.

Several factors dominate in the determination of the TE calibration constant, and they may vary over time with the result that the calibration constant changes. Perhaps the most significant factor affecting the constant is the filling factor – the coupling between the target material beads and the NMR coil. Over time, motion of the target insert, vibration of the cryostat from pump systems, turbulence in the liquid helium from anneals, and even material destruction caused by beam can all impact the filling factor, with the result that the calibration constant changes.

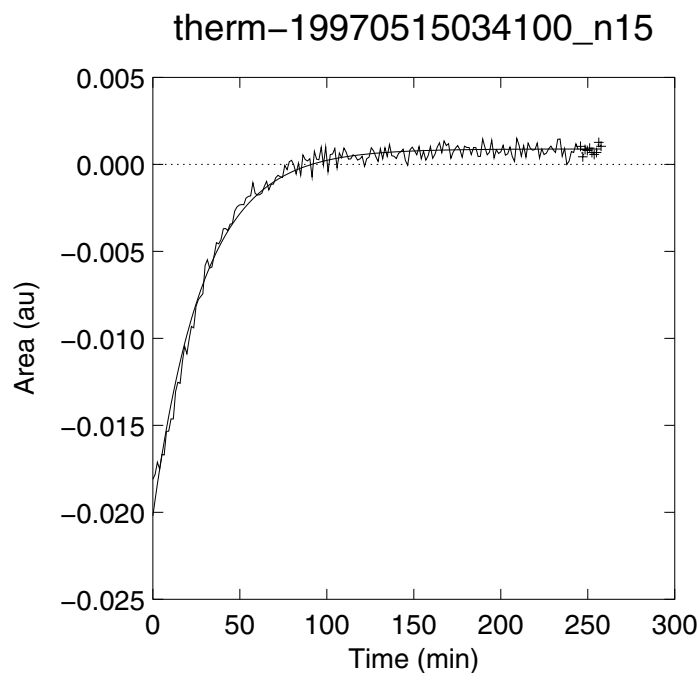


Figure 4.8: NMR signal area as the target material comes to thermal equilibrium. The last ten measurements, marked with plus signs, were used in calculating the calibration constant.

Unfortunately, these changes cannot be measured between TE calibrations, therefore we made many TE calibration measurements at regular intervals over the course of the experiment. Figure 4.9 shows the value of several calibration constants as a function of measurement number.

4.3.3 Measurement of Other Spin Species

Knowledge of the polarizations of all of the spin species in the target material is crucial to making proper corrections to the measured asymmetries. In the case of ${}^6\text{LiD}$, it is important because the deuterons involved in the scattering came from two sources: the atomic deuterons bound to the ${}^6\text{Li}$ nucleus, and the effective deuterons contained within the ${}^6\text{Li}$ nucleus itself. With ${}^{15}\text{NH}_3$, the ${}^{15}\text{N}$ becomes polarized – with

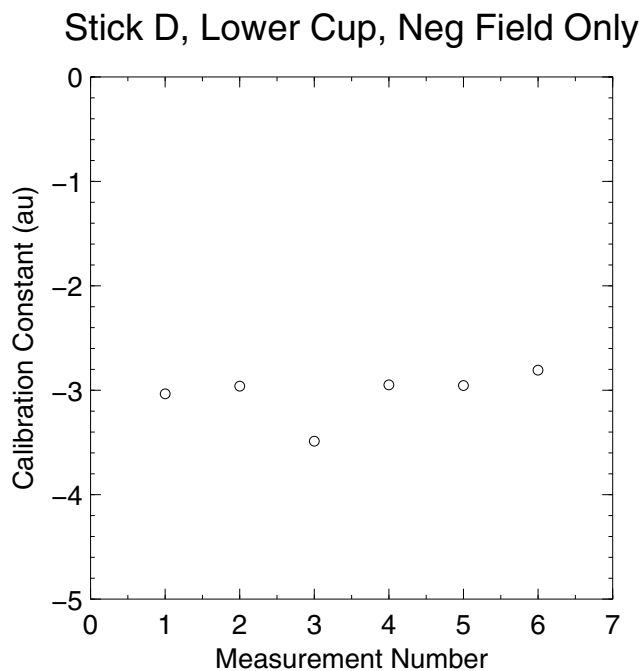


Figure 4.9: TE calibration constants from an E155 target insert.

a sign opposite that of the proton polarization – and so a correction to the scattering asymmetry must be made, thus requiring knowledge of the ^{15}N polarization.

Simultaneous measurement of two different spin species in the same target sample was not technically practical. Having two NMR coils energized at the same time would cause cross coupling between them that would distort both of the measurements. An alternative is to interleave measurements of the two polarizations. During experimental conditions, the microwave power delivered resulted in a buildup rate of the proton polarization fast enough that this was also not practical.

For E155, empirical formula, derived from proton vs. ^{15}N polarization studies [65], was used to supply the ^{15}N polarization from the measured proton polarization

$$P_{15} = -(0.136P_p - 0.183P_p^2 + 0.335P_p^3). \quad (4.17)$$

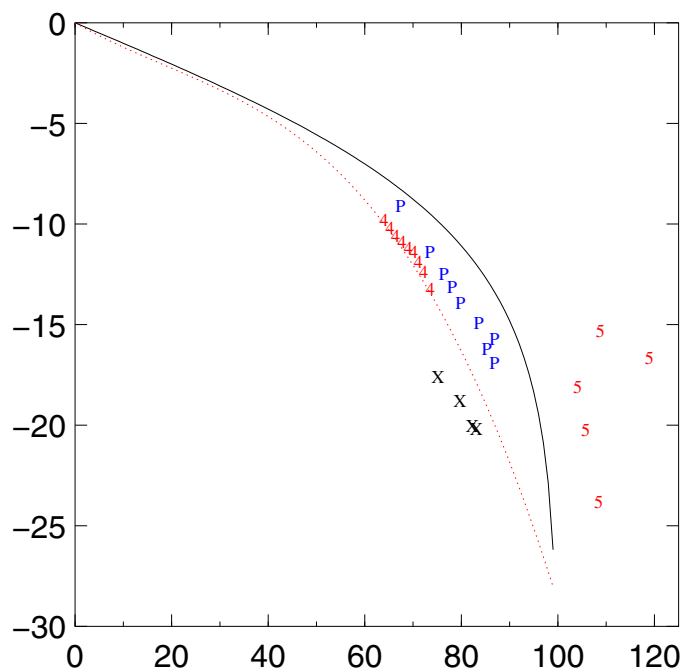


Figure 4.10: ^{15}N versus proton polarizations. Solid line is EST, dotted line is Equation 4.17. Symbols are: P - PSI; X - E155x; 4 - E143; 5 - E155.

The minus sign in front of the above expression is present because the magnetic moment of ^{15}N is opposite that of the proton, and thus the polarization is also opposite in sign. Figure 4.10 shows a plot of Equation 4.17 with data from several experiments. This figure shows that the ^{15}N polarization was found to differ substantially from that predicted by the Equal Spin Temperature (EST). EST is a theory that relates the polarizations of two species in a material through their total spin and their magnetic moments.

4.4 Correction of Proton NMR Signals

While running on $^{15}\text{NH}_3$ during E155, some features of the NMR signal and of the measured polarization began to suggest a problem in the NMR system. The main

symptoms of the problem were:

1. Great difficulty was sometimes experienced in tuning the NMR system prior to taking measurements. (Tuning involves adjusting the capacitance and the length of the phase cable in order to obtain a resonance centered on the Larmor frequency of the species to be measured.)
2. The Q Curve and NMR signals were inverted, ie, a positive polarization enhancement produced an NMR signal with a peak pointing down instead of up. (An example can be seen in Figure 4.7. The signal depicted, which has a downward-pointing peak, is of a positively polarized material.)
3. There was residual signal present in the wings of the NMR signal, whereas normally the signal tends quickly to zero in the wings. Further, this residue was not symmetric about the frequency axis, whereas proper NMR signals of the proton in NH_3 are largely symmetric with the exception of some well-understood features. (See Figure 4.11 for an example.)
4. Polarizations above 100% were observed, despite careful re-analysis of the TE Calibration Constants and of the signal areas.
5. There was a larger than expected discrepancy between the highest positive polarizations (up to +120%) and the highest negative polarizations (up to -90%).
6. The spin asymmetry obtained from runs with high polarization differed beyond statistics from that obtained from runs with lower polarization.

One of the greatest differences between the target system used in E155 and that used in previous experiments, such as E143, was that E155 had a completely re-designed target insert, primarily to enhance microwave delivery to the target material.

It is now understood that these changes had unforeseen effects on the performance of the NMR system when it was used to measure proton polarization. Consequently, the NMR system was operated outside its design envelope, resulting in a significant degree of non-linear behavior. No problems with the Liverpool Q Meter have been discovered, and thus targets using this device in other experiments are not similarly affected.

The new features of the E155 insert, as compared to that used in E143, follow. First, the target cavities were made of aluminum instead of torlon, as in previous experiments. In the past, polarization performance suffered due to a lack of microwave power on the target. Since increasing the delivered power is beyond current microwave tube technology, metal cavities were chosen to help confine the microwaves to just the target region, instead of letting them fill the entire volume of the tailpiece and refrigerator. An additional benefit of the metal cavities was that they conducted heat much more evenly during target anneals, thus avoiding hot spots that may cause material to melt or settle. In order to make reliable solder attachments to these cavities, a thin copper plating was deposited on their surface.

Second, the material used in the NMR coil was aluminum wire, instead of the Cu/Ni tubing that had been used in the past. The smaller total Z of the aluminum coils results in less unpolarized material placed in the beam. As with the aluminum cavities themselves, in order to aid soldering to the wire, a thin plating of copper was deposited on the surface.

Other changes to the insert were less likely to have affected the NMR, but included adding a second microwave horn so that each cavity had its own supply of microwave power, adding stiffening rails to make the insert more rigid and less easily damaged in handling, and changing some of the temperature-sensing resistors.

During E155 running, it was observed that if the NMR coil material was changed back to that previously used, Cu/Ni tubing, the problem with the NMR signal shape was almost eliminated, but not the signal and Q Curve inversion. However, there was a significant difference in the size of the signals obtained – about a factor of five – which should not occur.

The remainder of this section will discuss the correction of the NMR problems mentioned above. First, a brief discussion of two failed attempts at corrections will be provided in order to illuminate aspects of the NMR problem that were learned from them. Full accounts of the two methods are given as appendices. Next, a detailed description of the cause of the problem is provided. Finally, the correction to the data used in this analysis is described.

4.4.1 Attempts to Correct the NMR Data

A measurement made at the end of the technical run that followed E155 suggested that some of the unwanted features in the proton signal disappear if the NMR frequency is decreased. Since the frequency at which the NMR samples the material is determined by the proton Larmor frequency, this test measurement required operating the magnet at half the field used during E155. The two signals are shown in Figure 4.11. The 213 MHz signal (solid line) can be seen to descend below zero to the left of the peak, and to have a slope different than zero at its edges. Further, to the right of the peak the 106.5 MHz signal is sharply curved, while its curvature is much more shallow to the left of the peak. The 213 MHz signal is the opposite of this, with the shallow side on the right and the sharp side on the left, as if it had been flipped about the line $y = 200$.

With the discovery that some of the proton signal problems disappear at lower

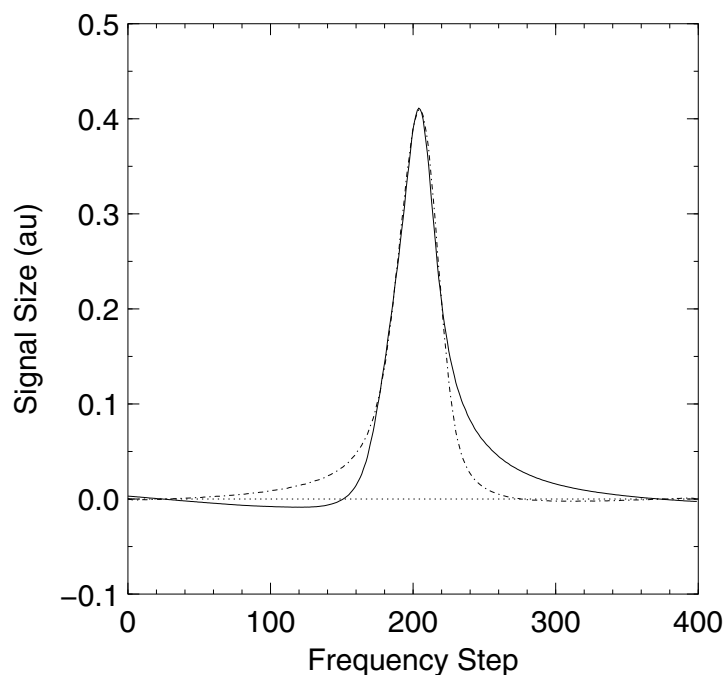


Figure 4.11: Comparison of NMR signals of $^{15}\text{NH}_3$ at 2.5 T/106.5 MHz (dashed line) and 5 T/213 MHz (solid line). The 213 MHz signal, representing a polarization of about 94%, was flipped about the x -axis and then scaled by a factor of 280 in order to aid comparison with the 106.5 MHz signal, which represents a polarization of only 23%.

frequencies, the ^{15}N signals, which are acquired at 21.6 MHz in a 5 T field, were then inspected and also found to appear normal. This suggested that only the 213 MHz proton polarization measurements were distorted by the NMR, and not the ^{15}N measurements.

A correction method based on this fact was then developed. Briefly, some measured values of ^{15}N and proton polarizations were plotted against each other and fitted. This relation was then compared to that discussed in Section 4.3.3, Equation 4.17, reproduced here

$$P_{15} = -(0.136P_p - 0.183P_p^2 + 0.335P_p^3). \quad (4.18)$$

This correction method had two drawbacks. First, the need for simultaneous measurements of proton and ^{15}N polarizations at every point of a polarization buildup was not envisioned during the technical run. As a result, the data sets consist of measurements of proton polarizations from zero to a maximum value, and then a handful of measurements on ^{15}N . The lack of ^{15}N data at lower polarizations required extrapolations to be made, with introduced greater uncertainties to the method. The second drawback to the method is that the signal residue present in the NMR waveform, mentioned in the previous section, complicated the determination of the signal area. The method is discussed fully and the resulting correction shown in Appendix A.

The observation that signal residue interfered with the polynomial fit used in determining the polarization led to another means of correcting the data. The residue has an appearance similar to the dispersive component of the material's magnetic susceptibility. This suggested that if this residue could be removed, the remaining purely absorptive signal could be used to obtain good measurements of the polarization.

To accomplish this, a model was developed to simulate the shape of the NMR signal. The model, which contains seven parameters, consists of components representing absorptive and dispersive NMR signals, and a polynomial to account for drifts in the Q Meter baseline. The approach is to fit the model to each of the approximately 100,000 proton NMR signals. After each fit, the part of the model representing the absorptive signal is extracted and integrated. The resulting area produces a polarization measurement when combined with a calibration constant. An example of a fit of the model to a real signal is shown in Figure 4.12.

The drawback to this approach is that there are many parameters in the model, and almost any signal shape can be fitted. Ideally, the model would be based on a simulation of the actual Q Meter circuit. This is not practical because it would require inputs representing circuit parameters that are difficult or impossible to measure. The

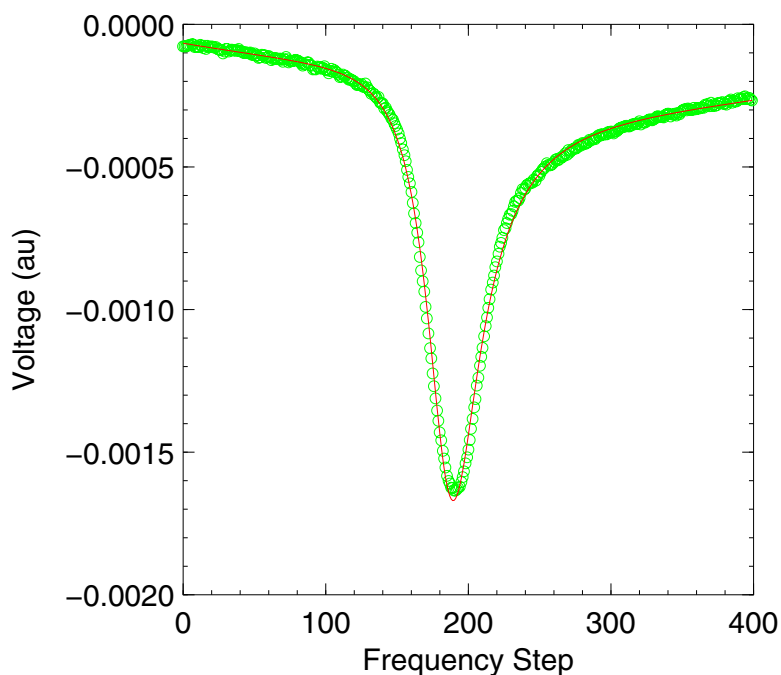


Figure 4.12: Fit of a modeled lineshape to a real proton NMR signal.

correction generated from this method resulted in an increase of the polarization even further above 100%.

Full explanations of these two correction methods, and plots of the correction curves they produce, are included in Appendix A and Appendix B.

4.4.2 Failure of the Constant Current Condition

Extensive analysis [66, 67] and discussion [68–70] of the E155 NMR system and of the signals it produced have led to a consensus opinion on the cause of the anomalous effects observed.

The conclusion is that the construction of the E155 target insert, most importantly the metal target cavity walls, were the cause of the NMR problems. There is no evidence that the Q Meters misperformed in any way, nor that the measurements of

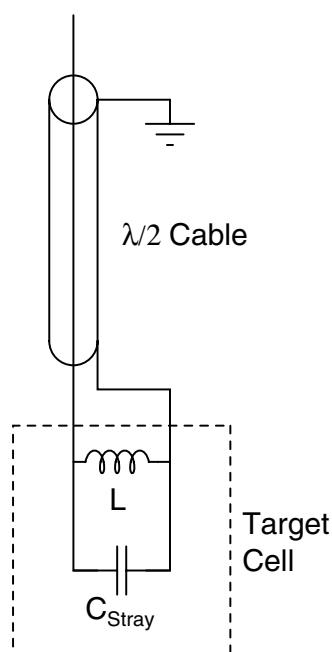


Figure 4.13: Resonant circuit with the addition of stray capacitance.

any other experiment, including E155's own measurements of ${}^6\text{LiD}$, are in any way suspect.

Evidence supports the assertion that a capacitance was created in parallel to the NMR coil within the target cell. The source of the capacitance is coupling between the NMR coil itself and the metal walls from which the cell was constructed. Since ${}^{15}\text{NH}_3$ has a high dielectric constant, this capacitance is increased by the presence of the target material itself. A depiction of the modified circuit is presented in Figure 4.13.

Simulations of the Q Meter circuit were used to test the effects of such a capacitance on the signal produced. It was found [67] that if the total impedance of the NMR coil and parallel stray capacitance exceeded $50\ \Omega$, a flipped signal would indeed be produced.

Another result of this stray capacitance is that the Q-factor of the cold components (the parallel inductance and capacitance) becomes much larger than 1. The Q-factor

determines the ratio of the current in the NMR coil to the current traveling down the $\lambda/2$ cable. Thus a Q-factor much greater than 1 means that there is much more current passing through the coil than if there were no stray capacitance. This becomes important because too high a current in the coil can lead to *NMR saturation*, an effect in which the magnitude of the oscillating magnetic field created by the coil causes the majority of the sampled spins to de-flip, resulting in depolarization of the material sampled by the coil. Since the amount of stray capacitance is not known and would be difficult to measure, the degree to which saturation may have occurred also cannot be known, and thus modeling the system is not practical.

As mentioned earlier, the NMR system of E155 was often unusually difficult to tune. Often the only way to obtain a tune was with the addition of extra length to the $\lambda/2$ cable, thus breaking the condition which gives rise to its name. This extra length has the effect of changing the resonant impedance of the circuit, and thus produces further distortions to the signal. It is possible that the added cable length contributed enough inductance to the circuit to cancel the amount of stray capacitance present at the resonant frequency.

One remaining question is how a tune was possible in a circuit with its impedance altered by this anomalous capacitance. An explanation might be the following [70]: A normal NMR coil with no stray capacitance has a frequency dependent impedance similar to that shown in Figure 4.14. In this plot, the minima on the low-frequency side corresponds to the normal, whole-circuit resonance at the Larmor frequency for which the coil was designed. The maxima on the high-frequency side is a parallel-resonant frequency due to the coil's inductance and its self-capacitance treated in parallel. Normally, this peak is much higher in frequency and lies far outside the range covered by even the widest NMR scan centered on the Larmor frequency.

The presence of the parallel stray capacitance in the E155 target cell had the effect

of altering the position of the self-resonant peak, bringing it lower in frequency. For some values of the stray capacitance, the impedance curve of the coil could appear more like that in Figure 4.15. The region between the inductive minimum and the self-resonant maximum appears, if viewed across a narrow range in frequency, like the normal background Q-curve generated by the electronics of the Q Meter circuit in a properly functioning system. Thus the operators were led to believe that the system was properly tuned when it was indeed not.

A final aspect of the changes introduced by the presence of the stray capacitance is that they are predicted to be frequency-dependent, only showing up at higher NMR frequencies. Thus the measurement of other spin species, such as ^{15}N (21.59 MHz in a 5 T field), ^6Li (31.3 MHz), the deuteron (32.7 MHz), and even ^7Li (82.8 MHz) are not expected to be distorted by this effect.

Confirmation of this prediction can be found in a measurement made during the Technical Run following E155. A microwave tube having a peak output around 70 GHz – half the frequency of the tube used during E155 – was installed in the target. Using this tube, the target magnetic field (and therefore the frequency at which the NMR operated) were also halved. At this new field, the proton Larmor frequency was 106.5 MHz (Figure 4.11 shows an example of a 106.5 MHz signal).

4.4.3 Using Radiation Damage Curves as a Correction

The method used to correct the E155 target polarization is based on the polarization performance of the material as radiation damage from the beam is accumulated. This performance is compared with that of material used in a similar target setup and in a similar electron beam during E155x, and extension run to E155. The differences in the performance of the two targets is used to derive a correction to the E155 proton

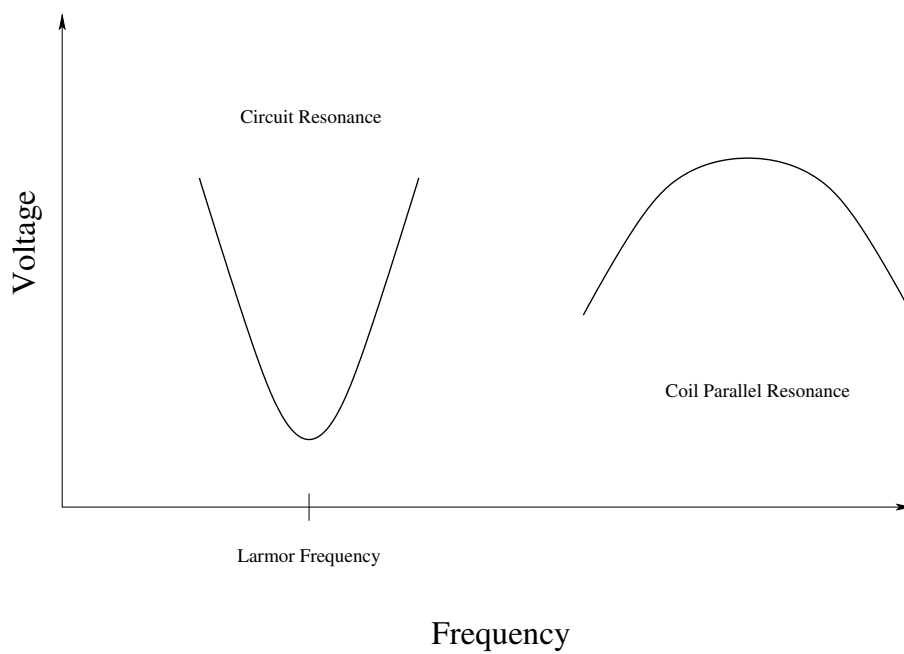


Figure 4.14: Impedance of a normal NMR coil as a function of frequency.

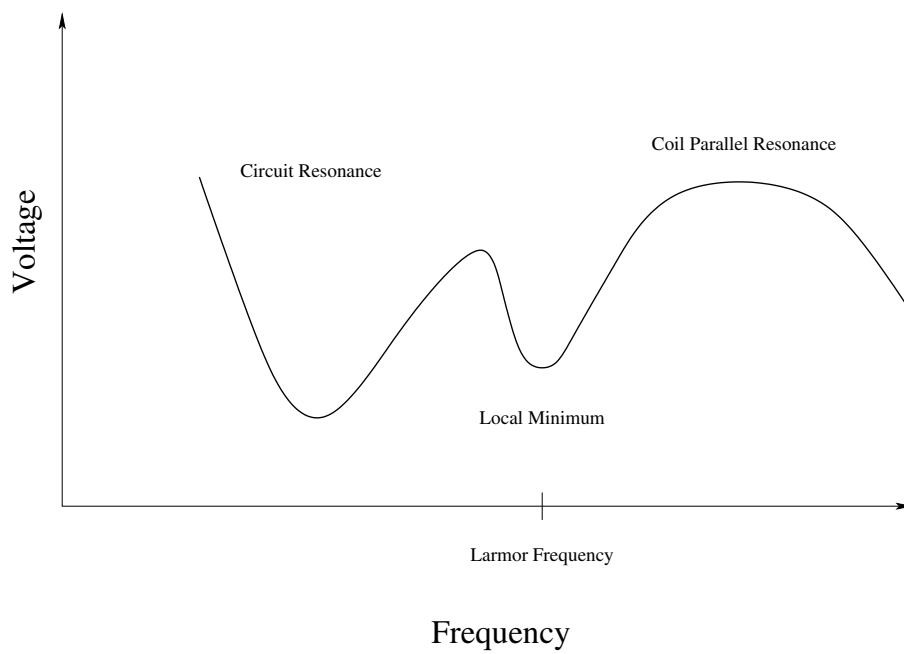


Figure 4.15: Possible impedance of an E155 NMR coil as a function of frequency.

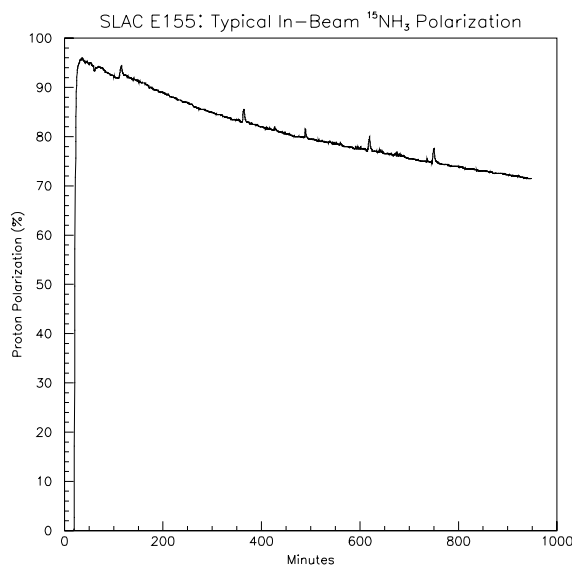


Figure 4.16: Typical decay of polarization with accumulated beam dose.

polarization data.

The effect of the beam is to create additional paramagnetic centers which allow faster nuclear spin relaxation in the target material, causing the maximum achievable polarization to decrease. An example of this is shown in Figure 4.16. After enough dose, typically 10 to 16 hours of E155 running (approximately 10 to 15×10^{15} electrons through the target), the polarization falls to unacceptably low levels. Annealing the target by raising its temperature to 80 to 90 K for half an hour (for Ammonia) restores the polarization performance of the material for another 10 to 16 hours of beam, depending on the history of the material. There were 34 of these anneal cycles during the proton running of E155, using four separate batches of ¹⁵NH₃.

Each anneal cycle taken in the experiment can be categorized into one of four groups, based on NMR coil material (copper-nickel or aluminum) and polarization sign. The majority of the data was taken with positive polarization and copper-nickel coils, and this group can be further divided into four subgroups based on the

performance of the material. A categorization of each of the 34 anneal cycles into one of these groups is shown in Table 4.2.

The four subgroups of anneal cycles taken with copper-nickel coils and positive polarization are **Cu-Pos:Fresh**, which denotes relatively new material with good performance, **Cu-Pos:Stale**, which means decreased performance, but still acceptable for efficient running of the experiment, **Cu-Pos:Poor**, which refers to the very end of the material's lifetime, when running is inefficient because of quickly decreasing polarization, and finally **Cu-Pos:Unchar**, which means that beam trips, tuning, or other problems prevented the polarization from exhibiting its typical radiation decay curve, and thus no conclusions can be made on the polarization performance.

Anneal cycles with copper-nickel coils but negative polarization are all labeled **Cu-Neg**. There are few enough of these that it is not possible to classify them further based on their performance. Similarly, anneal cycles taken with Al NMR coils fall into either **Al-Pos** or **Al-Neg**, depending on the polarization sign.

Inspection of Table 4.2 shows the normal progression of a batch of material from good to poor performance as beam dose is accumulated. One batch of material (Bottle 102,28) probably did not receive proper pre-irradiation: after briefly producing good polarization, performance quickly decreased to poor levels. However, another batch (Bottle 5,6) was particularly robust: after 13 anneal cycles with acceptable performance, a two week period under liquid nitrogen (while a second set of deuteron measurements were made) provided enough recovery that it again produced a few more good anneal cycles.

Figure 4.17 shows the performance of the four useful subsets of positively polarized E155 data as a function of accumulated dose since annealing: "f" labels runs from the **Cu-Pos:Fresh** subset, "s" stands for **Cu-Pos:Stale**, "p" represents **Cu-Pos:Poor**, and "A" means **Al-Pos**. The boundaries between these four groups of data is imme-

Bottle 5,6			Bottle 101,28		
23L	Cu-Pos:Unchar	8.4 PE	10L	Al-Neg	8.4 PE
24L	Cu-Pos:Poor	4.0 PE	11L	Al-Neg	7.4 PE
25L	Cu-Neg	2.3 PE	12L	Cu-Pos:Fresh	16.5 PE
26L	Cu-Pos:Poor	3.5 PE	13L	Cu-Neg	6.4 PE
27L	Cu-Pos:Poor	1.1 PE	14L	Cu-Pos:Fresh	13.3 PE
Bottle 102,28			15L	Cu-Neg	2.5 PE
32U	Cu-Pos:Fresh	15.5 PE	16L	Cu-Pos:Fresh	12.5 PE
33U	Cu-Pos:Fresh	15.2 PE	17L	Cu-Pos:Fresh	11.9 PE
34U	Cu-Pos:Poor	8.9 PE	18L	Cu-Pos:Fresh	17.0 PE
35U	Cu-Pos:Poor	4.9 PE	19L	Cu-Pos:Stale	8.9 PE
36U	Cu-Pos:Poor	2.1 PE	20L	Cu-Pos:Stale	4.9 PE
Bottle 7,8			21L	Cu-Pos:Stale	3.3 PE
13U	Al-Pos	6.8 PE	22L	Cu-Pos:Stale	8.8 PE
14U	Al-Pos	2.4 PE	<i>sit in nitrogen 2 weeks</i>		
15U	Al-Pos	7.1 PE	32L	Cu-Pos:Fresh	7.8 PE
24U	Cu-Pos:Unchar	20.9 PE	33L	Cu-Neg	4.1 PE
25U	Cu-Pos:Fresh	17.7 PE	34L	Cu-Pos:Poor	5.6 PE
26U	Cu-Pos:Stale	12.2 PE	35L	Cu-Pos:Poor	9.9 PE
27U	Cu-Pos:Stale	8.5 PE			

Table 4.2: Performance, by anneal cycle, of the four batches of material used in E155 g_1^p running. The number/letter code signifies the target epoch in which the cycle occurred and the target cup (Upper or Lower) in which the material was placed. The next column indicates the classification of the material's performance during that anneal cycle. The final column indicates, in peta-electrons ($10^{15} e^-$) the total beam dose delivered during the cycle.

diately obvious.

Figure 4.18 shows the performance of the two subsets that include negative polarization. “n” represents Cu-Neg data, while “a” stands for Al-Neg data.

To perform the correction, a reference data set was first obtained of target data from E155x, an experiment run as an extension to E155 to gain further statistics on g_2 . The only changes made to the target from E155 to E155x were the replacement of the metal target cavities with plastic (Kel-F) ones, and the exclusive use of copper-nickel NMR coils instead of aluminum ones.

The E155x reference set includes seven anneal cycles of positively polarized proton data, all which exhibit performance of “fresh” material. Since the beam current of E155x was significantly smaller than E155, while the calendar running time was similar, there is not sufficient dose to make a “stale” or “poor” reference set from E155x.

The first step of the correction is to derive curves representing the standard behavior of each of four E155 subsets (Cu-Pos:Fresh, Cu-Neg, Al-Pos, and Al-Neg) and of the E155x reference. Rather than fitting a functional form to the data, a binning and averaging method was used to create these standard curves. This is to avoid making any assumptions about how the polarization decays with dose – instead of forcing the data into a particular model, an average is free to follow the data wherever it may go. Each of the five average curves thus obtained represents polarization as a function of the beam dose acquired since the most recent anneal.

The correction is then made by comparing E155 and E155x polarizations taken at the same beam dose. This essentially treats the dose as a parametric variable connecting the flawed E155 measurement to the good E155x measurement. This procedure is applied separately to each of the four E155 data subsets, resulting in four correction curves.

E155 Positive Anneal Cycles

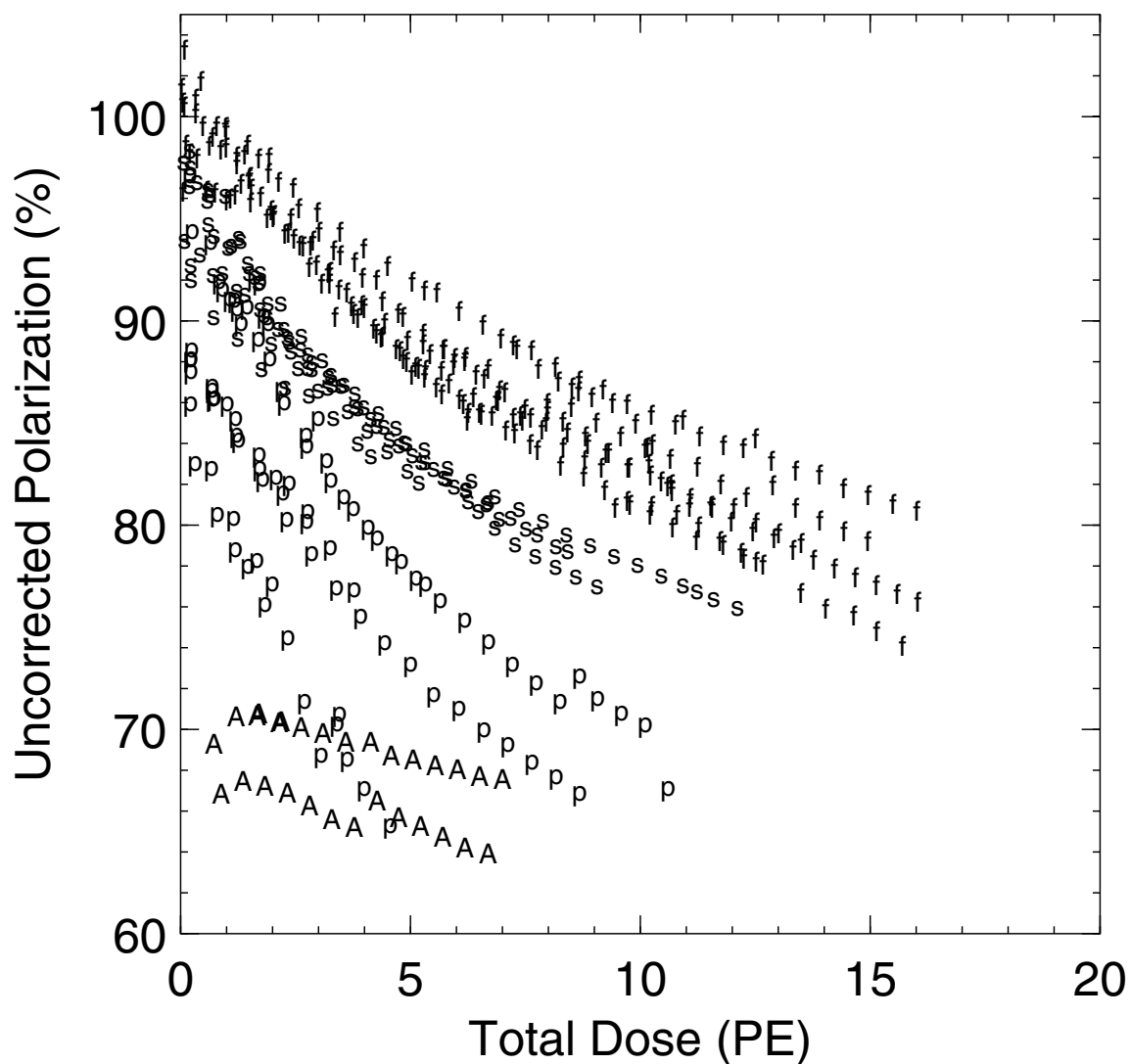


Figure 4.17: E155 positive polarization anneal cycles. Symbols refer to performance and NMR coil material, and are as follows: f - fresh material with copper NMR coils, s - stale material with copper coils, p - poorly performing material with copper coils, A - all anneal cycles taken with aluminum NMR coils.

E155 Negative Anneal Cycles

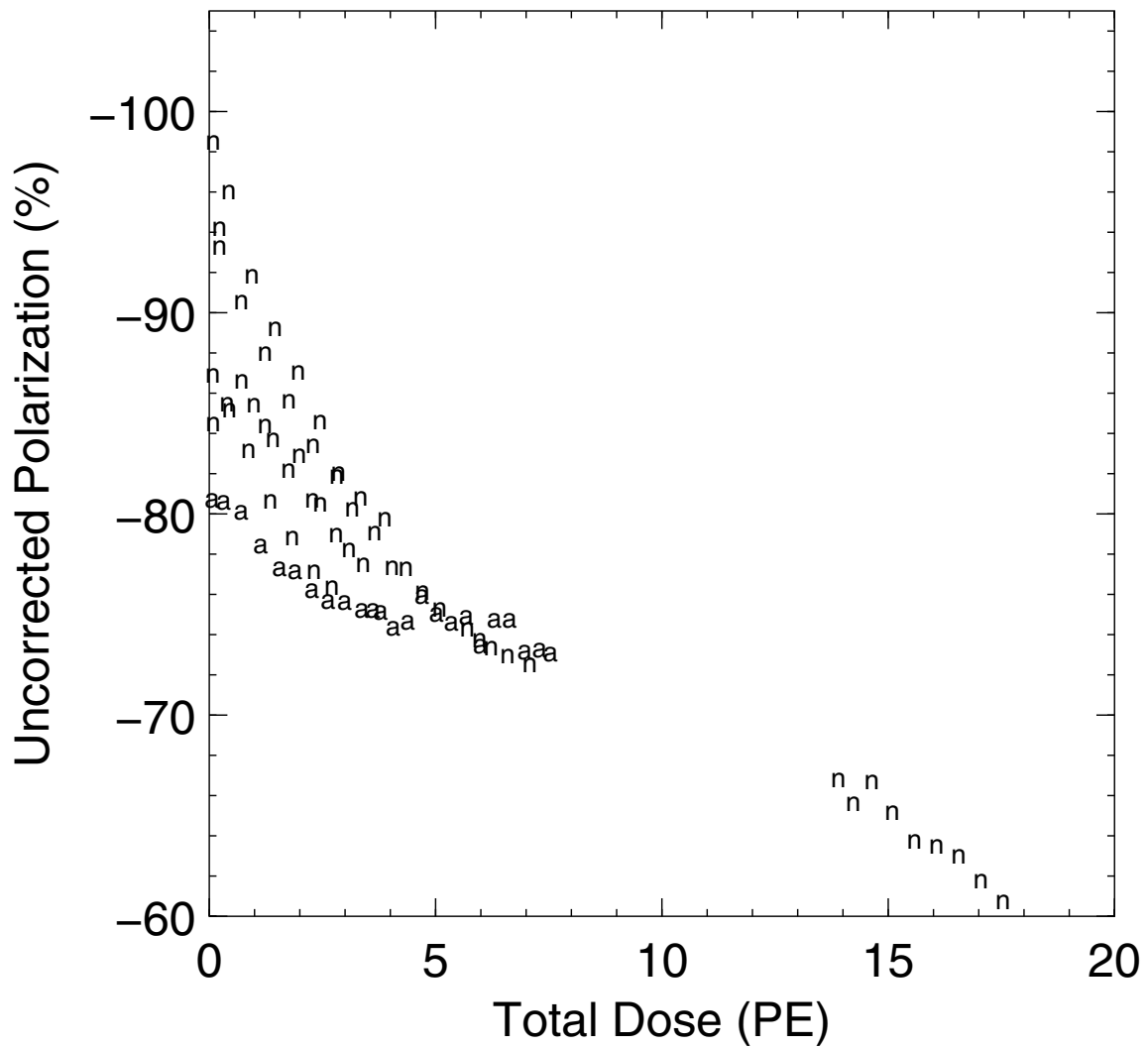


Figure 4.18: E155 negative polarization anneal cycles. Symbols refer to NMR coil material, and are as follows: n - all anneal cycles with copper NMR coils, a - all anneal cycles with aluminum coils.

The results are shown in Figures 4.19 through 4.22. Panel a) shows the data subset alone. Panel b) shows the average curve together with the data from which it came. The averaging was performed with a bin size of $0.5 \times 10^{15} e^-$. This is a typical quantity of dose occurring during one E155 run. Panel c) shows the average curve with error bars. Finally, panel d) shows the correction curve. Figure 4.23 shows the E155x reference data used.

The error on the correction comes from two sources. First the anneal cycles of each subset do not perfectly overlap each other, and that scatter produces an error in determining the average curve. Second, the individual measurements each have an error from the TE calibration and the precision of the NMR.

For the first part, the error due to scatter in the anneal cycles, the error varied not only by subset, but also on a bin by bin basis within each subset. This can be seen in the lower left panel of Figures 4.19 to 4.23. In making the average curve and computing the error, some of the bins contained only one point, making it impossible to determine error due to scatter. In these cases, an average error from the preceding bins was used. As can be seen from the figures, this results in quite a smooth progression in the size of the errors from one bin to the next.

For the second part of the error, the error due to the imprecision in the polarization measurement, the polarization error was averaged for all E155 proton measurements with absolute polarizations greater than 50%. The source of the polarization error was due to uncertainty in the calibration constant and to the statistics of capturing the NMR signal with the STAC. This average came out to be 2.5%, and was added in quadrature to the scatter error discussed above to obtain the overall error for each average curve.

Once the error for each average curve is determined, the next step is to generate the correction. This is done by plotting one of the E155 average curves against the E155x

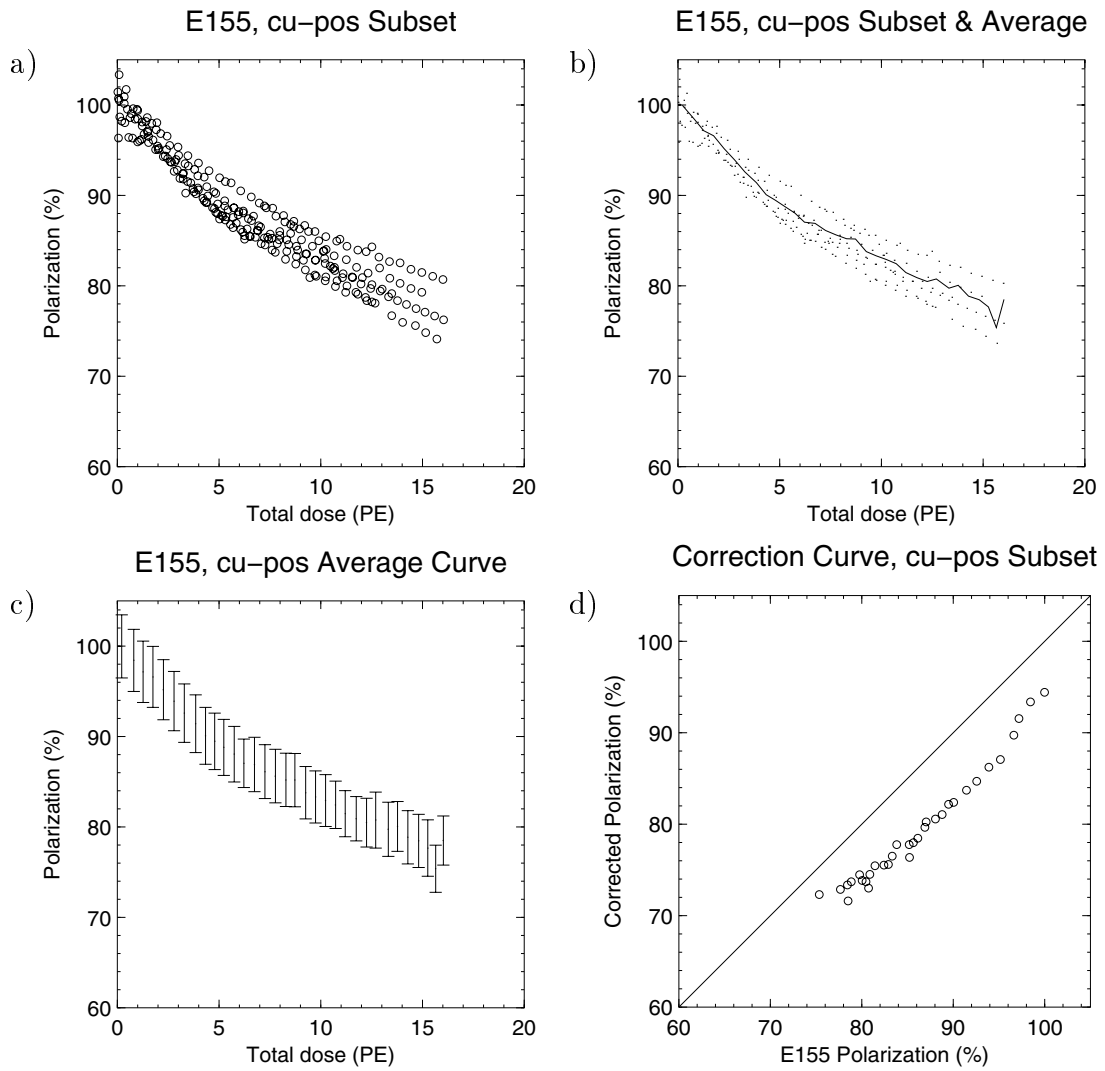


Figure 4.19: Data, averaged curve, and correction for the positive polarization, copper NMR coil subset. Only anneal cycles from the `Cu-Pos:Fresh` subset are included, in order to more closely match the E155x reference.

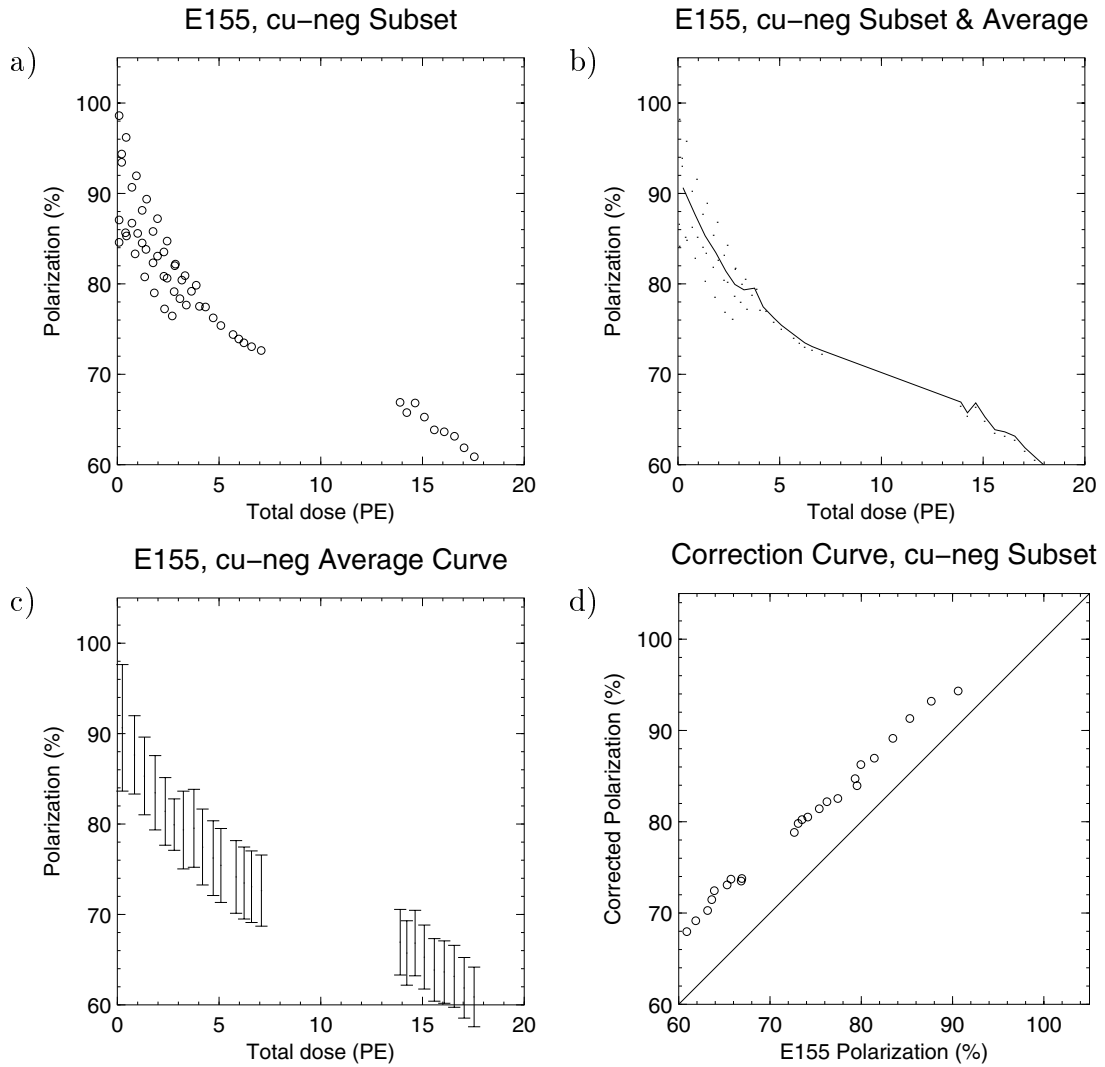


Figure 4.20: Correction for the negative polarization, copper NMR coil subset.

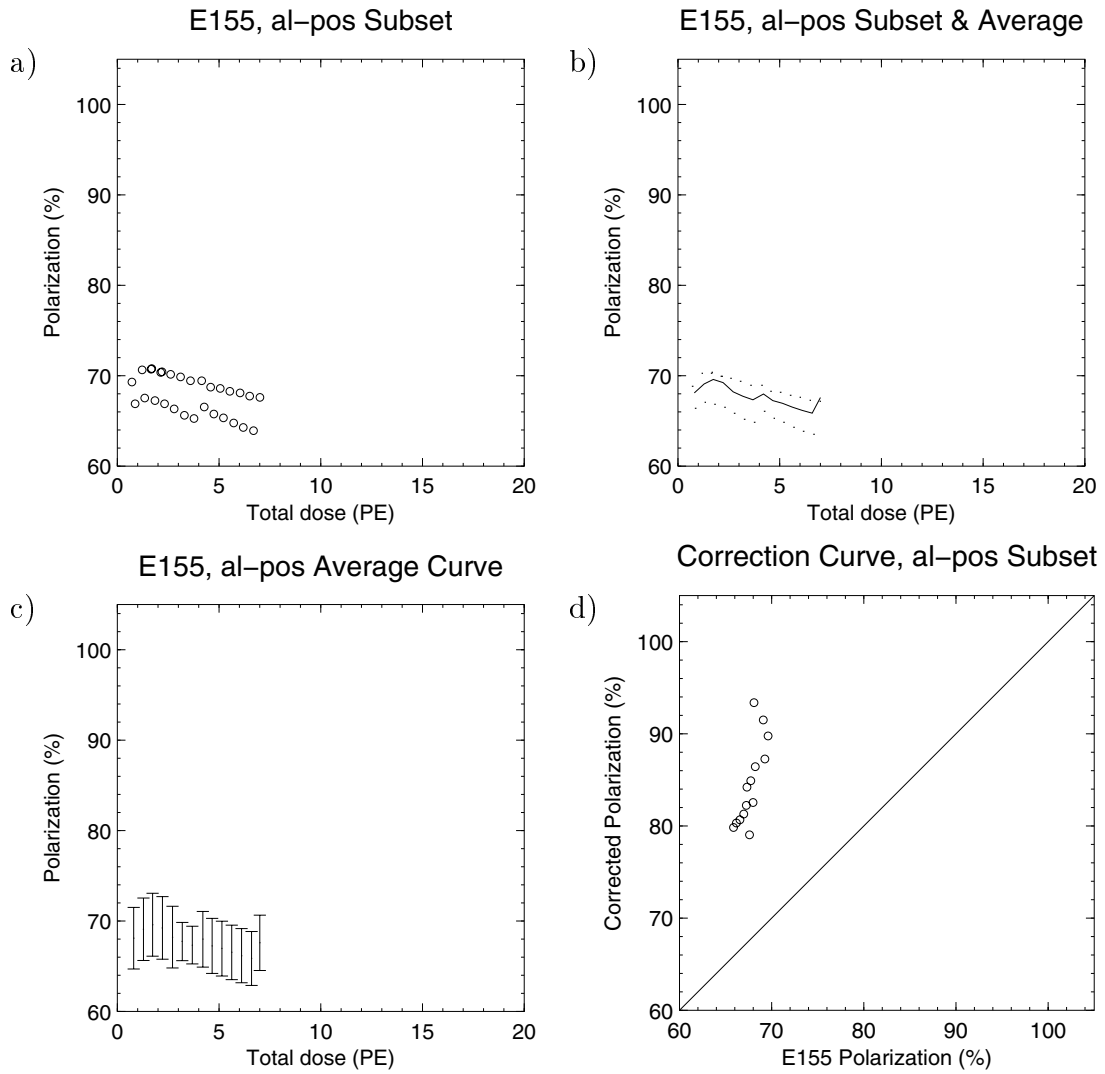


Figure 4.21: Correction for the positive polarization, aluminum NMR coil subset.

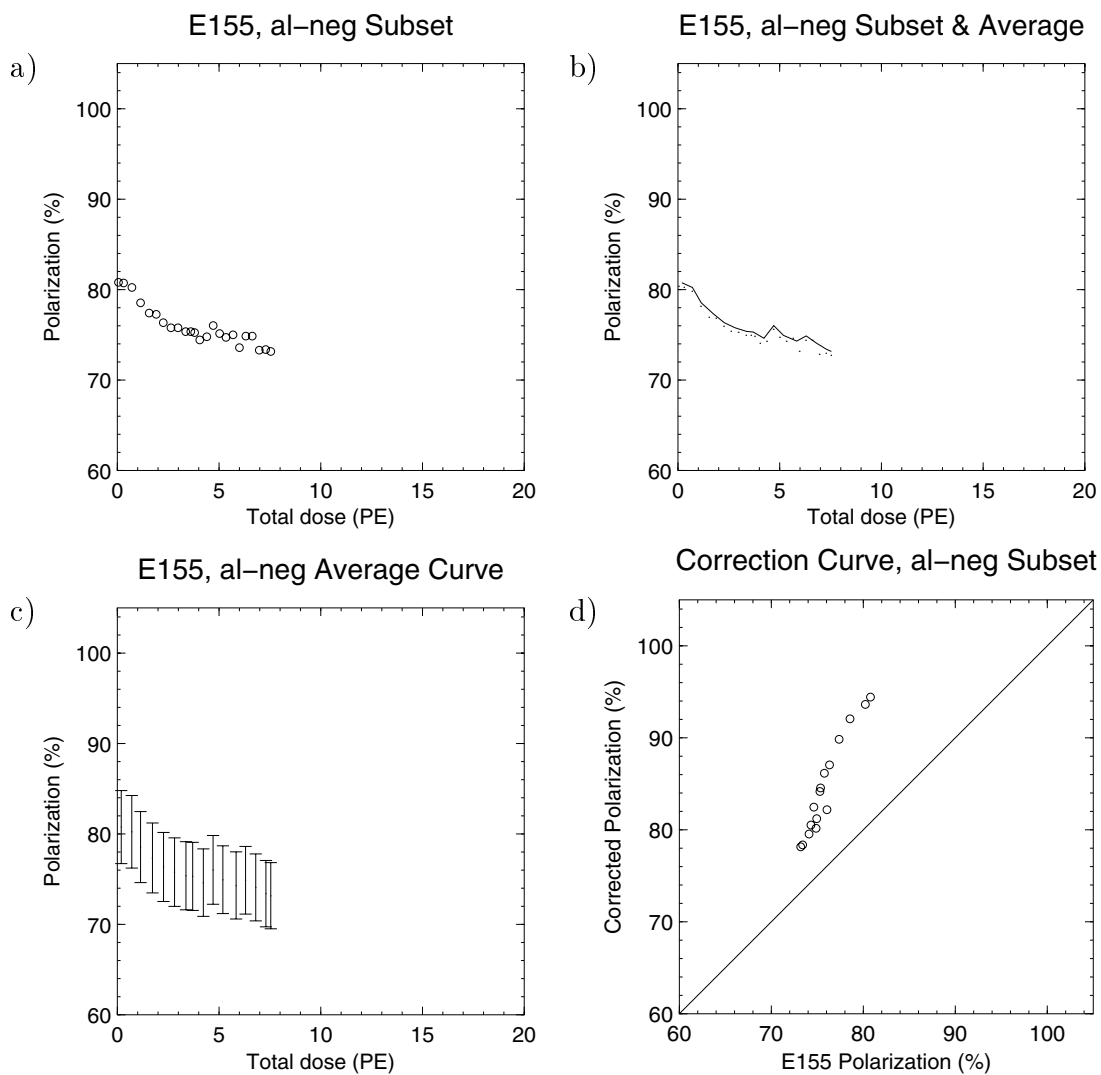


Figure 4.22: Correction for the negative polarization, aluminum NMR coil subset.

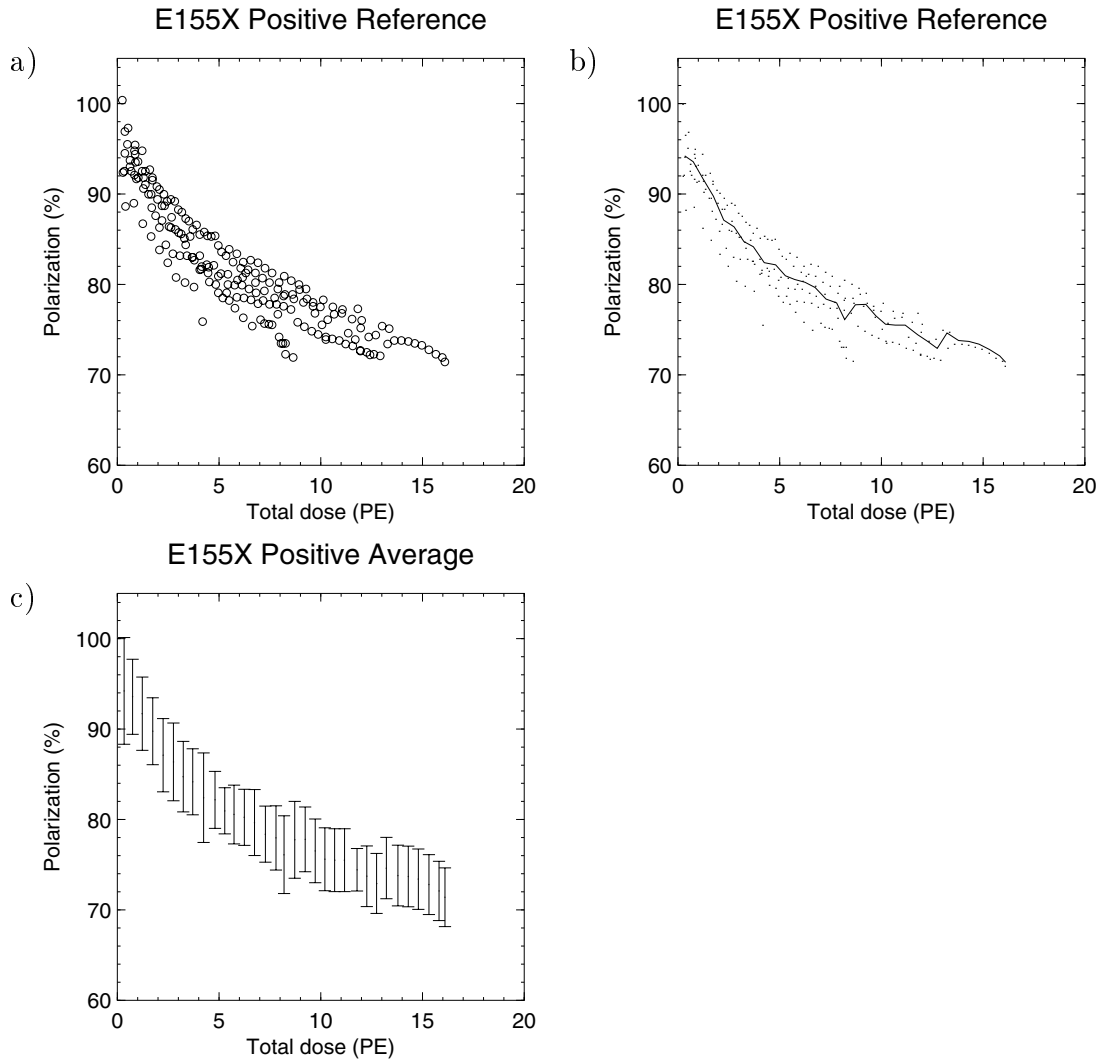


Figure 4.23: Data and averaged curve for the E155x reference set.

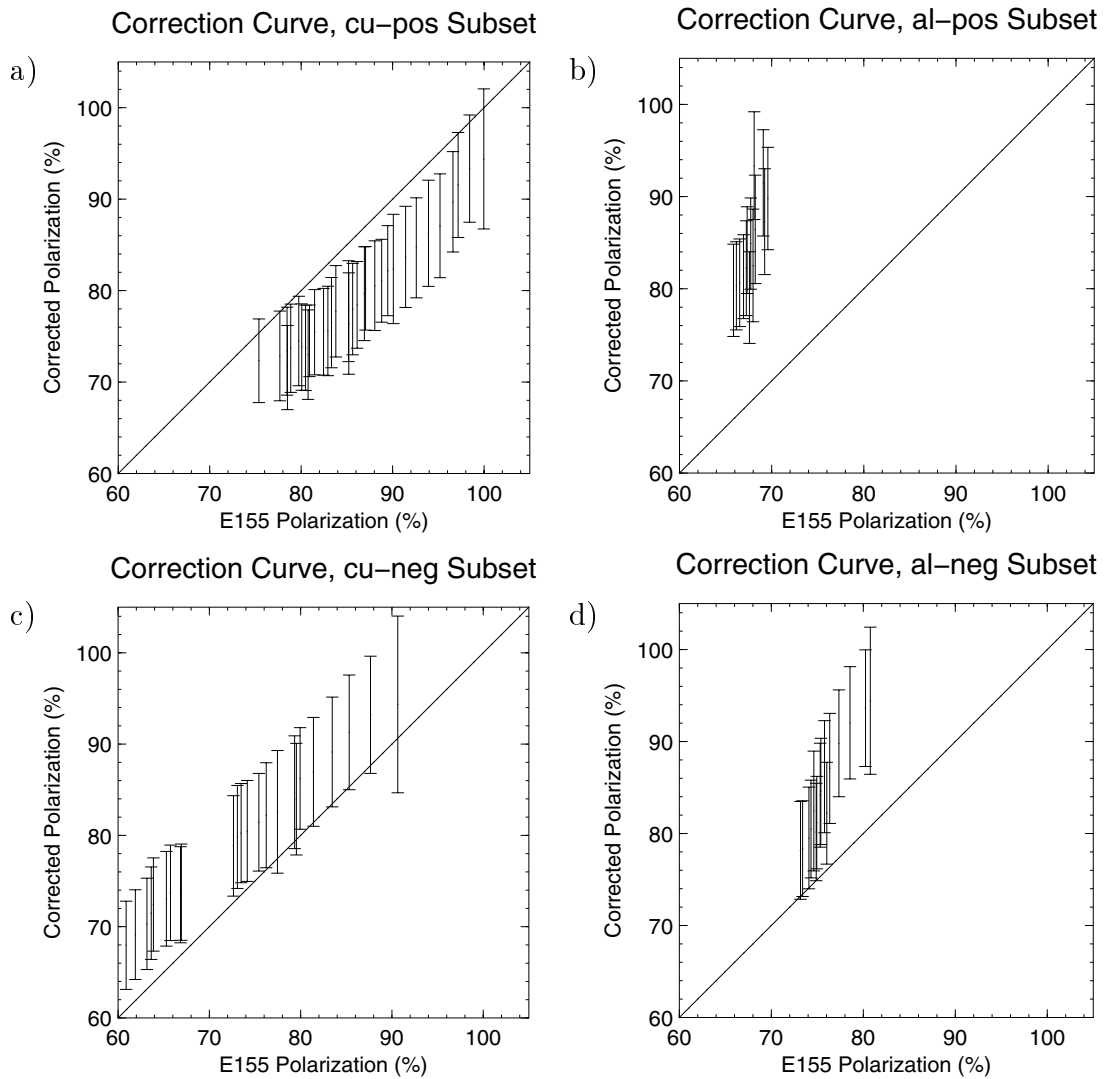


Figure 4.24: Final curves used to correct the four sets of E155 proton polarization data. The solid line represents no correction, points below it represent a reduction in polarization, while points above indicate an increase.

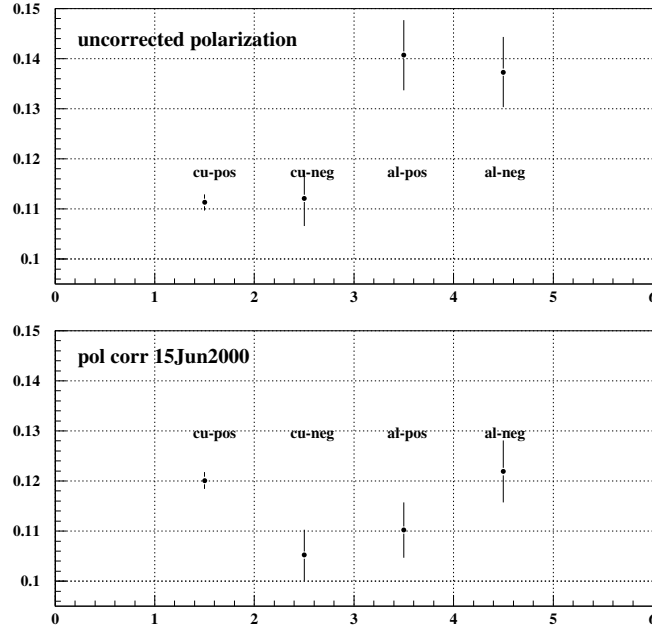


Figure 4.25: Measured region integral of g_1^p for uncorrected (top) and corrected (bottom) proton data.

reference curve. Since both of these curves depict polarization and both polarizations have errors, this plot has an error bar in both the x - and y -axis. Properly converting a plot with both x - and y -axis error bars into one with only y -axis errorbars requires care [71, 72]. For this work the two sources of error are completely uncorrelated and a quadratic sum of the x - and y -axis errors was taken for the overall error. The four final correction curves, with error bars, are shown in Figure 4.24. The average error on the measurement is 7.0%. Figure 4.25 shows the integral over the measured region of the structure function $g_1^p(x, Q^2)$ for each subset of E155 proton data. Although the correction does not result in perfect agreement among the four subsets, the large, artificial gap between the data taken with Al NMR coils and CuNi NMR coils is eliminated.

Chapter 5

Asymmetry Analysis

This chapter will discuss the results of the E155 measurement of $g_1^p(x, Q^2)$ and related issues. Section 5.1 covers the steps performed to arrive at a raw experimental asymmetry. Aspects of the equipment used in the experiment, and several physics processes require corrections to be made to the raw asymmetries to obtain the true Born asymmetries desired. These are discussed, in the order in which they were made, beginning with Section 5.2. Once the Born asymmetries are obtained, the discussion then turns to the calculation of the structure functions, their Q^2 dependence, and their integrals in Section 5.7.

5.1 Raw Asymmetries

5.1.1 Data Reduction

The smallest unit of relevant data in E155 was a single beam spill, which included the information from the beam monitoring devices and from all three spectrometers. To facilitate easy handling of the data, many spills are aggregated into a larger set known as a run. A typical run on a polarized target consists of 20 to 25 minutes

of beam time, or on the order of 150,000 spills. Such a run occupies about 1 GB of space on disk or tape. Calibration runs were usually much shorter, lasting from only a few seconds to a minute or two depending on the type of calibration, which included Pedestal runs to measure offsets in the spectrometer ADCs, LED runs to measure the Čerenkov phototube response to a pulse from a light emitting diode, Flashlamp runs to measure shower counter ADC response to a pulsed xenon light, and Toroid runs to calibrate the beam toroid coils to a known current passed through them along a wire.

Transforming the data from a polarized target run into a raw asymmetry involves a large amount of computer processing. To avoid unnecessary repetition of steps, the overall process was broken into two parts. First, the spectrometer data is processed in order to reconstruct particle trajectories from the detector signals that the traversal of the particles create. This step is known as particle tracking. Once the algorithm to perform the tracking was perfected, each run was processed and the trajectories and related information written to a new file, known as a data summary tape, or DST. This step accounts for approximately 99% of the computer time needed to identify DIS electrons in the data. The resulting DST file is typically one third the size of the raw data file. An explanation of the tracking algorithm can be found in [73].

In the second step, each particle track in a DST file is examined to determine what type of particle created it and to extract physics information about that particle. This step is usually referred to as particle identification.

5.1.2 Electron Definition

Once the DSTs were written, the task of particle identification remained. Tuning of the algorithm used to perform this step was one of the largest and most challenging

tasks in the analysis. The collection of criteria (or *cuts*) used to define tracks thought to have been produced by electrons is commonly referred to as the *Electron Definition*. The cuts which define the electrons used for the analysis of E155 are shown in Table 5.1 and can be broken down into three subparts. First, criteria are applied to the beam data to assure that the spill falls within the desired current range and that its path is parallel to the target magnetic field. Then cuts are applied to the spectrometer data to examine if the track is an electron candidate. Finally, physics quantities are constructed from the spectrometer data and criteria are applied to them to make sure these quantities are physically realistic, and that they represent candidate electrons created by Deep Inelastic events.

The beam cuts are designed to be unrestrictive. The only purpose is to eliminate spills in which the beam was in some way distorted. Examples include unusually large spot size, spill size too large or small, and beam position at the target not coinciding with the target cavity. In addition to these cuts, all four of the helicity signals are compared and must be in agreement. This cut is discussed further in Section 5.3.

The spectrometer cuts focus mostly on the quality of the data taken by the subsystems within the spectrometer. The hodoscopes were required to register time-correlated hits in three of the four planes of a hodoscope package (four of the six planes in the upstream package in the 2.75° spectrometer). The shower counters were required to have registered a cluster centered on a non-edge block. That is, the cluster must register in a group of nine blocks in a three by three block arrangement. This requirement assures that all of the energy of the particle is captured by a central block and its neighbors, rather than relying on an algorithm to reconstruct energy not captured by the detector blocks. The Čerenkov detectors were most crucial in discriminating between electrons and pions. The cut put on the Čerenkov data required the product of the peak voltage of the two phototubes be greater than a threshold

Name of Cut	Units	Criteria
<i>Beam Cuts</i>		
Foil Position	mm	$-20 \leq X, Y \leq 15$
Foil X Width	mm	$0.2 \leq X \leq 5.0$
Foil Y Width	mm	$0.1 \leq Y \leq 15.0$
Spill Monitors	ADC Channels	$0 < goodspill, badspill < 2000$
Helicity Bits		4 Signals Agree
<i>Spectrometer Cuts</i>		
Čerenkov Hits		C_1, C_2 had a hit
Čerenkov Coincidence	V	$\sqrt{C_1 C_2} > 40$
Shower Cluster	(location)	Non-edge cluster
Hodoscope Hits		In Time with Shower Cluster
<i>Kinematic Cuts</i>		
Bjorken x	none	$0.014 < x < 0.9$
Q^2	GeV ²	$Q^2 > 1$
Invariant Mass	GeV ²	$W^2 > 4$
Shower Energy/Momentum	none	$0.8 \leq E/p \leq 1.2$

Table 5.1: Cuts comprising the E155 Electron Definition.

value determined [74] by examination of electron and pion counts.

The constructed physics quantities are the final category of cuts applied. First, the energy to momentum ratio was required to fall in a range from 0.8 to 1.2, in order to select electrons over heavier particles. The energy used for this ratio is the shower counter energy, while the momentum is determined from the angle and position of the track in the spectrometer. Next, the value of Q^2 has to be greater than 1 (GeV/c)² to be in the scaling region. The calculated value of Bjorken x is required to lie within the designed acceptance of the spectrometers, $0.01 < x < 0.9$, and finally the missing mass squared, W^2 has to be greater than 4 GeV², to avoid the resonance region.

5.1.3 Run Selection

There were 4384 unique runs acquired during E155. The guidelines used during data taking instructed that changes to many experimental quantities should take place only between runs. In this way, all the variables pertinent to calculation of asymmetries can be considered constant during a run*.

For each spectrometer, separate lists of runs were maintained based on spectrometer polarity (e^-/e^+), target material ($^{15}\text{NH}_3$, ^6LiD , Be, C, LHe, hole), target magnet field direction, and target polarization sign (in the case of polarized target material). To be included in these lists, a run had to have at least 5×10^{14} electrons, stable beam current, accurate beam positioning on the target, negligible number of spills having polarization bit disagreement, properly functioning target, good DAQ system performance with no computer problems, and no equipment malfunctions.

For detection of longitudinally scattered electrons on a proton target, these cuts resulted in 575 runs for the 2.75° , 623 runs for the 5.5° , and 608 runs for the 10.5° spectrometer. Another 59 runs for the 2.75° , 38 runs for the 5.5° , and 51 runs for the 10.5° measured scattered positrons. The rest of the runs were either measurements using ^6LiD as the target material (848 runs total), or were calibration runs (such as pedestal runs used to determine ADC offsets or LED runs in which the Čerenkov phototube gains are calibrated), runs on unpolarized targets (used primarily for packing fraction analysis and acceptance cross-checks), Møller polarimeter runs (for determination of the beam polarization), or runs in which equipment malfunction or other errors interrupted data taking.

*One notable exception to this rule is the target polarization, the magnitude of which changed slightly during each run due mostly to radiation damage in the target material, but also because of changes in such factors as cryogenic operating conditions and delivered microwave power and frequency.

5.1.4 Experimental Asymmetry

Using a given specification of Electron Definition (Section 5.1.2), and a list of runs on which to apply it (Section 5.1.3), a procedure is used to build the raw experimental asymmetry separately for each spectrometer.

This procedure involves reading the DST information for the relevant runs and extracting those tracks that pass the electron definition. For each of these tracks, several physics quantities are calculated. These include the Bjorken x and Q^2 of the electron, the accumulated beam charge, and the helicity state of the spill. Totals of these quantities are maintained, placed into x -bins, and written to a file for each run. From these files, the raw counting asymmetry $(N_L - N_R)/(N_L + N_R)$ may be calculated. This is the first step in calculating the structure functions.

5.2 Asymmetry Corrections

5.2.1 Pion Background Correction

The vast majority of the tracks identified in the spectrometers come not from electrons but rather from hadrons, mostly pions electro-produced in the target. For the 2.75° spectrometer, the ratio of hadron tracks to electron tracks was about 3:1; for the 5.5° spectrometer it increased to over 10:1 [75] because the DIS cross section drops off more quickly at large angles and constant x than the hadron production cross section. Since the dominant hadron process is pion production, this part of the spectrometer data set will be referred to as the pion data for the remainder of this section.

A great deal of effort was expended in both the design of the spectrometers and the selection of the Electron Definition to assure that tracks created by pions were not misidentified as electron tracks. No process is perfect, and there exists a con-

tamination of the electron data set by pions such that a correction must be applied before final asymmetry results may be quoted.

The presence of pion contamination affects the experimental asymmetry in two different ways. First, there is an artificial inflation of the total number of hits in the spectrometer that we count as electrons. Thus our counts N_L and N_R are too large, which reduces the experimental asymmetry, $A_{exp} = (N_L - N_R)/(N_L + N_R)$. In this way, the pion contamination behaves like a dilution of the asymmetry (see Section 5.4 for discussion of the target dilution factor).

Second, there may also be an asymmetry in the production of the charged pions. Thus, the pion contamination in the electron data is helicity dependent. This pion production asymmetry must be measured and subtracted in order to isolate the electron asymmetry.

To correct for the pion contamination we must measure the fraction of identified electron tracks that are actually misidentified pions, n_π . This is done in two steps. First, a pion definition (similar to the electron definition, but requiring no Čerenkov signal and $E/p < 0.2$) is used to reveal the distribution of pions in the spectrometers, and a fit is made to this shape. This fit is then normalized to the electron distribution in the range $0.2 \leq E/p \leq 0.4$, and subtracted from the electron distribution. The same pion definition is used to measure A_π , the pion asymmetry. Figures 5.1 and 5.2 show the results of these measurements[†].

Once n_π and A_π are measured, the corrected electron asymmetry is then determined as

$$A_{no\ pions} = \frac{A_{meas} - n_\pi A_\pi}{1 - n_\pi}. \quad (5.1)$$

[†]This measurement was not possible in the 10.5° spectrometer because the lack of redundant detector elements made development of a pion definition impossible. n_π and A_π are taken to be zero for this spectrometer.

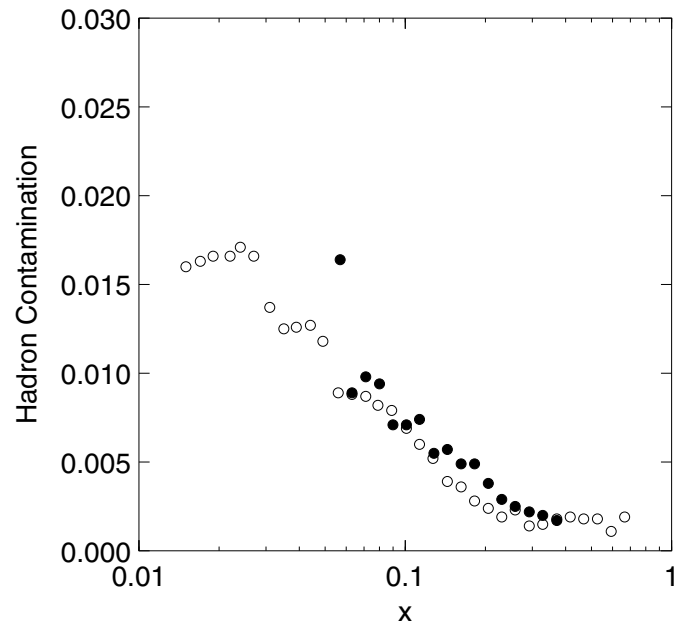


Figure 5.1: Measured hadron contamination in the 2.75° (open circles) and 5.5° (filled circles) spectrometers.

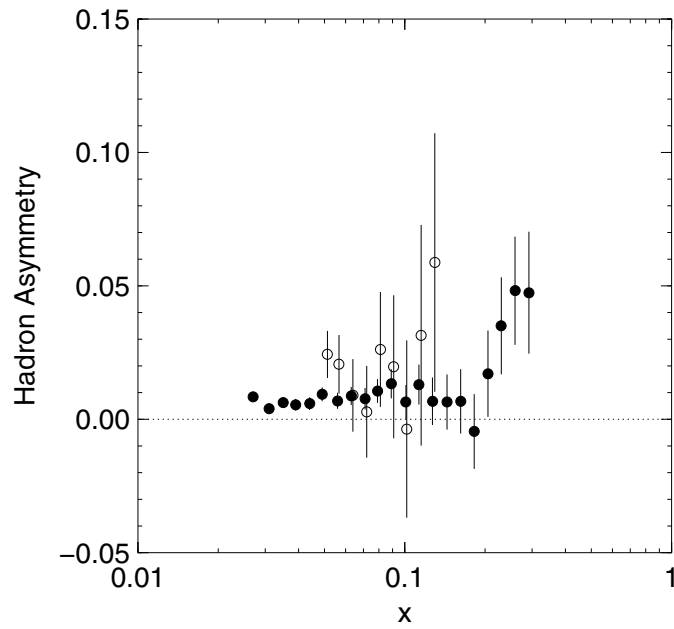


Figure 5.2: Measured hadron asymmetry in the 2.75° (open circles) and 5.5° (filled circles) spectrometers.

5.2.2 Charge-Symmetric Processes

Another correction performed on the raw asymmetry concerned not the misidentification of other particles as electrons, but rather the inclusion in the electron data set of electrons coming from processes other than deep inelastic scattering. Such processes include $\gamma \rightarrow e^+e^-$ from bremsstrahlung, decay of a $\pi^0 \rightarrow 2\gamma \rightarrow \gamma e^+e^-$ from nuclear fragmentation, etc. Unlike in Section 5.2.1, the number of these electrons cannot be measured by applying a different particle definition. Instead, as these are charge symmetric processes, the polarity of the spectrometer magnets is reversed, so that the spectrometers instead measure positrons. With the assumption that all positrons come from pair-symmetric processes, the contamination and asymmetry from these non-DIS events can be measured and a correction applied to the electron asymmetry in a manner very similar to that for pion contamination:

$$A_{e^-} = \frac{A_{no\ pions} - n_{e^+} A_{e^+}}{1 - n_{e^+}} \quad (5.2)$$

Figure 5.3 shows the measured values for the positron contamination, and Figure 5.4 shows the measured positron asymmetry. For completeness, it should be mentioned that in making the electron/positron asymmetry for the 2.75° and 5.5° spectrometers, the pion correction discussed in Section 5.2.1 was performed twice. Once for runs with the spectrometers in electron mode, and separately for runs with the spectrometers in positron mode. The 10.5° spectrometer lacked a pion definition, so the measured positron contamination contains a small fraction of pion events. This compensates for the lack of a formal pion correction as discussed in Section 5.2.1.

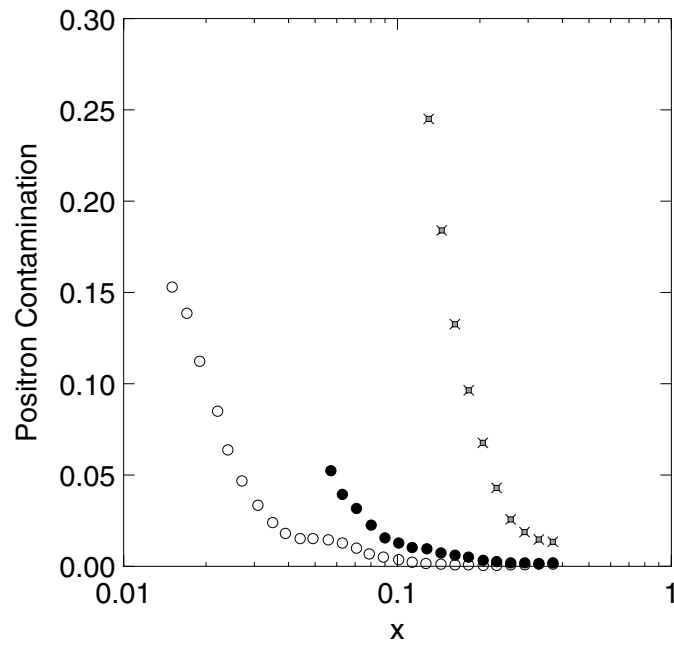


Figure 5.3: Measured positron contamination in the 2.75° (open circles), 5.5° (filled circles), and 10.5° (crossed squares) spectrometers.

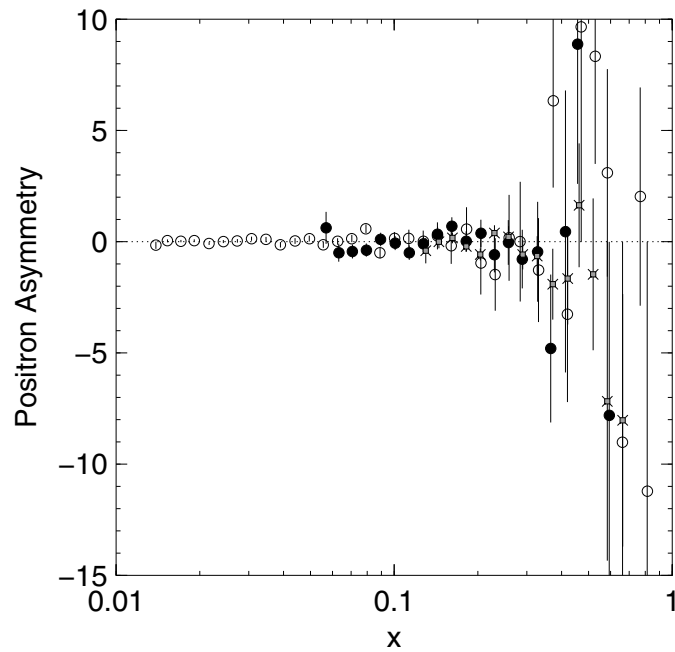


Figure 5.4: Measured positron asymmetry in the 2.75° (open circles), 5.5° (filled circles), and 10.5° (crossed squares) spectrometers.

5.2.3 Electro-Weak Correction

The vast majority of scattering events in E155 involve electromagnetic interactions between the electron and the quark in which a virtual photon is exchanged. Weak interactions, involving the exchange of a W^\pm or a Z^0 , are suppressed because at these kinematics $Q^2 \ll M_Z^2$, but are present and a small correction to the data must be applied.

The derivation of this correction in the literature [76] applies to isoscalar targets. The assumption is made that this correction is pertinent to the $^{15}\text{NH}_3$ proton target used in E155. The effect is sensitive only to the direction of the beam polarization, not to that of the target. Thus this correction breaks a symmetry normally present in our equation for A_{exp} .

Normally, scattering of beam electrons with their polarization in the direction of the beam from target nucleons with their polarization in the direction of the beam yields the same cross section as scattering of electrons with polarization opposite the beam off target nucleons with their polarization opposite the direction of the beam. In other words,

$$\sigma^{\uparrow\uparrow} = \sigma^{\downarrow\downarrow}. \quad (5.3)$$

The inclusion of weak interactions means that Equation 5.3 no longer holds. The weak interaction effects would not be seen if equal amounts of data were taken with the target polarized in each direction. As mentioned in Section 4.4, there was a strong preference to operate the target in positive polarization since the size of the online polarization values obtained were so much greater than with negative polarization. As a result, a correction to the proton asymmetries of about 1% was made [77].

5.2.4 Rate Dependence

In experiments that measure asymmetries, unlike experiments that measure absolute cross sections, determination of the absolute detection efficiency of the spectrometers is not necessary, since the efficiency cancels in the equation for A_{exp} . What is much more important in asymmetry experiments, however, is determination of the relative variation in the efficiency with the rate of particles entering the spectrometer.

By definition, a scattering asymmetry means that one helicity state has a cross section larger than the other. The particle rate in the spectrometer is therefore greater for one helicity state than the other. If, at this higher rate, the spectrometer were not as efficient at detecting electrons, this difference in cross sections is measured to be smaller than it actually is. Thus the rate dependence of the detector efficiency must be measured and a correction applied.

The method of determining this rate dependence is that developed for E154[78], known as “pulse fiction.” The basic technique is to combine the raw spectrometer data from two beam pulses of the same helicity and create a single, synthetic pulse from them in which the spectrometer rates are roughly twice their normal values. The tracking code is then run on this synthetic, double-rate pulse, and the detection efficiency calculated. By extrapolation between the efficiencies at normal and double rate, the dependence of the efficiency with rate may be determined.

As might be expected, the efficiency decreases with increasing rate [79]. Thus the rate dependence correction results in an increase in the asymmetry. The change is on the order of 1% [80].

5.3 Beam Quantities

5.3.1 Møller Polarimeter Measurements

As discussed in Section 3.1.5, both a single-arm and a double-arm Møller polarimeter were used for beam polarization measurements during E155. The detectors shared a common target foil, and used the same bending magnet. Møller runs were typically scheduled to take place during down times of other parts of the experiment – often target anneals provided the best opportunity – and occurred on average about every three days of running.

Analysis of the single-arm detector was the most extensive. Factors included in the calculation of the analyzing power of this detector included multiple scattering in the detector elements, bremsstrahlung, resolution of the detector, a gap between silicon pads in the detector, and the Levchuk effect [36]. (See Section 3.1.5 for a diagram of the detector and a discussion of the Levchuk effect.) The value given by the single-arm polarimeter is 0.813 ± 0.02 for the entire run, with the error arising from systematic effects only since the error on the statistics of the measurement was negligible.

Analysis of the double-arm detector included corrections for dead time in the detectors and for crosstalk between adjacent detectors. Although the results of the double-arm measurements agree with those of the single-arm, extensive investigation of the systematic errors in the double-arm detector was not performed, so the single-arm measurement is generally considered more reliable. The value obtained from the double-arm is 0.805 ± 0.03 , again the error being from systematics only.

Analysis of each of the individual Møller measurements showed no statistically significant variation with time, so the beam polarization is treated as a constant value for this analysis. Figure 5.5 shows individual measurements from the single

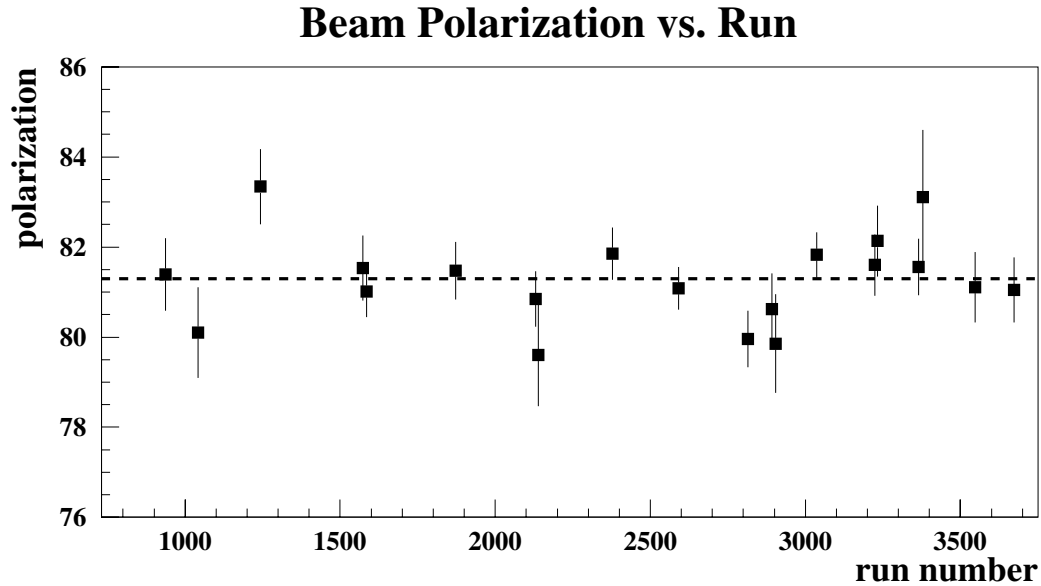


Figure 5.5: Beam Polarizations measured with the Single-Arm Møller Detector as a function of run number.

arm Møller as an example. For use in the asymmetry analysis, a weighted average of the single- and double-arm detectors was used, resulting in a final value of 0.810, with a error of 0.02 due to the high degree of correlation in the errors of the two detectors.

5.3.2 Reporting of Beam Helicity

As with any experiment that seeks to measure an asymmetry between spin states, proper reporting of the helicity of each beam spill is crucial for E155. To help assure that this information was recorded properly, four independent signals reported spill helicity, known as the PMON, MACH, SCALER, and VETO lines. Each of these signals is capable of indicating one of four different states: positive helicity, negative helicity, unpolarized beam, and error condition.

As was discussed in Section 5.1.2, part of the electron definition was that all four of these signals report the same beam helicity. This is important because the

occurrence of signal errors with one helicity state more than the other can introduce false asymmetries in the data. During an extension run to E155, extensive studies [81] were made of the cases when there is disagreement among these four signals. The conclusion of this investigation is that there is no false asymmetry created by the elimination of spills with conflicting helicity signals.

5.4 Dilution Factor

In order to determine the physics asymmetries, one must account for the fact that scattering occurs not only from polarized nucleons in the target, but also from unpolarized nucleons in the target and non-target materials. These unpolarized materials “dilute” the measurement of the physics asymmetry and are accounted for in the asymmetry expression with the variable $f(x)$ – the dilution factor

$$A_{Born} = \frac{1}{fP_B P_T} A_{e^-} \quad (5.4)$$

Components that contribute to the dilution factor include some parts of the target insert, such as NMR coils, temperature sensors, and liquid helium, in addition to beam windows in the insert, the target tailpiece, the helium shield, the nitrogen shield, the outer vacuum can, and several other parts of the beamline. The drift space between the target and the entrance to each spectrometer also contained a pair of windows on a helium bag used to fill this space. In addition, the target material itself does not consist only of polarized nucleons – most of the nucleons in a molecule of target material are unpolarized; in $^{15}\text{NH}_3$ 15 of 18 nucleons are unpolarized[‡]

Due to the two-bounce geometry of the spectrometers, scattering from many com-

[‡]Correction for the polarization of the unpaired proton in ^{15}N is discussed in Section 5.5.

ponents far from the target is outside the spectrometer acceptance and therefore does not need to be considered. Some components near the target, however, were in the spectrometer acceptance, and therefore some of the electrons identified in the analysis were not from the polarized material in the target.

To determine f , the ratio is calculated of scattering events from polarized target material to scattering events from all materials in the spectrometer acceptance [82, 83]. To do this, the amount of each type of material in the acceptance must be determined and multiplied by the total cross section for each of these elements:

$$f = \frac{N_t \sigma_t}{N_t \sigma_t + \sum_i N_i \sigma_i}, \quad (5.5)$$

where N_t is the number of polarized free target nucleons (this excludes the unpaired proton in ^{15}N), σ_t is the Born cross section for the target nucleons, and the index i is over all non-target materials. The x and Q^2 dependence of all σ and of f has been omitted for clarity. There is also a slight correction [84] made due to variations in spectrometer acceptance along the beam path. The correction introduces a scale factor in front of the $N_i \sigma_i$ term of Figure 5.5 that depends on the z location of each material under consideration. The result is a slight increase in the dilution factor, of 0.5%, 2%, and 5% for the 2.75° , 5.5° , and 10.5° spectrometers, respectively. Figure 5.6 shows the corrected dilution factor as a function of x for each of the three spectrometers.

For most of the components in the spectrometer acceptance, determination of N , the number of nucleons in the beam's path, is a simple task of knowing the molecular content of the material, its density, and the thickness of the material in the beam path [85]. This is not the case for the target material itself, however, since the material existed in the form of chips of irregular shape. As a result, although we know the

target consisted of actual material surrounded by liquid helium, it is not directly possible to state how much of each was present along the 3 cm length of the target cell.

For this reason, a study of the target material *packing fraction* was made. The packing fraction is defined as the portion of the target thickness, as seen by the beam, that actually contains target material. This number is determined by building a ratio of the total scattering rate from the polarized target to the total scattering rate from its corresponding solid disk target. Pyrolytic graphite was used for the solid reference target for $^{15}\text{NH}_3$ material, and pure Beryllium for the solid reference target for ^6LiD . The thicknesses of the reference targets were chosen so as to closely match the expected number of radiation lengths presented by the polarized target material [61].

Once the ratio of the measured polarized target rate R_t to measured reference target rate R_{ref} is made, it is compared to a model indicating what the ratio should be:

$$\frac{R_t}{R_{\text{ref}}} = \frac{p(\sum_i R_i) + (1-p)R_{He} + R_{\text{unpol}}}{R_{\text{disk}} + R'_{He} + R_{\text{unpol}}}, \quad (5.6)$$

where p is the packing fraction, i indexes the various elements in the target material, R_{He} is the rate from the liquid helium in and amongst the target material, R_{disk} is the rate from the reference target material, R'_{He} is the rate from the liquid helium on either side of the reference target, and R_{unpol} is the rate from all other material. R_{disk} , R_{He} , and R_{unpol} are calculated using the density and the quantity of each of the materials, combined with experimental fits to $F_2(x, Q^2)$ for the proton and neutron, a parameterization of the EMC factor for each material, and a multiplicative factor to account for unpolarized radiative corrections.

Solving Equation 5.6 for p yields the packing fraction. For the various $^{15}\text{NH}_3$

target loads, p ranged from $0.522 \pm .026$ to $0.610 \pm .021$ [86]. Figure 5.7 shows the packing fraction as a function of x for one of the E155 target loads (insert number 4, upper target cavity). It is independent of x , as expected, and the same for both the 2.75° and the 5.5° spectrometer.

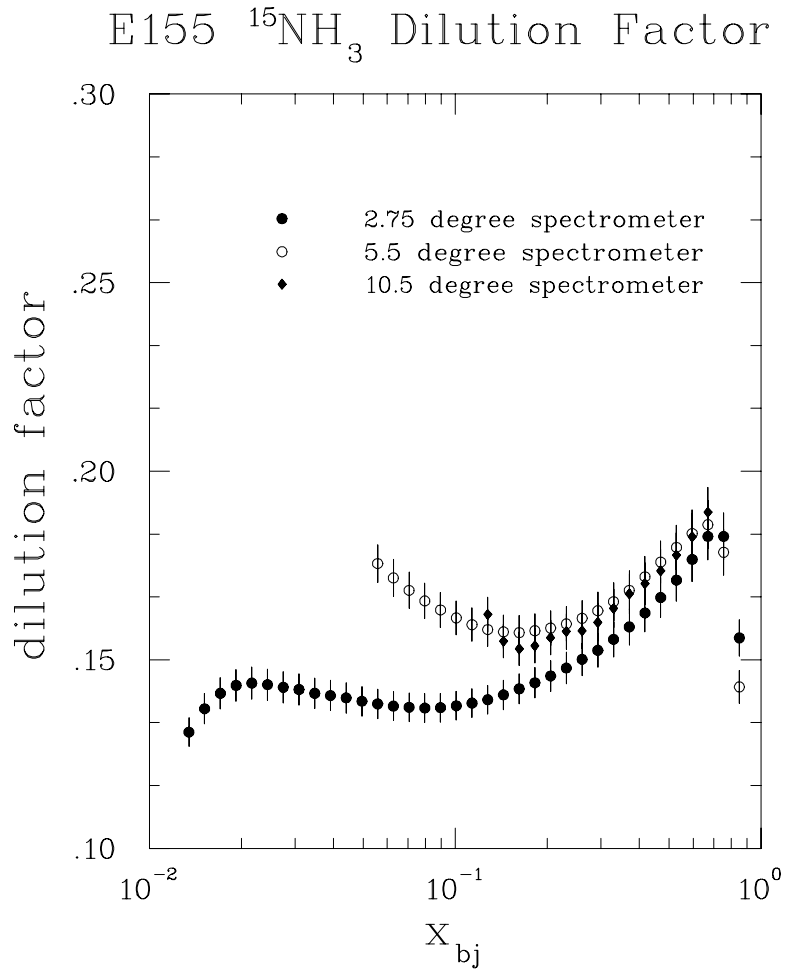


Figure 5.6: Dilution factor for the three E155 spectrometers.

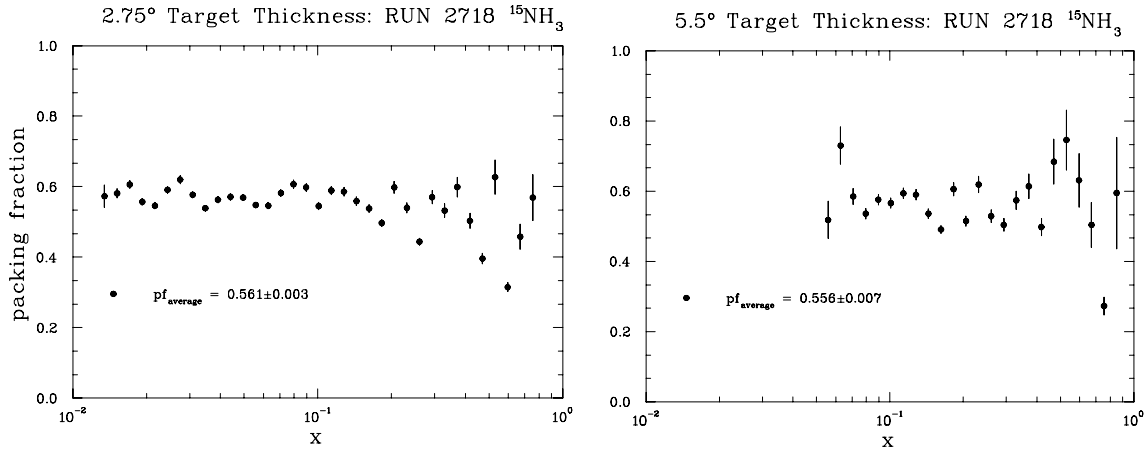


Figure 5.7: Packing fraction as a function of x for an E155 target.

5.5 Nuclear Corrections

As mentioned in Section 5.4, electrons scattered from non-target materials are a contamination in the data. Since these materials are not polarized, the scattering from them is not helicity-dependent, and therefore the dilution factor is an appropriate method of correcting the data.

A smaller contamination, similar to that described above, exists due to scattering from additional *polarized* species in the target. Correction of this contamination cannot be accommodated by the dilution factor – the polarization of the contaminating species imparts a scattering asymmetry and thus the contamination is different for the two beam helicity states.

The target insert was designed so that the target material was the only polarized substance both within the raster pattern of the beam and the acceptance of the spectrometers[§]. The only correction needed is therefore due to any additional polarized species in the target material.

[§]The target cavity also contained a small amount of plastic, used to insulate the $\lambda/2$ cables as they penetrate the cavity wall. Although this plastic does have a very small polarization, it was outside the beam raster pattern.

Variable	Value	Description
$f_{^{14}\text{N}}$	0.02	Fraction of N actually ^{14}N
$n_{^{15}\text{N}}/n_p$	1/3	Ratio of ^{15}N nuclei to protons
$P_{^{15}\text{N}}$	Equation 4.17	^{15}N polarization
P_p	(measured)	Proton polarization
$\beta_{^{15}\text{N}}$	-1/3	Unpaired proton to ^{15}N polarization ratio
$g_{^{15}\text{N}}$	≈ 1	x -dependent EMC factor for ^{15}N [87]

Table 5.2: Variables used in ^{15}N nuclear correction.

In the case of $^{15}\text{NH}_3$ there are two polarized species: the free protons in the hydrogen atoms and the nitrogen nuclei. The ^{15}N nucleus contains a single unpaired proton, and thus contributes to the overall number of polarized protons in the material. The magnetic moment of ^{15}N is opposite in sign to that of hydrogen, thus the unpaired proton is polarized in the opposite direction as that of the free protons.

To account for the presence of the polarized ^{15}N , the proton polarization is multiplied by a correction factor given by [83]

$$C_1 = 1 + (1 - f_{^{14}\text{N}}) \frac{n_{^{15}\text{N}}}{n_p} \frac{P_{^{15}\text{N}}}{P_p} \beta_{^{15}\text{N}} g_{^{15}\text{N}}. \quad (5.7)$$

where Table 5.2 lists the definitions of the variables and the values used.

The average value of C_1 was 1.024.

5.6 Radiative Corrections

Figure 2.1 presents the Feynman diagram of the fundamental scattering process of interest in E155. Proper calculation of the nucleon structure functions requires that the kinematic variables used are those defined at the vertex. Measurement of these variables is complicated by a number of radiative processes that modify the kinematic quantities at the vertex.

An example is the electron emitting a photon through bremsstrahlung after scattering from the nucleon. The shower counter in the spectrometer would then measure an energy lower than E' , the final-state energy of the electron after the scattering, because of the energy given to the photon. Correcting the measured kinematic quantities for the effects of these interactions is known as *radiative corrections*.

The interactions that require radiative corrections can be divided into two classes, known as internal and external processes. External processes are those in which the incident electron loses energy, usually through emission of a photon, before the deep inelastic scattering event, or those in which the outgoing, scattered electron loses energy before detection in the spectrometer. Feynman diagrams of these processes are shown in Figure 5.8. Internal processes are those in which the actual scattering takes place through a different Feynman diagram. Examples include vacuum polarization of the virtual photon and interactions requiring vertex corrections, which are depicted in Figure 5.9.

E155 used a procedure similar to that of E154 [88] in which the radiative corrections are broken into an additive and a multiplicative factor – $A_{\text{RC}}(x, Q^2)$ and $F_{\text{RC}}(x, Q^2)$ – defined in the equation

$$A_{\text{Born}}(x, Q^2) = A_{e^-}(x, Q^2)/F_{\text{RC}}(x, Q^2) + A_{\text{RC}}(x, Q^2) \quad (5.8)$$

where $A_{\text{Born}}(x, Q^2)$ is the desired cross section of the diagram of Figure 2.1 and $A_{e^-}(x, Q^2)$ is the measured electron cross section, the result of all the corrections discussed in Sections 5.2 through 5.5. $F_{\text{RC}}(x, Q^2)$ is often called the *radiative dilution factor* since, like the target dilution factor f of Section 5.4, it multiplicatively reduces the overall asymmetry. It is used to account for events originating at a higher x than that measured by the spectrometers, that end up in the bin of interest. $A_{\text{RC}}(x, Q^2)$ is known as the *polarized radiative correction factor*. It adjusts the asymmetry to account for processes that involve radiation of a photon before the emission of the virtual photon that couples to the nucleon. These processes change the polarization of the incident electron before the interaction with the nucleon.

The radiative corrections are calculated by a program, developed at SLAC by L. Stuart, known as RCSLACPOL, based on the technique of [89]. This program calculates the Born asymmetry from a model which uses polarized and unpolarized structure functions, nuclear form factors, $R(x, Q^2)$, Pauli suppression factors, H and D cross sections, and a target model as input. It then applies corrections to this asymmetry to account for lepton and hadron vacuum polarization, multiple photon exchange, lepton and multiple soft photon bremsstrahlung, radiative tails from other kinematic regions, and peaking approximations. Values of A_{RC} and F_{RC} are then calculated to account for the difference between the Born asymmetry and the radiatively-corrected Born asymmetry via Equation 5.8.

It should be noted that a circular arrangement exists in that the calculation of the Born asymmetry requires the polarized structure functions as input, and yet those functions are exactly what are being sought to determine the Born asymmetry. The solution is to solve for both the corrected and uncorrected asymmetries and the radiative corrections through an iterative process [90], as explained below.

A fit is made to the virtual photon asymmetry A_1 using the functional form

$$A_1(x, Q^2) = x^\alpha(a + bx + cx^2)(1 + \beta/Q^2). \quad (5.9)$$

This fit is performed on a set of radiatively-corrected data from past experiments, plus uncorrected data from E155 and previous SLAC experiments (E80, E130, E143, and E154). A_1 was chosen so that the positivity limits requiring $|A_1| \leq 1$ (Equation 2.29) could be used to test the fit. This fit is performed simultaneously to proton and neutron data, with a set of the parameters α , a , b , c , and β maintained for each. Experiments reporting data on the deuteron structure functions were included in the fit by use of the relation

$$A_1^n(x, Q^2)F_1^n(x, Q^2) = \frac{2A_1^d(x, Q^2)F_1^d(x, Q^2)}{1 - 1.5\omega_D} - A_1^p(x, Q^2)F_1^p(x, Q^2), \quad (5.10)$$

where ω_D is the D -state probability of the deuteron.

This fit is then used as input to RCSLACPOL to calculate the Born asymmetries and the radiative corrections in the first iteration. The radiative corrections that result are then applied to the measured E155 data, the fit procedure is repeated, and RCSLACPOL run another time. This process continues until convergence, which typically took fewer than 10 iterations.

The resulting corrections [91] increased the proton asymmetry $A_{||}$ by up to 30% in the low- x bins.

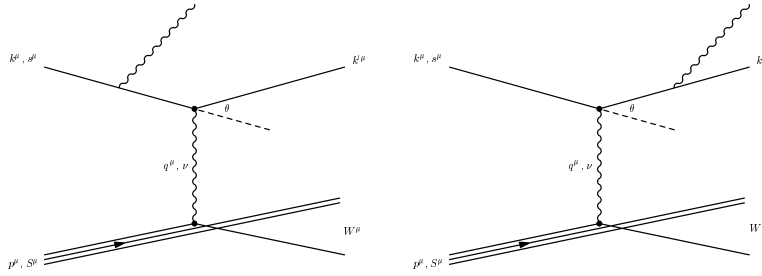


Figure 5.8: Examples of external processes that require radiative corrections.

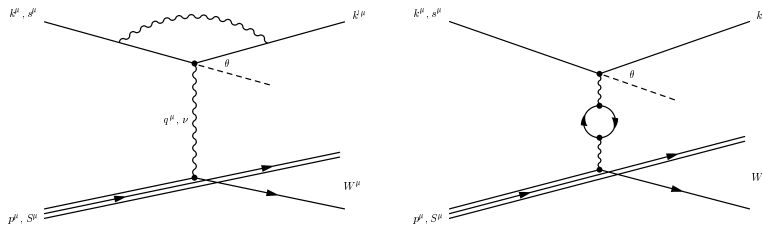


Figure 5.9: Examples of internal processes that require radiative corrections.

5.7 Structure Functions and Integrals

5.7.1 Determining the Final Structure Functions

This section will summarize the order of the steps taken to determine the spin structure functions from the measured asymmetry $(N_L - N_R)/(N_L + N_R)$ and the correction factors discussed in the previous sections of this chapter.

The analysis is performed on a run-by-run basis and begins with the application of the Electron Definition (Table 5.1) to the spectrometer and beam data to determine the raw counts N_L and N_R for each beam helicity state

$$A_{raw} = \frac{N_L - N_R}{N_L + N_R}. \quad (5.11)$$

This asymmetry is then corrected for rate dependence (Section 5.2.4) and electro-weak effects (Section 5.2.3)

$$A_{corr} = A_{raw} C_{rate} C_{weak} \quad (5.12)$$

The next step is to combine the asymmetries from multiple runs into overall asymmetries and structure functions for each spectrometer. Since each run is taken to be its own unique measurement with its own statistical error, this is done as follows

$$A_{spec} = \frac{\sum \frac{(A_{corr})_i}{\sigma_i^2}}{\sum \frac{1}{\sigma_i^2}} \quad (5.13)$$

where the sum is over all runs with valid data for the spectrometer under consideration. The error on each of these quantities is

$$\sigma_{A_{spec}} = \frac{1}{\sqrt{\sum \frac{1}{\sigma_i^2}}}. \quad (5.14)$$

The hadron (Section 5.2.1) and positron (Section 5.2.2) correction factors are next used to obtain a final counting asymmetry for each spectrometer

$$A_{no\ pions} = \frac{A_{spec} - n_{\pi} A_{\pi}}{1 - n_{\pi}} \quad (5.15)$$

$$A_{count} = \frac{A_{no\ pions} - n_{e^+} A_{e^+}}{1 - n_{e^+}}. \quad (5.16)$$

The target polarization (Chapter 4), beam polarization (Section 5.3), dilution factor (Section 5.4), target nuclear effects (Section 5.5), and radiative corrections

(Section 5.6) are then used to obtain

$$A_{\parallel} = \frac{A_{count}}{P_b P_t C_1 f f_{RC}} + A_{RC} \quad (5.17)$$

separately for each of the spectrometers.

A_{\parallel} can be put into Equation 2.7 to obtain the structure function $g_1^p(x, Q^2)$. For this analysis, $F_1(x, Q^2)$ is obtained from Equation 2.28 together with fits to $F_2(x, Q^2)$ from NMC [92] and to $R(x, Q^2)$ from 1998 [65].

5.7.2 Evolution to a Common Q^2

In order to calculate the sum rules discussed in Section 2.5, the data from all x bins must be evolved to a common Q^2 . This also facilitates comparison of the E155 data with that of other experiments. For the kinematic range of E155, a value of 5 GeV² was chosen as the common value, which will be denoted as Q_0^2 .

One method for accomplishing this evolution is to make the assertion that g_1/F_1 is Q^2 independent [7, 93, 94], a claim that will be discussed further below. In that method, the measured g_1 for each x bin is divided by F_1 evaluated at the same kinematics and then multiplied by $F_1(x, Q_0^2)$.

For this analysis, fits [91] to world g_1/F_1 data were performed to the proton, neutron, and deuteron data simultaneously using the equation

$$g_1/F_1 = x^\alpha(a + bx + cx^2)(1 + \beta/Q^2). \quad (5.18)$$

This is the same form as Equation 5.9, used in the fits to $A_1(x, Q^2)$ for the radiative corrections discussed in Section 5.6.

The final parameters from this fit are shown in Table 5.3. The value of g_1/F_1

Parameter	Proton	Neutron
α	0.700	-0.335
a	0.817	-0.013
b	1.014	-0.330
c	-1.489	0.761
β	-0.037	0.129

Table 5.3: Parameters from fit to g_1/F_1 .

evolved to Q_0^2 is then calculated with

$$\left(\frac{g_1}{F_1}\right)_{Q_0^2} = \left(\frac{g_1}{F_1}\right)_{measured} + [(\text{Fit})_{Q_0^2} - (\text{Fit})_{measured}] \quad (5.19)$$

Table 5.4 and Table 5.5 list g_1/F_1 and g_1 for each spectrometer at $Q^2 = 5 \text{ GeV}^2$, along with the measured values of Q^2 for each bin.

The assertion discussed above that g_1/F_1 should be Q^2 independent can be supported by considering the DGLAP[¶] equations for these functions, which express how they evolve with Q^2 due to gluon radiation. F_1 and g_1 have DGLAP equations that are similar in form, and to leading order are identical. As Figure 5.10 shows, the expectation of Q^2 independence in g_1/F_1 is supported by the data, although for the higher x bins a slight dependence can be seen at lower values of Q^2 .

In order to compare data at fixed x , as a function of Q^2 , from many experiments on an equal footing, a set of coarse bins is used to re-bin the data. The scheme, known as *world binning* is shown in Table 5.6.

Figure 5.10 shows the data from Tables 5.4 and 5.5, along with that from other experiments, plotted as a function of Q^2 for each of the world bins. The Q^2 dependence of g_1^p is evident. This may be compared to a similar plot of $2xF_1$, shown in Figure 2.3.

[¶]These equations, also known as the GLAP equations or the Altarelli-Parisi equations, are named for their authors: Dokshitzer, Gribov, Lipatov, Altarelli, and Parisi.

Spec.	Bin	$\langle x \rangle$	$\langle Q^2 \rangle$	$g_1/F_1 \pm \text{stat}$	$g_1 \pm \text{stat}$
2.75°	4	0.015	1.091	0.049 ± 0.021	0.524 ± 0.147
	5	0.017	1.203	0.061 ± 0.015	0.562 ± 0.100
	6	0.019	1.321	0.047 ± 0.015	0.429 ± 0.088
	7	0.022	1.448	0.046 ± 0.014	0.379 ± 0.078
	8	0.024	1.585	0.055 ± 0.014	0.390 ± 0.069
	9	0.027	1.732	0.065 ± 0.013	0.399 ± 0.062
	10	0.031	1.885	0.067 ± 0.014	0.368 ± 0.057
	11	0.035	2.044	0.083 ± 0.014	0.391 ± 0.052
	12	0.039	2.216	0.057 ± 0.014	0.264 ± 0.048
	13	0.044	2.396	0.101 ± 0.014	0.374 ± 0.044
	14	0.049	2.587	0.115 ± 0.015	0.374 ± 0.042
	15	0.056	2.776	0.112 ± 0.015	0.327 ± 0.040
	16	0.063	2.972	0.123 ± 0.017	0.319 ± 0.039
	17	0.071	3.171	0.140 ± 0.018	0.319 ± 0.037
	18	0.079	3.367	0.183 ± 0.019	0.364 ± 0.036
	19	0.089	3.573	0.143 ± 0.020	0.258 ± 0.034
	20	0.101	3.772	0.178 ± 0.022	0.281 ± 0.033
	21	0.113	3.970	0.124 ± 0.023	0.176 ± 0.032
	22	0.127	4.170	0.175 ± 0.025	0.218 ± 0.031
	23	0.144	4.361	0.249 ± 0.028	0.272 ± 0.030
	24	0.162	4.544	0.276 ± 0.031	0.266 ± 0.030
	25	0.182	4.716	0.254 ± 0.035	0.216 ± 0.029
	26	0.205	4.883	0.285 ± 0.039	0.212 ± 0.029
	27	0.230	5.038	0.332 ± 0.044	0.215 ± 0.029
	28	0.259	5.182	0.414 ± 0.050	0.231 ± 0.028
	29	0.292	5.332	0.392 ± 0.057	0.186 ± 0.027
	30	0.328	5.465	0.444 ± 0.065	0.176 ± 0.026
	31	0.370	5.575	0.386 ± 0.075	0.125 ± 0.024
	32	0.416	5.680	0.583 ± 0.088	0.149 ± 0.022
	33	0.468	5.783	0.627 ± 0.109	0.121 ± 0.020
	34	0.527	5.869	0.329 ± 0.138	0.048 ± 0.019
	35	0.593	5.944	0.501 ± 0.178	0.050 ± 0.016
	36	0.667	6.003	0.503 ± 0.228	0.032 ± 0.013
	37	0.751	6.062	0.691 ± 0.280	0.022 ± 0.008
	38	0.846	6.118	1.254 ± 0.432	0.013 ± 0.004

Table 5.4: g_1^p/F_1^p and g_1^p at $Q^2 = 5 \text{ GeV}^2$ for the 2.75° spectrometer.

Spec.	Bin	$\langle x \rangle$	$\langle Q^2 \rangle$	$g_1/F_1 \pm \text{stat}$	$g_1 \pm \text{stat}$
5.5°	15	0.057	4.005	0.234 ± 0.089	0.653 ± 0.241
	16	0.063	4.388	0.180 ± 0.040	0.455 ± 0.100
	17	0.071	4.829	0.132 ± 0.026	0.298 ± 0.058
	18	0.080	5.302	0.146 ± 0.020	0.292 ± 0.040
	19	0.090	5.799	0.159 ± 0.017	0.281 ± 0.031
	20	0.101	6.324	0.170 ± 0.015	0.266 ± 0.025
	21	0.113	6.868	0.167 ± 0.015	0.231 ± 0.022
	22	0.128	7.432	0.237 ± 0.015	0.292 ± 0.019
	23	0.144	8.017	0.241 ± 0.015	0.263 ± 0.017
	24	0.162	8.618	0.226 ± 0.016	0.216 ± 0.016
	25	0.182	9.232	0.260 ± 0.017	0.219 ± 0.015
	26	0.205	9.851	0.270 ± 0.018	0.200 ± 0.014
	27	0.230	10.477	0.360 ± 0.020	0.233 ± 0.013
	28	0.259	11.110	0.358 ± 0.022	0.199 ± 0.012
	29	0.292	11.728	0.412 ± 0.025	0.195 ± 0.011
	30	0.328	12.335	0.423 ± 0.027	0.168 ± 0.010
	31	0.370	12.937	0.511 ± 0.031	0.164 ± 0.009
	32	0.416	13.521	0.560 ± 0.035	0.141 ± 0.008
	33	0.468	14.083	0.467 ± 0.044	0.094 ± 0.007
	34	0.526	14.607	0.582 ± 0.057	0.082 ± 0.006
35	0.592	15.108	0.615 ± 0.078	0.060 ± 0.005	
36	0.666	15.578	0.560 ± 0.110	0.036 ± 0.004	
37	0.749	15.986	0.813 ± 0.163	0.023 ± 0.002	
38	0.843	16.341	0.736 ± 0.286	0.007 ± 0.001	
10.5°	22	0.130	10.042	0.359 ± 0.135	0.443 ± 0.174
	23	0.145	11.140	0.326 ± 0.054	0.357 ± 0.062
	24	0.162	12.354	0.271 ± 0.035	0.259 ± 0.035
	25	0.182	13.699	0.325 ± 0.027	0.275 ± 0.024
	26	0.205	15.134	0.326 ± 0.025	0.242 ± 0.019
	27	0.230	16.655	0.386 ± 0.026	0.249 ± 0.017
	28	0.259	18.276	0.364 ± 0.028	0.203 ± 0.015
	29	0.291	20.027	0.508 ± 0.032	0.239 ± 0.014
	30	0.328	21.862	0.502 ± 0.034	0.196 ± 0.012
	31	0.369	23.795	0.489 ± 0.038	0.158 ± 0.011
	32	0.413	25.851	0.442 ± 0.052	0.118 ± 0.011
	33	0.465	27.944	0.512 ± 0.090	0.103 ± 0.013
	34	0.524	30.117	0.410 ± 0.153	0.068 ± 0.014
	35	0.590	32.298	0.868 ± 0.232	0.074 ± 0.012
36	0.663	34.722	0.580 ± 0.405	0.038 ± 0.011	

Table 5.5: g_1^p/F_1^p and g_1^p at $Q^2 = 5 \text{ GeV}^2$ for the 5.5° & 10.5° spectrometers.

Bin	Min x	Center	Max x
1	0.010	0.015	0.020
2	0.020	0.025	0.030
3	0.030	0.035	0.040
4	0.040	0.050	0.060
5	0.060	0.080	0.100
6	0.100	0.125	0.150
7	0.150	0.175	0.200
8	0.200	0.250	0.300
9	0.300	0.350	0.400
10	0.400	0.500	0.600
11	0.600	0.750	0.900

Table 5.6: Definitions of world bins.

In both Figure 5.10 and Figure 5.11, the E155 data points represent the separate measurements of each of the up to three spectrometers measuring the bin.

5.7.3 Proton, Deuteron, and Neutron Functions for $0 \leq x \leq 1$

Although maintaining separate data for each spectrometer is useful for Q^2 dependence plots and for illuminating the kinematic coverage of the experiment, for investigation of integrals of g_1^p the data need to be combined. This was accomplished on a bin-by-bin basis by performing an average of the Q^2 -evolved structure functions, weighted by the statistical error, for all spectrometers returning data for that bin.

Some sum rules involve not just the proton spin structure function, but also that of the neutron. We may determine g_1^n from a combination of the measurements on the proton and deuteron:

$$g_1^n(x, Q^2) = \frac{2g_1^d(x, Q^2)}{1 - 1.5\omega_D} - g_1^p(x, Q^2) \quad (5.20)$$

where ω_D is the D -state probability of the deuteron. E155 deuteron data is from [14].

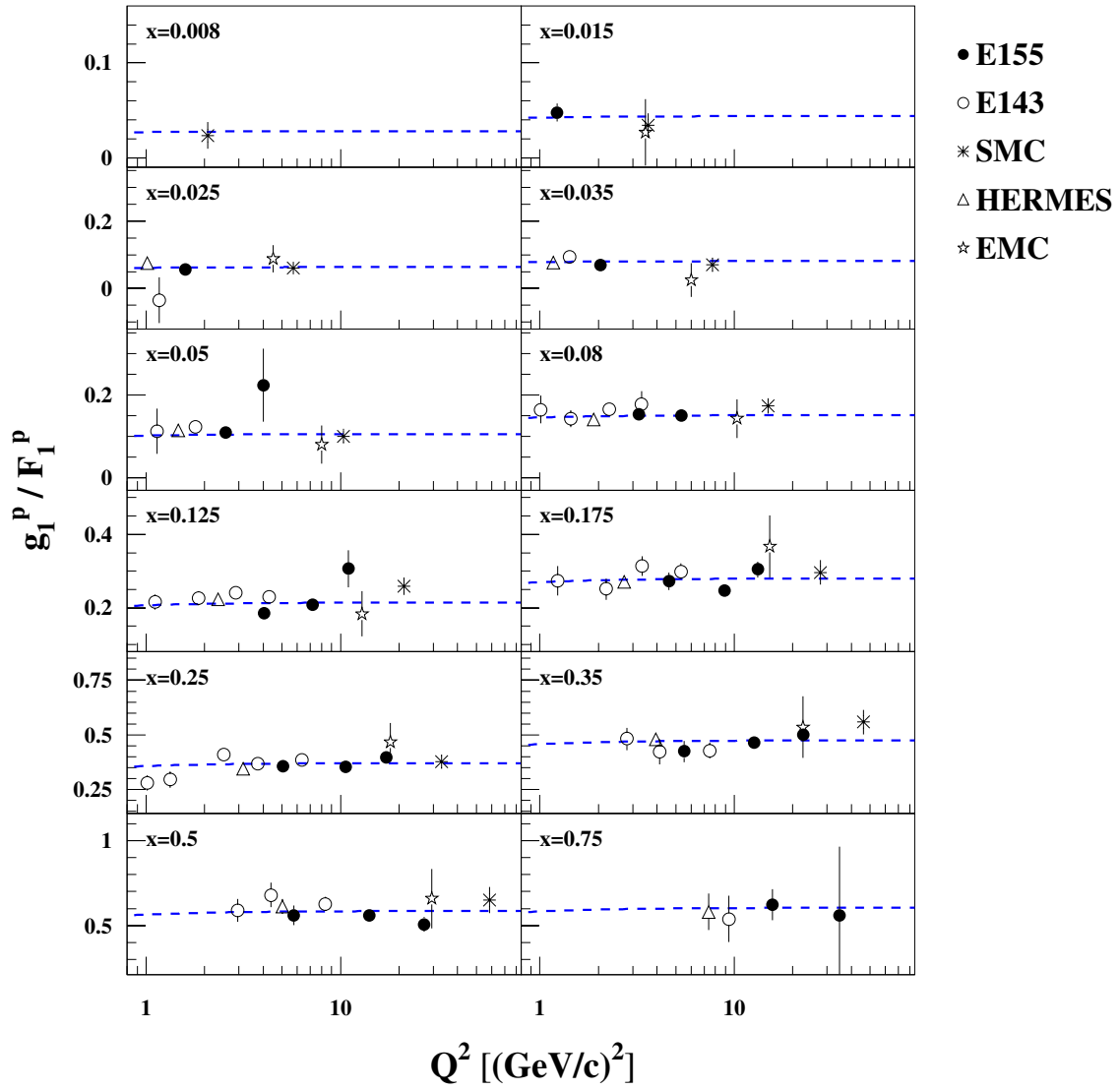


Figure 5.10: g_1^p / F_1^p plotted as a function of Q^2 for E155 and several other experiments. Dashed lines are the result of a NLO fit [95].

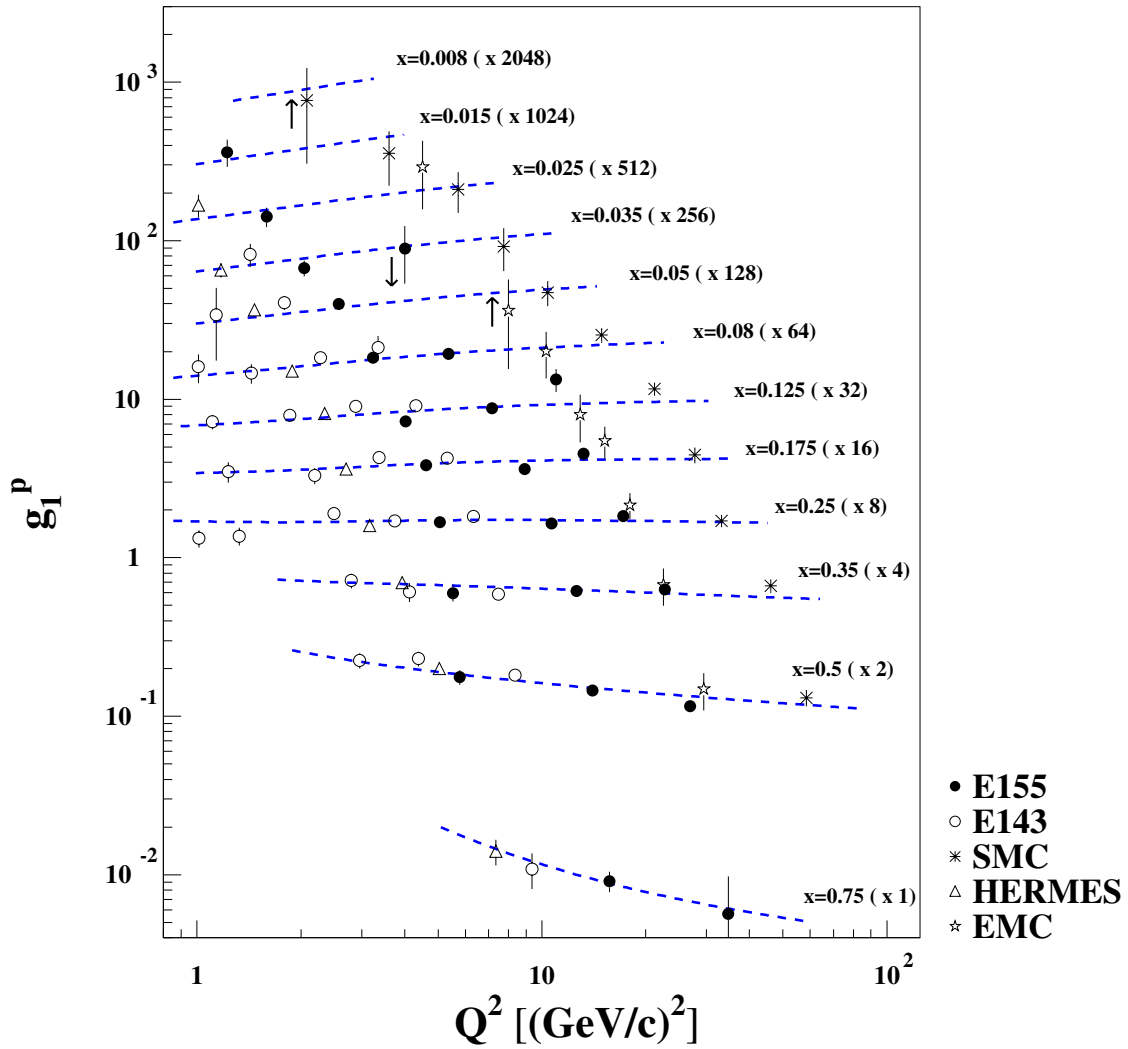


Figure 5.11: g_1^p plotted as a function of Q^2 for E155 and several other experiments.

With the data from the three spectrometers combined and with a neutron structure function extracted from the proton and deuteron functions, we may now compare g_1 versus x for E155 with data from other experiments. Figure 5.12 shows all three functions, plotted with all other relevant measurements. Visually, the log scale used in the x -axis tends to exaggerate the low x contribution of g_1 to integrals. To compensate for this effect, xg_1 is also plotted, in Figure 5.13.

The kinematics of E155 allowed measurement of g_1 over only a portion of the region from 0 to 1. The integrals of g_1^p and g_1^d over this measured region are

$$\int_{0.014}^{0.9} g_1^p dx = 0.118 \pm 0.001 \pm 0.010 \quad (5.21)$$

$$\int_{0.014}^{0.9} g_1^d dx = 0.044 \pm 0.002 \pm 0.003, \quad (5.22)$$

with the first error statistical and the second systematic.

For testing sum rules we need to perform the integral over the entire region from 0 to 1, so we must extrapolate g_1 in the regions in which it was not measured.

For the low x extrapolation ($0 \leq x \leq 0.014$), an NLO analysis of world plus E155 data [95] was used. This method fits all available g_1 data simultaneously to a model based on next-to-leading order perturbative QCD. The method [10, 41] is that used in E154, with updated unpolarized parton distributions from phenomenological fits to world data (the ‘‘GRV98’’ distributions) [96, 97]. The integrals for the low- x region from these NLO fits are

$$\int_0^{0.014} g_1^p dx = -0.006 \pm 0.004 \pm 0.002 \pm 0.009 \quad (5.23)$$

$$\int_0^{0.014} g_1^d dx = -0.014 \pm 0.004 \pm 0.002 \pm 0.005, \quad (5.24)$$

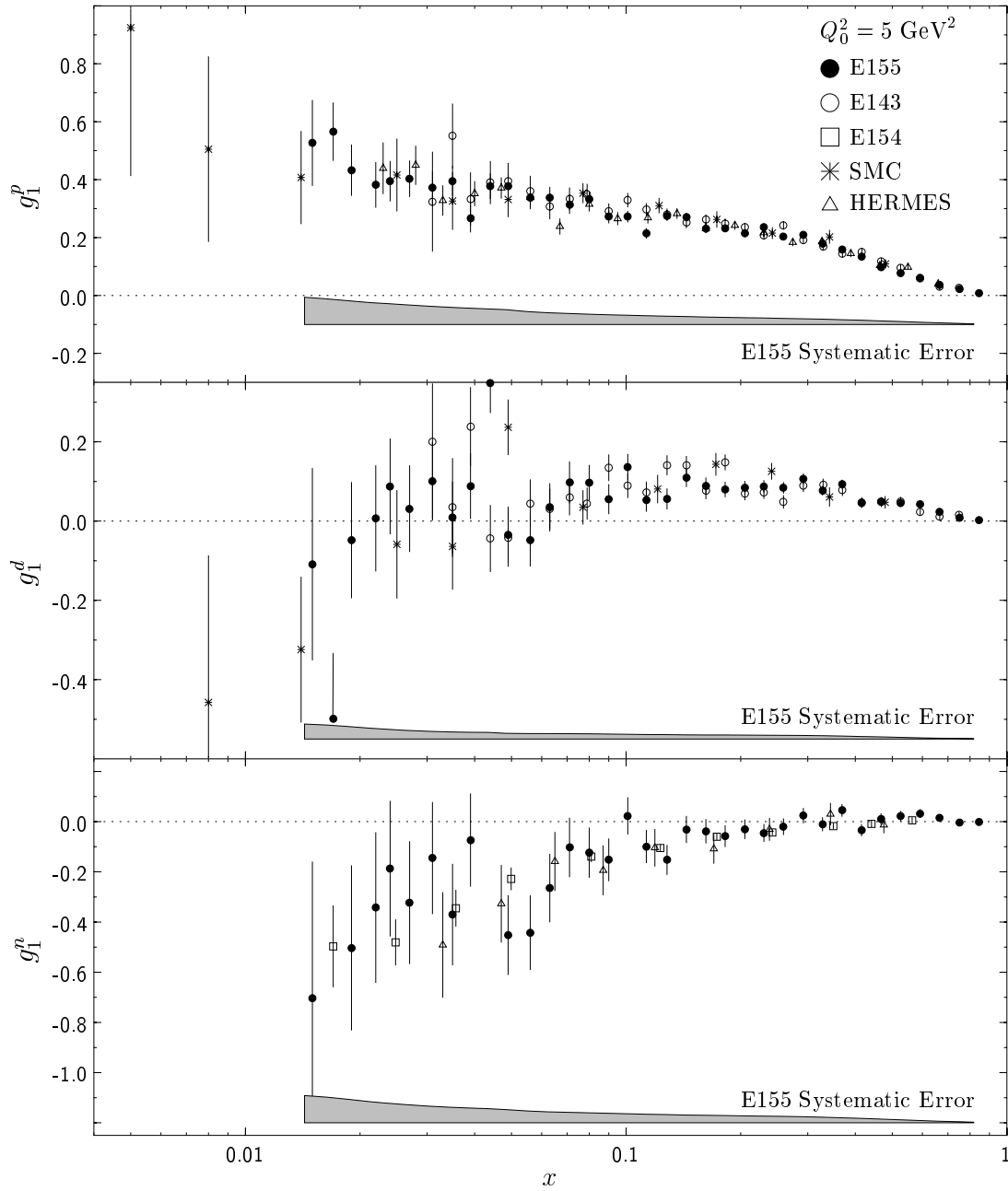


Figure 5.12: E155 g_1^p for proton, deuteron, and neutron. Deuteron data is from [14].

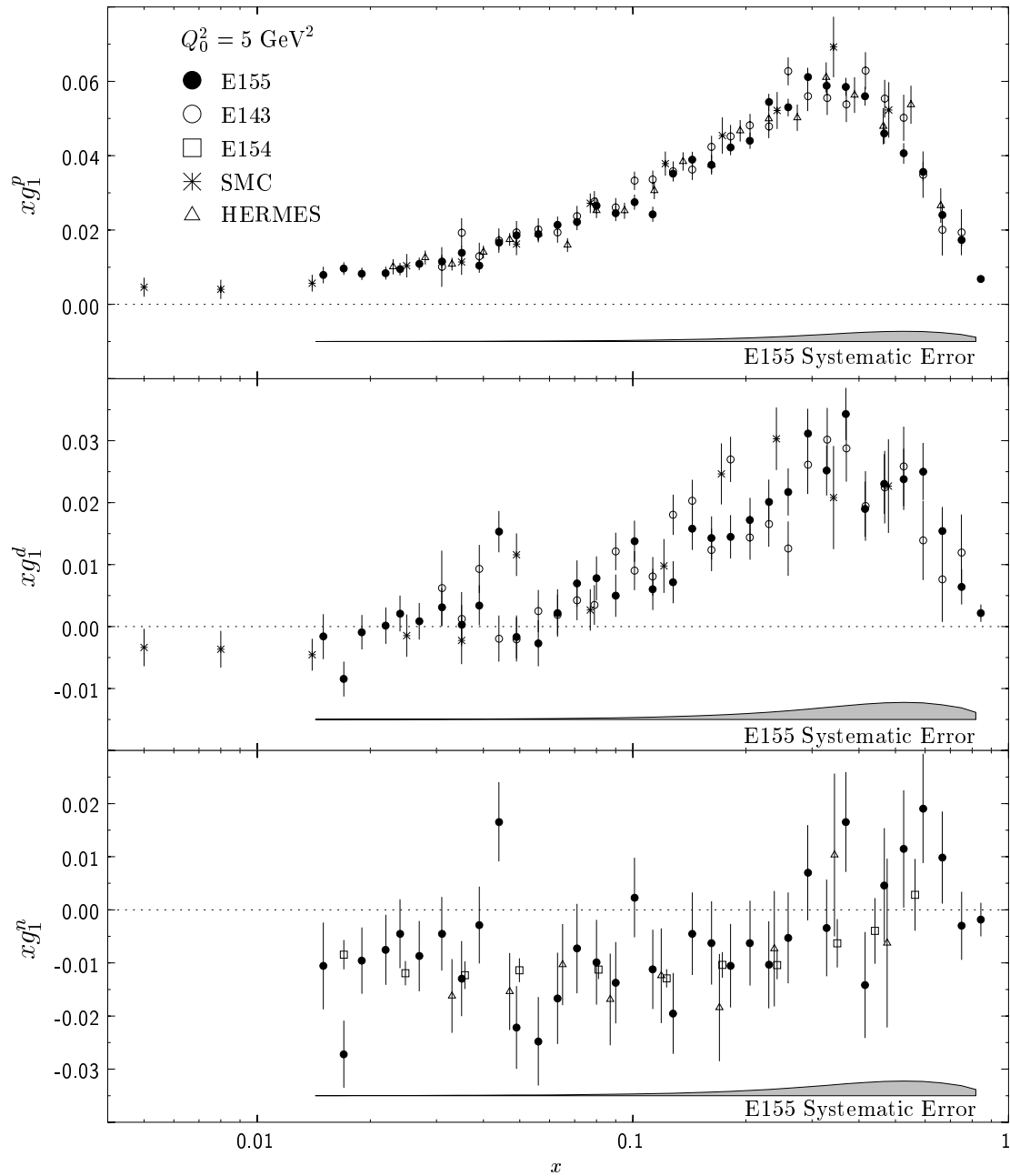


Figure 5.13: E155 xg_1 for proton, deuteron, and neutron.

with the first error statistical, the second systematic, and the third due to evolution errors in g_1 .

For the high- x region, a parameterization of g_1 is used. The function

$$g_1(x) = \alpha(1 - x)^3 \quad (5.25)$$

is fit to the highest four data points. The integral of Equation 5.25 is then used for the high- x extrapolation. For g_1^p the fit gave $\alpha = 1.01453$ and an integral over $[.9, 1]$ of -0.0000253 . For g_1^d the fit gave $\alpha = 0.61517$, which results in an integral over $[0.9, 1]$ of -0.0000153 . The extrapolation in the high- x region is therefore taken to be

$$\int_{0.9}^1 g_1^p dx = 0.000 \pm 0.000 \pm 0.000 \quad (5.26)$$

$$\int_{0.9}^1 g_1^d dx = 0.000 \pm 0.000 \pm 0.000. \quad (5.27)$$

5.7.4 Sum Rules

With values for the integral of g_1 in the low x , high x , and measured regions, it is now possible to examine the agreement of E155 with the sum rules mentioned in Section 2.5.

Combining the three regions covered by the integrals in the previous section, we have

$$\Gamma_1^p \equiv \int_0^1 g_1^p dx = +0.112 \pm 0.005 \pm 0.010 \pm 0.009 \quad (5.28)$$

$$\Gamma_1^d \equiv \int_0^1 g_1^d dx = +0.030 \pm 0.005 \pm 0.004 \pm 0.005 \quad (5.29)$$

$$\Gamma_1^n \equiv \int_0^1 g_1^n dx = -0.062 \pm 0.012 \pm 0.013 \quad (5.30)$$

The value of Γ_1^p can be compared to the prediction of the Ellis-Jaffe sum rule. With current data on F , D [23], their prediction gives 0.163 ± 0.004 . The E155 value, $+0.112 \pm 0.014$ differs from this prediction by over 12σ . Similarly, the Ellis-Jaffe prediction for Γ_1^n of -0.019 ± 0.004 , compared to the E155 measurement of $-0.062 \pm 0.012 \pm 0.013$ represents a more than 12σ violation. The E155 result should be compared with the E143 result [16] of $\Gamma_1^p(Q_0^2=5) = 0.129 \pm 0.010$ and with the SMC result [98] of $\Gamma_1^p(Q_0^2=5) = 0.132 \pm 0.017$. Together, these results help confirm the conclusion that the assumptions of an unpolarized strange sea and no gluon contribution oversimplify the issue of the nucleon spin.

For the Bjorken sum rule, $\Gamma_1^p - \Gamma_1^n$ is examined. At 5 GeV^2 , the theoretical prediction is 0.182 ± 0.005 . From the above values, E155 measures 0.174 ± 0.014 , in agreement not only with the prediction, but also with other spin structure experiments. Figure 5.14 shows the E155 data in relation to the theoretical predictions.

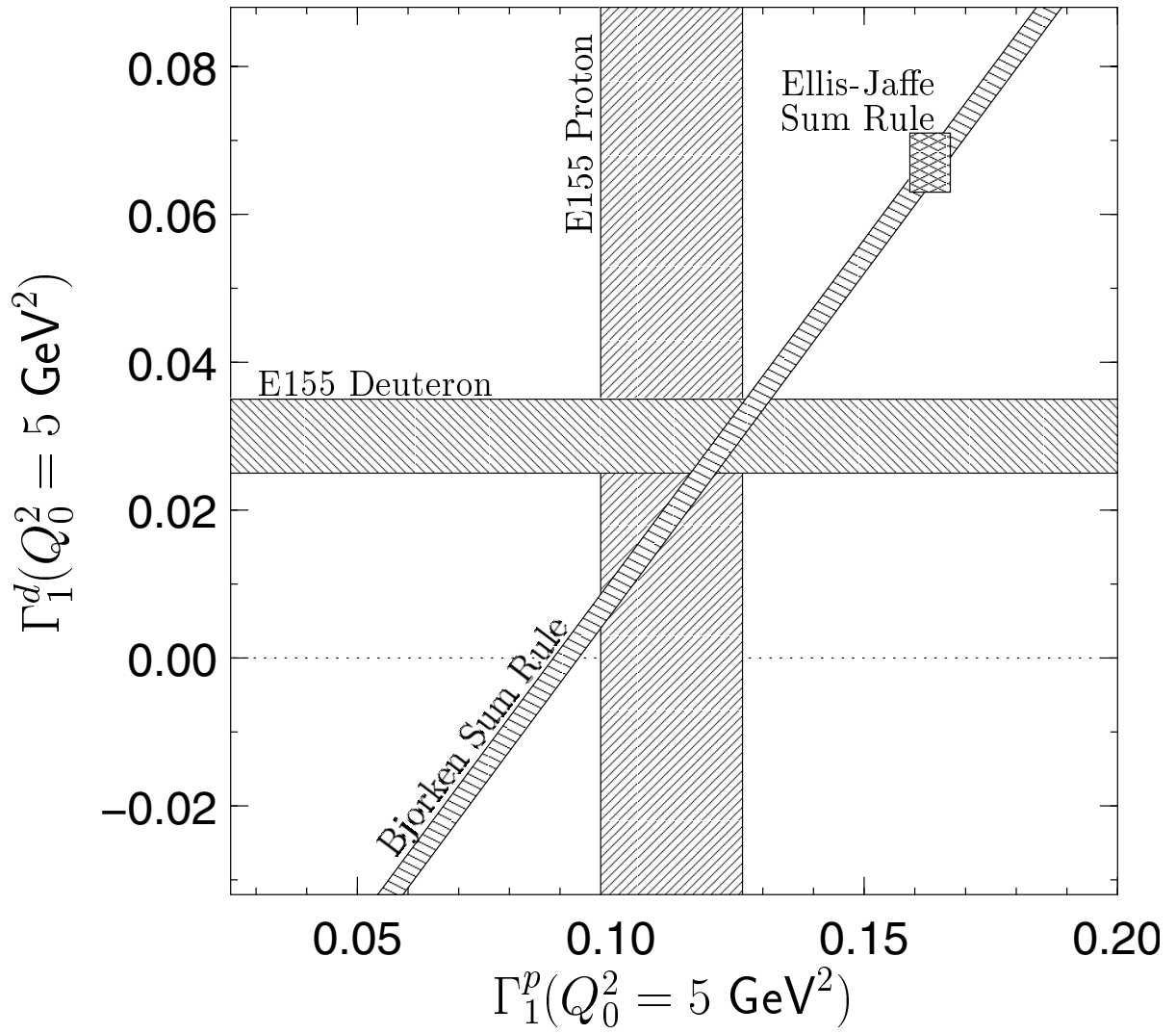


Figure 5.14: E155 integrals and sum rule predictions.

Chapter 6

Conclusions

Since the surprising discovery by the EMC experiment at CERN in 1987 that the quark contribution to the nucleon spin differs significantly from what the expectations were at the time, the subject has flourished. The 1990's saw tremendous interest in the field of spin physics, witnessed by the quantity and variety of experiments conducted at the world's major accelerators. The HERMES experiment at DESY uses a polarized electron storage ring and a fixed, internal polarized gas target (of H, D, or ^3He) and has been running since 1996. The SMC experiment at CERN used a polarized muon beam and a fixed polarized solid target (of butanol, deuterated butanol, and $^{14}\text{NH}_3$) and ran from 1992 to 1996. Finally, a series of five experiments at SLAC, culminating in E155 and its extension, E155x, have run from 1993 to 1999 and used a polarized electron beam and either polarized solid targets (of $^{15}\text{NH}_3$, $^{15}\text{ND}_3$, and ^6LiD) or gaseous targets (of ^3He).

The kinematic regions observed differ among each of the experiments, as do the statistical accuracy of the measurements. All experiments to date confirm the EMC findings of violation of the Ellis-Jaffe sum rule. Further, each experiment's results for the structure function $g_1(x, Q^2)$ are consistent, and, for experiments that measured

both g_1^p and either g_1^n or g_1^d , the integrals of g_1^p and g_1^n of each experiment combine to validate the fundamental Bjorken sum rule.

As one of these spin physics experiments, the successes of E155 are numerous. The statistical accuracy achieved on g_1 is unparalleled, and the coverage in x is large enough to permit comparison with all other experiments. E155 successfully used ${}^6\text{LiD}$ as a source of polarized deuterons, the first use of this material in an intense beam of any type. Although the running time on g_2 was limited in E155, the E155x extension significantly increased the precision of this quantity over all previous measurements. Finally, despite a flaw in the measurement of the proton polarization due to the design of the target holder, careful analysis, reported in this work for the first time, has recovered this crucial part of the E155 data set.

The above experiments could be said to constitute the first chapter in the study of nucleon spin. Today, the world seems poised for the next chapter, with plans for new experiments and measurements of new quantities being made at all the major labs. At DESY, HERMES will begin its second run in 2001 with a measurement of the quark transversity function $h_1(x, Q^2)$, an analogue to $g_1(x, Q^2)$ built from transverse instead of longitudinal parton distribution functions [99]. Two experiments at RHIC, the STAR [100] and PHENIX [101] detectors, seek to measure the polarized gluon distribution function ΔG and individual parton distribution functions (Δu , $\Delta \bar{u}$, Δd , $\Delta \bar{d}$) through Drell-Yan processes and through W^\pm and Z^0 production asymmetries. At CERN, the COMPASS [102] experiment will also measure ΔG through charm lepton production using a muon beam and a target and detector similar to those used in the SMC [2] experiment. Finally, a proposal [103] has been made to SLAC for an experiment, E156, to measure ΔG through open charm photoproduction.

Each of these experiments promises to stretch the limits of beam, detector, and computing technology, as well as advance the physics frontiers in this rich field. Fi-

nally, in the distance are yet-unconceived experiments offering information on the orbital angular momentum degrees of freedom in the nucleon. Indeed, the study of nucleon spin seems to offer limitless potential for interesting physics.

Appendix A

NMR Correction Based on ^{15}N Polarization

After the conclusion of the scheduled E155 running, a much more thorough investigation of the problem began. This period of target measurements and calibrations became known as the Technical Run. A measurement made during the Technical Run suggested that the problems encountered with the NMR system only appeared at the frequency used to measure the proton polarization – 213 MHz, and not at lower frequencies used to measure ^{15}N and deuteron polarizations. The test involved setting the target magnet at half its normal field, such that the Larmor frequency of the protons was reduced from 213 MHz to 106.5 MHz. The lower field also meant that the Larmor frequency of the electrons was lower by a factor of two. Thus we had to install a microwave tube that had a peak power centered in the 70 GHz range instead of the 140 GHz unit used during production running at 5 T.

Comparison of the NMR lineshape of the enhanced proton signal at 106.5 MHz with a similar one taken at the normal 213 MHz shows that at lower frequencies the anomalous features disappear, as can be seen in Figure A.1, copied from Figure 4.11.

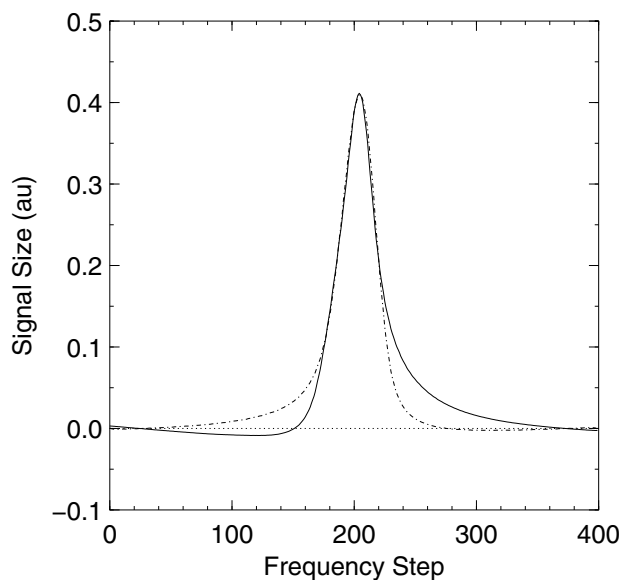


Figure A.1: Comparison of NMR signals of $^{15}\text{NH}_3$ at 2.5 T/106.5 MHz (dashed line) and 5 T/213 MHz (solid line). The 213 MHz signal, representing a polarization of about 94%, was scaled by an overall factor of -280 in order to aid comparison with the 106.5 MHz signal, which represents a polarization of only 23%. Despite the appearance, one signal is not flipped about the y -axis relative to the other.

The 213 MHz signal has been inverted and rescaled to aid comparison, and it can be clearly seen that the distortions in this signal are not present in the 106.5 MHz signal. $^{15}\text{NH}_3$ is known not to polarize as highly or as quickly at 2.5 T as at 5 T [56]. The polarization of the 106.5 MHz signal is 23%, compared to 94% for the 213 MHz signal.

As discussed in Section 4.3.3, there are several spin species present in the target material. Each comes from a specific substance in the material, and each has a unique magnetic moment and therefore a unique Larmor frequency. In $^{15}\text{NH}_3$, the proton has the highest Larmor frequency, and ^{15}N has the lowest. Since there is a connection between the polarizations of the protons and of ^{15}N , a method was devised whereby knowledge of one species would be used to imply the polarization of the other.

The magnetic moment of ^{15}N is one tenth the size of the proton's, which makes

an accurate measurement of its NMR signal more difficult than the proton. Several attempts were made during E155 running to tune a Q Meter to measure this signal, but due to its small size, the general difficulty in working with the NMR mentioned above, and the consequence that time spent on the NMR system during the experiment precluded taking asymmetry data, an accurate measurement of the ^{15}N polarization in beam was not made.

During the Technical Run the loss of data was not a factor, and the system was tuned and measurements of ^{15}N polarization were made along with that of the other spin species. By comparing the ^{15}N polarizations and the proton polarizations, it was seen that the proton to ^{15}N relation described by Equation 4.17 was not reproduced, because the ^{15}N measurements seemed unaffected (as would be expected due to their relatively low Larmor frequency) while the proton measurements suffered from the maladies mentioned in Section 4.4.

This suggested the following method of correcting the data. The first part of the correction is based on the measured proton- ^{15}N relationship from the technical run data, while the second part of the correction is based upon the fit from Equation 4.17. The two parts of the correction will now be referred to as the “measured relation” and the “expected relation” between the proton and the ^{15}N polarizations.

The combination of these two relations into a correction is rather natural. One relation gives the proton polarization actually measured for a given ^{15}N polarization, while the other gives the proton polarization expected from a given ^{15}N polarization. Thus the correction, i.e., the value to be added to or subtracted from the measured proton value, is made simply by the difference between the two relations.

While finding an expression for the expected relation is easy – one needs only to write down Equation 4.17 – the expression for the measured relation depends on the quantity and kind of data taken. Ideally, measurements would be taken on each of the

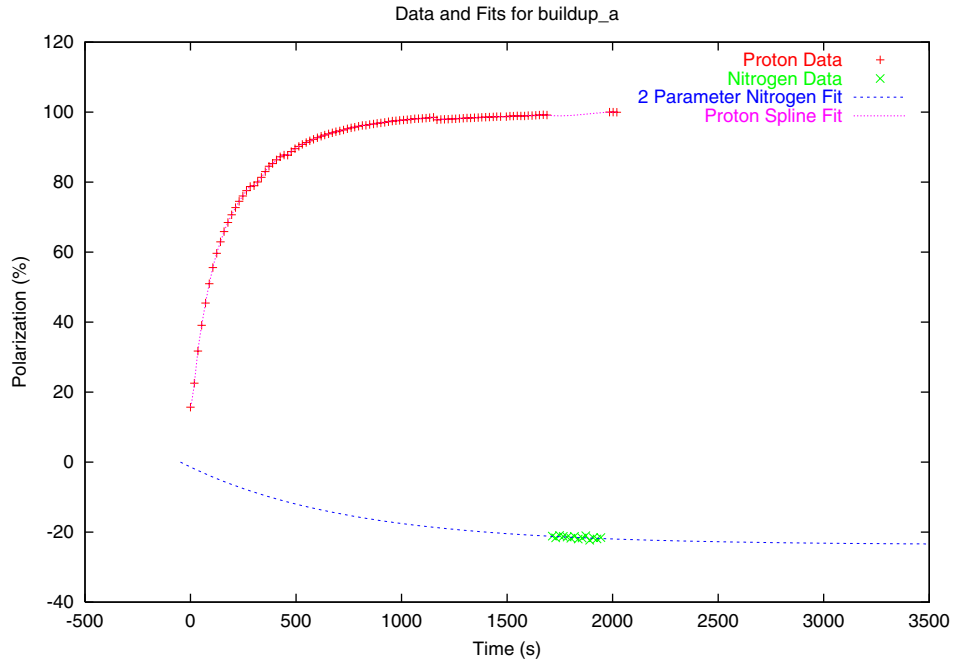


Figure A.2: Polarization buildup measuring proton and ^{15}N polarization. Note the difference in number of proton points to ^{15}N points.

species at regular intervals. Unfortunately, this correction method was not envisioned during the Technical Run, and so the data sets tend to consist of many measurements of one species as its polarization builds up, and then a few measurements of the other species once the buildup has reached its maximum. The result is that one species has significantly fewer measurements than the other, and thus fitting techniques have to be used to try to supply the missing data. Figure A.2 shows an example of a typical data set. Approximately ten such data sets were taken during the Technical Run.

The fit was accomplished by matching the existing data with an exponential buildup equation. The expression fitted was

$$P(t) = c_1(1 - e^{c_2 t - c_3}) \quad (\text{A.1})$$

where c_1 controls the maximum polarization obtained, c_2 controls the rate of polar-

ization buildup, and c_3 adjusts for the clock time at which the buildup was begun.

The actual method of the fit involved several steps. First, Equation A.1 was fit to the species with the most data, using c_1 , c_2 , and c_3 as independent parameters. The purpose of this fit is only to determine the value of c_3 , the time at which the polarization buildup was started*. Second, Equation A.1 was fit to the species with less data (usually ^{15}N), with c_1 and c_2 as independent parameters, and using the value of c_3 , determined above, as a fixed parameter. This resulted in a curve representing what the polarization was for the species with less data. This curve crosses the x -axis at exactly the same point as the curve for the species with more data.

A complication arises from the fact that the NMR system can only measure the polarization of one species at a time. Thus what is desired, pairs of values reflecting the proton and ^{15}N polarization at the same point in time, is not possible. Such pairs thus had to be constructed. For each time that the species with more data was measured, the value obtained was paired with the value of the fit equation, determined above, for that same time. For each time that the species with less data was measured, the value obtained was paired with the value from a spline fit to the data of the species with more measurements. A spline was used instead of an exponential buildup because what was desired was a smooth interpolation between existing points. A spline provided this, whereas Equation A.1 instead forced an assumption that the data changed in a specific way. The spline fit to the proton data and the fit of Equation A.1 to the ^{15}N data are also shown in Figure A.2.

The result of the above steps is a relation between proton and ^{15}N polarizations. This can then be combined with Equation 4.17 to create a correction curve. Unfortunately, as can be seen in Figure A.3, the resulting corrections are implausible as

*The target data acquisition system stores time as the number of seconds since January 1, 1900. The value of c_3 is therefore which second in 1997 the buildup in question was started.

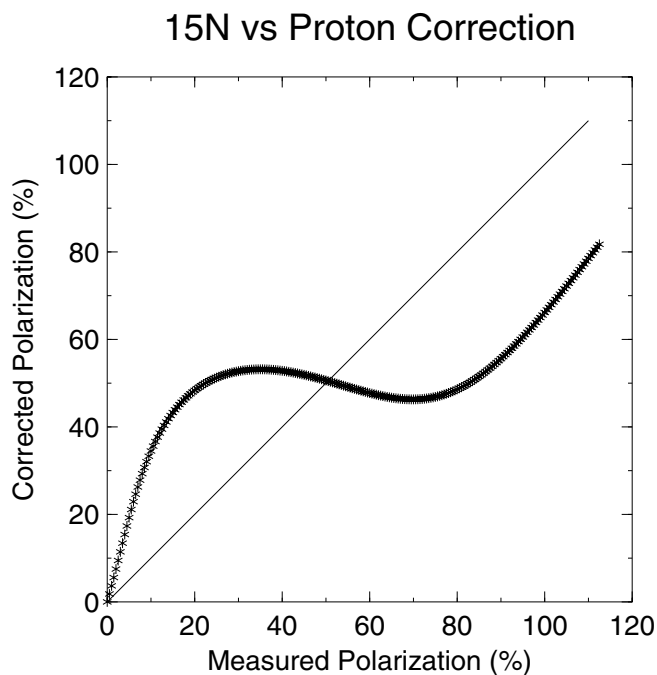


Figure A.3: Correction from measured values and Equation 4.17.

they are quite harsh (90% measured polarization maps to 55% corrected polarization), multi-valued (measured polarizations of 82%, 55%, and 20% all map to 45% corrected polarization), have a behavior that is not suggested by the processes involved, and do not result in asymmetry measurements that are independent of polarization.

Further investigation indicated that the problem may be occurring at a more fundamental level. By examining the quality of the fit used for Polysubtraction (described in Section 4.3.1), it can be seen that the anomalies in the NMR lineshape do not allow a good parabolic fit to the signal wings. This, in turn, directly affects the measured area of the NMR signal. Figure A.4 shows an example of this fitting error.

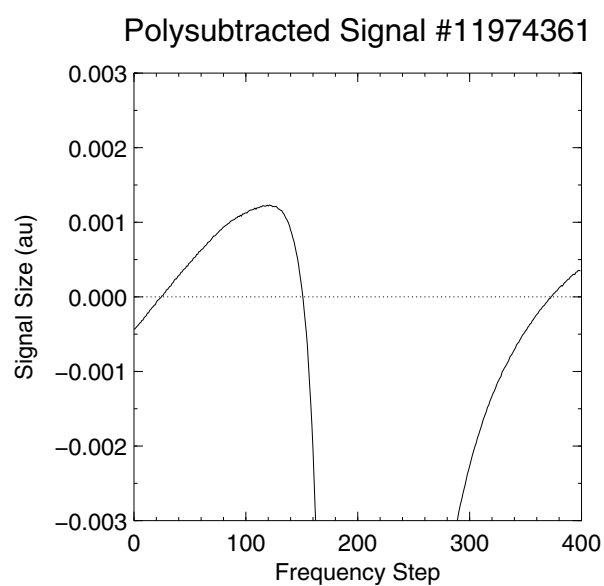


Figure A.4: Example of NMR signal anomalies interfering with residual background fit in signal wings. Ideally, the fit should be a flat line of zero height from channels 0 to 100 and 300 to 400.

Appendix B

NMR Correction Based on Lineshape Fitting

The anomalies that caused the ^{15}N correction method to fail are believed to be caused in part by a mixing of the absorptive and dispersive components of the target material's magnetic susceptibility in the measured NMR signal. The E155 target NMR system is designed to measure only the absorptive component of the magnetic susceptibility. This is a common feature of such systems [104], and the process of tuning the system ensures that this is the case.

A normal absorptive signal [105] from a proton NMR measurement resembles a Lorentzian function*. The corresponding dispersive signal resembles the derivative of such a function (see Figure B.1). Examination of typical E155 NMR signals indicates that both are present to some degree. Figure B.2 shows a sample E155 proton NMR signal.

Presence of a dispersive component in the NMR signal is problematic for several

*There are actually two closely-spaced peaks of slightly different height in $^{15}\text{NH}_3$. The difference in heights of these two peaks changes as the polarization of the sample changes. Thus the signal is not purely Lorentzian, but rather is somewhat asymmetric.

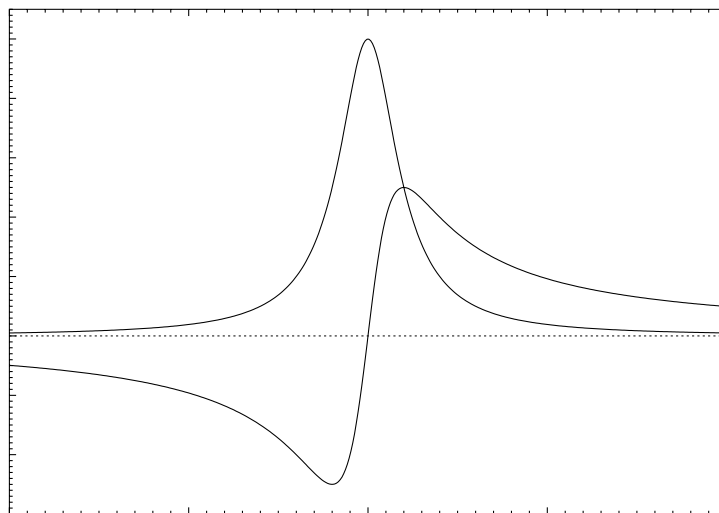


Figure B.1: Ideal absorptive and dispersive NMR signals.

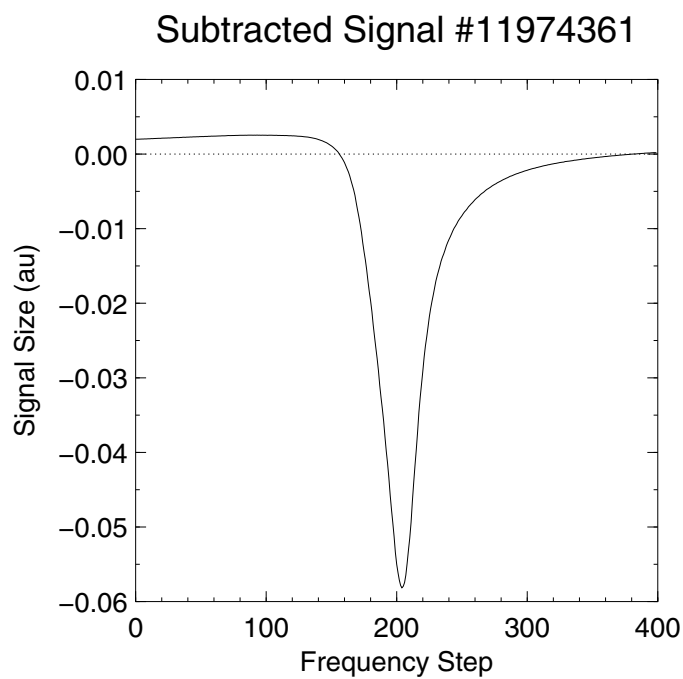


Figure B.2: Sample E155 proton NMR signal. The baseline signal has been subtracted as discussed in Section 4.3.1.

reasons. First, the NMR system is designed to avoid measuring it, and thus its appearance indicates that the system is not functioning normally. Second, the signal area, and thus polarization, is determined by integrating the NMR signal. If a dispersive component is present in that signal, the measured area will be skewed unless the region of integration happens to be symmetric about the zero crossing of the dispersive component. There is no guarantee that this will be the case. Finally, the presence of the dispersive component inhibits the proper fitting of the signal wings, since they no longer consist of only residual background from the electronics, but now also contain the dispersive component, which, unlike the absorptive signal, is not negligible in the wings. Clearly, a new method of determining the signal area is required since the usual Polysubtraction method does not work in this situation.

With the aim of correcting the measurements, an equation was developed to model the components present in the NMR signal, including the residual background from the electronics, the absorptive part of the susceptibility from which the polarization may be determined, and the dispersive part apparent in Figure B.2. An explanation of the path taken to arrive upon this equation follows.

The presence of magnetic moments in the target material causes the magnetic susceptibility of the material to be a complex function of frequency:

$$\chi(\omega) = \chi_R(\omega) + i\chi_I(\omega). \quad (\text{B.1})$$

The inductance of the NMR coil varies due to the susceptibility as

$$L(\omega) = L_0(1 + 4\pi\eta\chi(\omega)) \quad (\text{B.2})$$

where L_0 is the frequency independent part of the inductance, and η is known as the

filling factor, which represents the coupling between the field in the NMR coil and the nuclei of the material.

The heart of the Q Meter is a series RCL circuit which measures the impedance of the NMR coil (the inductor). This impedance depends on the inductance as $i\omega L$, or

$$Z(\omega) = \underbrace{-4\pi\omega\eta\chi_I}_{Z_R} + i \underbrace{(\omega L_0 + 4\pi\omega\eta\chi_R)}_{Z_I} \quad (\text{B.3})$$

The Q Meter is designed to return only the real part of this impedance – a quantity that may be integrated to obtain the polarization. The assumption made in this technique is that the problems experienced with the NMR were the result of a mixing of the real and imaginary parts of this impedance, equivalent to a rotation of the real and imaginary axes. Thus what was really measured was an impedance $Z'(\omega)$, related to $Z(\omega)$ by

$$\begin{aligned} Z'(\omega) &= e^{i\theta} Z(\omega) \\ &= \underbrace{-(4\pi\omega\eta\chi_I \sin\theta + (\omega L_0 + 4\pi\omega\eta\chi_R) \cos\theta)}_{Z'_R} + i \underbrace{(\sin\theta Z_I + \cos\theta Z_R)}_{Z'_I} \end{aligned} \quad (\text{B.4})$$

where θ is the amount of rotation.

From Equation B.4 it is clear that the dispersive part of the susceptibility (χ_R) appears in the measurement. It is the expression for Z'_R that forms the foundation of the equation used to fit the lineshapes. Since the Q Meter returns a voltage proportional to the real part of the impedance, Z'_R is put directly into the fit equation. The form of the fit equation is therefore

$$V(\omega) = \text{residual background} + c\chi_I\omega \sin\theta + c'\chi_R\omega \cos\theta \quad (\text{B.5})$$

The transmission cable used to connect the NMR coil to the Q Meter gives rise to a frequency dependent response in the electronic circuit that is present independent of the presence of a polarization signal. This background signal is usually referred to as the baseline. Normal operating procedures include a periodic measurement of this background so that it may be removed from the NMR signal before the polarization is calculated. Due to slow drifts in the electronic components, this background changes over time. The result is that after baseline subtraction, there is still some residue in the signal due to this drift. This residue – usually referred to as residual background – is characterized very well by a quadratic polynomial.

For the susceptibility, standard Lorentzian forms [105] are used for the two components:

$$\chi_I(\omega) = \frac{1}{2}\chi_0\omega_0 T_2 \frac{1}{1 + (\omega_0 - \omega)^2 T_2^2} \quad (\text{B.6})$$

$$\chi_R(\omega) = T_2(\omega_0 - \omega)\chi_I(\omega). \quad (\text{B.7})$$

where χ_0 is the frequency-independent susceptibility which influences the height of the signal, T_2 is a spin-spin relaxation time which influences the width of the signal, and ω_0 is the resonant (Larmor) frequency of the spin species being measured.

The fit equation is therefore

$$V(\omega) = c_0 + c_1\omega + c_2\omega^2 + \chi_I(\omega) \sin \theta + \chi_R(\omega) \cos \theta \quad (\text{B.8})$$

There are seven free parameters in this equation: c_0 , c_1 , c_2 , ω_0 , θ , χ_0 , and T_2 . It may be noted that the ωL_0 term of Equation B.4 has been dropped. The value of L_0 is folded into the parameter c_1 since it also enters as linear with respect to ω . In this way, an eighth parameter is avoided.

The technique for determining the polarization with this method is first to perform a fit of Equation B.8 to the NMR signal. The values returned for χ_0 , ω_0 , and T_2 are then plugged into the expression for $\chi_I(\omega)$ (Equation B.7), and integrated over the region in ω covered by the NMR sweep. In this way, the integration of the absorptive part of the susceptibility may be accomplished, even though the NMR system is returning more than just this quantity.

The result of fitting a typical signal is shown in Figure B.3. In general the NMR lineshape is matched rather well. Three regions can be identified in which the fit is not optimal. These regions are common to the majority of signals analyzed. First, the peak of the fit overshoots the data by a small amount. Second, the right knee of the fit is higher than the knee of the data. Finally, the fit winds up lower than the data at the extreme right, due to a slight mismatch between the slope of the fit and of the data in the right wing of the signal.

The results of using this technique to form a polarization correction are shown in Figure B.4. The x -axis shows the polarization measured online during running of E155, while the y -axis shows the new polarization calculated after applying this technique both to the signals of the Thermal Equilibrium calibration, and to the signals taken once the polarization was enhanced. Since there are over 100,000 proton signals from E155, a subset was constructed for use in plots by taking every 100th signal, and then from those throwing out ones that did not occur during a production run or that did not pass a series of cuts for target position and material type. The result is a smaller, more easily plotted data set that still retains all of the target loads and anneal cycles that occurred during the experiment.

As can be seen from Figure B.4, this signal-fitting technique results in polarizations that are larger than the original values. This result is counter to what one would expect, and also counter to some fundamental requirements such as that the absolute

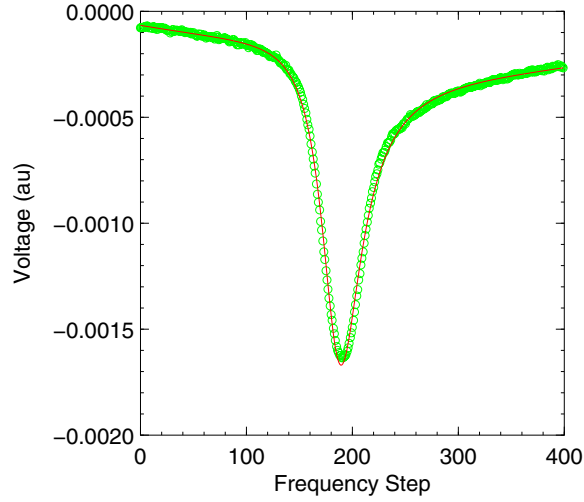


Figure B.3: Fit of Equation B.8 to a typical E155 NMR signal.

value of the polarization be below 100% and that the largest positive polarization and the largest negative polarization should be fairly close in value.

In an attempt to improve the results of the method, over 20 variations and refinements to this method were tested and plots similar to Figure B.4 made. Remarkably, there was little variation from the basic form of Figure B.4: the polarization of most of the points were increased, with several of the stripes (which represent target anneals or new material loads) extending to greater than 100% polarization. Further, examination of the effect this correction method has on the scattering asymmetries shows that it greatly increases the polarization dependence of the asymmetries, a dependence that should not exist.

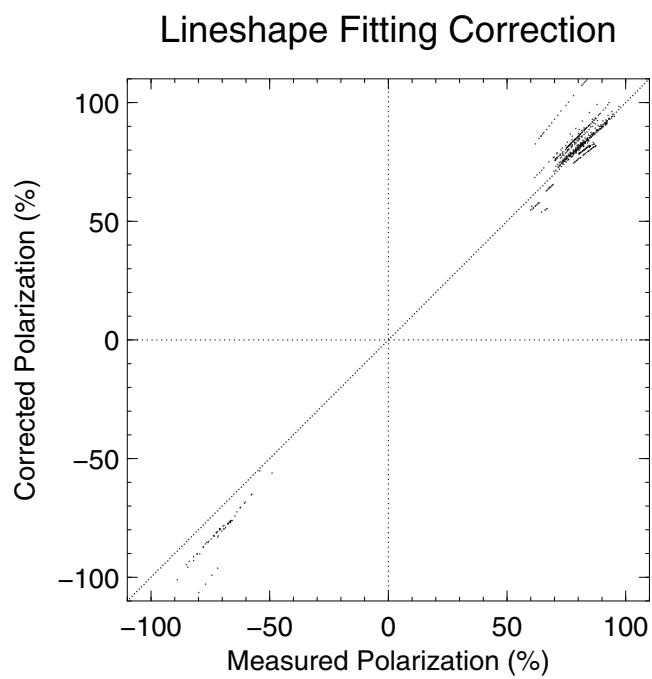


Figure B.4: Correction curve generated by fitting NMR signals to Equation B.8.

References

- [1] EMC Collaboration. *Phys. Lett.*, **B206**, 364 (1988).
- [2] SMC Collaboration. *Phys. Lett.*, **B396**, 338 (1997).
- [3] SMC Collaboration. *Phys. Lett.*, **B412**, 414 (1997).
- [4] HERMES Collaboration. *Phys. Lett.*, **B404**, 383 (1997).
- [5] E142 Collaboration. *Phys. Rev. Lett.*, **71**, 959 (1993).
- [6] E142 Collaboration. *Phys. Rev.*, **D54**, 6620 (1996).
- [7] E143 Collaboration. *Phys. Lett.*, **75**, 25 (1995).
- [8] E143 Collaboration. *Phys. Lett.*, **74**, 346 (1995).
- [9] E143 Collaboration. *Phys. Lett.*, **B364**, 61 (1995).
- [10] E154 Collaboration. *Phys. Rev. Lett.*, **79**, 26 (1997).
- [11] E154 Collaboration. *Phys. Lett.*, **B405**, 180 (1997).
- [12] E155 Collaboration. *Phys. Lett.*, **B458**, 529 (1998).
- [13] E155 Collaboration. *Phys. Lett.*, **B458**, 536 (1998).
- [14] E155 Collaboration. *Phys. Lett.*, **B463**, 339 (1999).

- [15] M. Anselmino, A. Efremov, E. Leader. *Phys. Rep.*, **261**, 1 (1995).
- [16] E143 Collaboration. *Phys. Lett.*, **B452**, 194 (1999).
- [17] R. P. Feynman. *Phys. Rev. Lett.*, **23**, 1415 (1969).
- [18] D. J. Gross and F. Wilczek. *Phys. Rev.*, **D9**, 980 (1974).
- [19] R. G. Roberts. *The Structure of the Proton*, p. 34 (Cambridge, 1990).
- [20] C. G. Callan and D. J. Gross. *Phys. Rev. Lett.*, **22**, 156 (1969).
- [21] G. Altarelli. *Phys. Rep.*, **81**, 1 (1982).
- [22] D. E. Groom et al. *Eur. Phys. Journ.*, **C15**, 1 (2000).
- [23] R. D. Erbacher. *E155 Tech Note 69* (September 1998). Unpublished.
- [24] K. Gottfried. *Phys. Rev. Lett.*, **18**, 1154 (1967).
- [25] J. D. Bjorken. *Phys. Rev.*, **148**, 1467 (1966).
- [26] S. A. Larin and J. A. M. Vermaseren. *Phys. Lett.*, **B259**, 245 (1991).
- [27] J. Ellis and R. L. Jaffe. *Phys. Rev.*, **D9**, 1444 (1974).
- [28] J. Ellis and R. L. Jaffe. *Phys. Rev.*, **D10**, 1669 (1974). Addendum to [27].
- [29] K. G. Wilson. *Phys. Rev.*, **179**, 1499 (1969).
- [30] S. A. Larin. *Phys. Lett.*, **B334**, 192 (1994).
- [31] J. E. Clendenin et al. *SLAC-PUB-7619* (August 1997). Unpublished.
- [32] Z. D. Farkas et al. *SLAC-PUB-1453* (June 1974). Unpublished.
- [33] C. Prescott. *E155 Tech Note 24* (November 1996). Unpublished.

- [34] A. A. Kresnin and L. N. Rosentsveig. *Journ. Exp. Theor. Phys. (USSR)*, **32**, 9353 (1957).
- [35] B. Wagner et al. *Nucl. Instr. and Meth.*, **A294**, 541 (1990).
- [36] L. G. Levchuk. *Nucl. Instr. and Meth.*, **A345**, 496 (1994).
- [37] M. Swartz et al. *Nucl. Instr. and Meth.*, **A363**, 526 (1995).
- [38] H. R. Band et al. *E154 Tech Note 40* (October 1996). Unpublished.
- [39] H. R. Band et al. *Nucl. Instr. and Meth.*, **A400**, 24 (1997).
- [40] P. Bosted. *E155 Tech Note 9* (June 1996). Unpublished.
- [41] Y. Kolomensky. *Precision Measurement of the Neutron Spin Dependent Structure Functions*. Ph.D. thesis, University of Massachusetts, Amherst (1997).
- [42] E155 Collaboration. *E155 Tech Note 8* (February 1996). Unpublished.
- [43] P. Bosted. *E155 Tech Note 10* (October 1996). Unpublished.
- [44] J. Groves and J. Olmsted. *E155 Tech Note 23* (September 1996). Unpublished.
- [45] T. Toole. *E155 Tech Note 86* (July 1999). Unpublished.
- [46] C. Prescott. *E155 Tech Note 25* (December 1996). Unpublished.
- [47] T. Toole. *E155 Tech Note 99* (August 1999). Unpublished.
- [48] P. L. Anthony and Z. M. Szalata. *SLAC-PUB-7201* (June 1996). Unpublished.
- [49] A. Abragam. *Principles of Nuclear Magnetism* (Oxford University Press, 1961).
- [50] A. Abragam and M. Goldman. *Rep. Prog. Phys.*, **41**, 395 (1978).

- [51] C. D. Jeffries. *Ann. Rev. Nuc. Sci.*, **14**, 101 (1964).
- [52] M. Goldman. *J. Magn. Res.*, **17**, 393 (1975).
- [53] S. I. Penttilä et al. In *Proceedings of the Workshop on NMR in Polarized Targets*, S. Büeltmann and D. G. Crabb, editors, p. 15 (1998). Unpublished.
- [54] G. R. Court et al. *Nucl. Instr. and Meth.*, **A324**, 433 (1993).
- [55] W. Meyer. *Nucl. Instr. and Meth.*, **215**, 65 (1983).
- [56] D. G. Crabb et al. *Phys. Rev. Lett.*, **64**, 2627 (1990).
- [57] O. A. Rondon. *Phys. Rev.*, **C60**, 1 (1999).
- [58] D. G. Crabb and D. B. Day. *Nucl. Instr. and Meth.*, **A356**, 9 (1995).
- [59] T. D. Averett et al. *Nucl. Instr. and Meth.*, **A427**, 440 (1999).
- [60] Büeltmann et al. *Nucl. Instr. and Meth.*, **A425**, 22 (1999).
- [61] P. Bosted. *E155 Tech Note 11* (July 1996). Unpublished.
- [62] T. O. Ninikoski, A. Rijllart. *Nucl. Instr. and Meth.*, **199**, 485 (1982).
- [63] F. Pobell. *Matter and methods at low temperatures* (Springer-Verlag, 1992).
- [64] Y. F. Kisselev. *Nucl. Instr. and Meth.*, **A356**, 99 (1995).
- [65] E143 Collaboration. *Phys. Lett.*, **B452**, 194 (1998).
- [66] G. R. Court and M. A. Houlden. In *Proceedings of the Workshop on NMR in Polarized Targets*, S. Büeltmann and D. G. Crabb, editors, p. 35 (1998). Unpublished.

- [67] G. R. Court and M. A. Houlden. *LIVHEP 97/01* (1997). Unpublished.
- [68] *Workshop on NMR in Polarized Targets*, S. Büeltmann and D. G. Crabb, editors (University of Virginia, 1998).
- [69] S. Büeltmann et al., *NMR Meeting*, University of Virginia.
- [70] G. Court et al., *NMR Meeting*, University of Virginia.
- [71] W. H. Press and S. A. Teukolsky. *Comp. in Phys.*, **6**, 274 (1992).
- [72] P. L. Jolivet. *Comp. in Phys.*, **7**, 208 (1993).
- [73] G. Mitchell. *A Precision Measurement of the Spin Structure Function $g_1(x, Q^2)$ for the Proton and Deuteron*. Ph.D. thesis, University of Wisconsin, Madison (1999). Appendix A.
- [74] S. Rock. *E155 Tech Note 38* (July 1997). Unpublished.
- [75] N. Benmouna. *E155 Tech Note 92* (July 1999). Unpublished.
- [76] C. Y. Prescott et al. *Phys Lett*, **B84**, 524 (1979).
- [77] P. Bosted. *E154 Tech Note 29* (January 1995). Unpublished.
- [78] Y. Kolomensky. *Precision Measurement of the Neutron Spin Dependent Structure Functions*. Ph.D. thesis, University of Massachusetts, Amherst (1997). p. 152-155.
- [79] P. Bosted. *E155 Tech Note 63* (June 1998). Unpublished.
- [80] G. Mitchell. *A Precision Measurement of the Spin Structure Function $g_1(x, Q^2)$ for the Proton and Deuteron*. Ph.D. thesis, University of Wisconsin, Madison (1999).

- [81] K. Griffioen. *E155 Tech Note 90* (July 1999). Unpublished.
- [82] O. Rondon. *E155 Tech Note 14* (August 1996). Unpublished.
- [83] T. Averett. *E155 Tech Note 27* (March 1997). Unpublished.
- [84] P. Bosted. *E155 Tech Note 62* (June 1998). Unpublished.
- [85] W. Tobias. *E155 Tech Note 36* (July 1997). Unpublished.
- [86] W. Tobias. *Measurement of the Spin Structure Functions g_1 and g_2 of the Deuteron*. Ph.D. thesis, University of Virginia (2000). To be approved.
- [87] E142 Collaboration. *Phys. Rev.*, **D49**, 4348 (1994).
- [88] D. Reyna. *E154 Tech Note 52* (January 1997). Unpublished.
- [89] T. V. Kukhto and N. M. Shumeiko. *Nucl. Phys.*, **B219**, 412 (1983).
- [90] S. Kuhn and F. Wesselmann. *E155 Tech Note 59* (July 1998). Unpublished.
- [91] F. Wesselmann. *E155 Tech Note 100* (September 1999). Unpublished.
- [92] NMC Collaboration. *Phys. Lett.*, **B364**, 107 (1995).
- [93] P. Grenier et al. *E143 Tech Note 62* (June 1994). Unpublished.
- [94] J. Bauer. *Measurement of the Longitudinal Deuteron Spin-Structure Function in Deep-Inelastic Scattering*. Ph.D. thesis, University of Massachusetts, Amherst (1996).
- [95] G. Mitchell. *E155 Tech Note 101* (September 1999). Unpublished.
- [96] M. S. M. Glück, E. Reya. *Phys. Rev.*, **D53**, 4775 (1996).

- [97] M. Glück, E. Reya, A. Vogt. *Eur. Phys. J.*, **C5**, 461 (1998).
- [98] SMC Collaboration. *Phys. Rev.*, **D56**, 5330 (1997).
- [99] B. Lampe and E. Reya. *LANL Preprint: hep-ph/9810270* (1998).
- [100] J. W. Harris et al. *Nucl. Phys.*, **A566**, 277c (1994).
- [101] N. Saito. *Nucl. Phys.*, **A638**, 575c (1997).
- [102] F. Bradamante. *Nucl. Inst. and Meth.*, **A622**, 50 (1997).
- [103] R. G. Arnold et al. *SLAC-PROPOSAL-E-156* (1997). Unpublished.
- [104] Y. K. Semertzidis. *Nucl. Instr. and Meth.*, **A356**, 83 (1995).
- [105] C. P. Slichter. *Principles of Magnetic Resonance* (Springer-Verlag, 1990).